Alma Mater Studiorum · Università di Bologna

Scuola di Scienze
Dipartimento di Fisica e Astronomia
Corso di Laurea Magistrale in Fisica

Future constraints on neutrino properties with Euclid

Relatore:
Dott.ssa Nicoletta Mauri

Correlatore:
Dott.ssa Maria Archidiacono

Presentata da:
Monica Rossi

Anno Accademico 2018/2019

Contents

Abstract

At present, the stronger bounds on neutrino mass come from the KATRIN experiment, which set an upper limit on the electron neutrino mass at $m_{\nu_e} < 1.1\,\mathrm{eV}$, and from Planck cosmological observations, setting an upper limit on the sum of neutrino masses at $\sum m_\nu < 0.12\,\mathrm{eV}$. Cosmology offers in fact the possibility of putting model-dependent constraints on neutrino properties. In this thesis a forecast on the sensitivity of the future ESA Euclid mission has been evaluated. Euclid aims to investigate the nature of dark energy and dark matter and verify General Relativity on large scales, and will provide also strong bounds on neutrino mass and number.

In this thesis, two different scenarios are considered: the first is a ΛCDM model with three massive active neutrinos, the second adds also one sterile neutrino. In the first case, a sensitivity of $0.02\,\mathrm{eV}$ on $\sum m_\nu$ and a sensitivity of 0.066 on the number of active neutrinos are evaluated. In the second case, a sensitivity on the sterile neutrino effective mass of $0.035\,\mathrm{eV}$ and a sensitivity of 0.066 on the number of extra neutrinos are obtained. These results will represent a big improvement with respect to current cosmological bounds.

Sommario

Attualmente i limiti più stringenti sulla massa dei neutrini sono stati ottenuti dall'esperimento KATRIN, che ha posto un limite superiore per la massa del neutrino elettronico di $m_{\nu_e} < 1.1\,\mathrm{eV}$, e dalle osservazioni cosmologiche di Planck, che hanno stabilito un limite superiore per la somma delle masse dei neutrini $\sum m_\nu < 0.12\,\mathrm{eV}$. La cosmologia offre infatti la possibilità di porre vincoli *model-dependent* sulle proprietà dei neutrini. In questa tesi è stata effettuata una previsione sulla precisione della futura missione ESA Euclid. Euclid mira ad investigare la natura dell'energia oscura e della materia oscura e a verificare la Relatività Generale su grandi scale. Fornirà inoltre misure stringenti sul numero e la massa dei neutrini.

In questa tesi sono stati considerati due scenari: il primo è un modello ΛCDM con tre neutrini massivi attivi, il secondo aggiunge anche un neutrino sterile. Nel primo caso sono state calcolate una sensibilità di $0.02\,\mathrm{eV}$ per $\sum m_\nu$ e una sensibilità di 0.066 sul numero di neutrini attivi. Nel secondo caso sono state ottenute una sensibilità sulla massa effettiva del neutrino sterile di $0.035\,\mathrm{eV}$ e una sensibilità di 0.066 sul numero di neutrini extra. Questi risultati rappresenteranno un notevole miglioramento rispetto agli attuali vincoli posti dalla cosmologia.

Introduction

The determination of neutrino properties have been, since their discovery, one of the most challenging issues in particle physics, due to their elusive nature. Neutrinos are color-less and charge-less particles and they only interact with charged fermions and massive gauge bosons through weak interactions. The continuous dialogue between theories and experiments in the second half of the last century have brought to the birth of the Standard Model (SM) of particle physics, that summarises the properties of known fundamental particles and of the basic forces that rule their interactions. In this model neutrinos are considered massless and left-handed particles. The discovery of neutrino flavour oscillations of atmospheric and solar neutrinos, however, has open the door to a new physics beyond the SM and many experiments have studied neutrinos from different sources, increasing the knowledge about parameters involved in the neutrino oscillation. The most important consequence of neutrino oscillations is that neutrinos have non-zero rest masses and that the observed flavour eigenstates $(\nu_e, \nu_\mu, \nu_\tau)$ are a mixing of the mass eigenstates (ν_1, ν_2, ν_3).

In the last decades many experiments have put strong constraints on the neutrinos properties. The more stringent constraints on neutrino mass come from the KATRIN experiment, that has derived an upper limit on the absolute electron neutrino mass at $m_{\nu_e} < 1.1\,\mathrm{eV}$, and from Planck, that has set the upper limit for the sum of neutrino masses in the contest of a standard ΛCDM model at $\sum m_\nu < 0.12\,\mathrm{eV}$. Many questions, however, are still open as the neutrino mass ordering and the absolute neutrino mass. Moreover, hints for new physics come from anomalies in oscillation neutrino experiments, that suggest the existence of extra neutrino states not participating in electroweak interactions, called sterile neutrinos.

Neutrino properties play a big role also in the context of cosmology, because of their impact on the formation of large-scale structures in the Universe. Being very light and weakly interacting particles, neutrinos are in fact able to travel freely in the primordial Universe, smoothing the density anisotropies and slowing the galaxy clustering and the formation of structures.

Euclid, an ESA space mission, is aimed at performing a survey of a large fraction of the extragalactic sky over a 6 years period, observing galaxies in the visible and near-infrared wavelengths up to redshift $z = 2$. Its design was optimized in order to investigate the nature of dark energy and dark matter and verify General Relativity on large scales. It will allow to obtain a big improvement on the sensitivity for cosmological parameters, in particular on the sum of neutrino masses.

In this thesis, forecasts on the sensitivity of the Euclid experiment for the neutrino mass have been evaluated in the context of different cosmological models, using two software codes: CLASS and MontePython. The CLASS code is a Boltzmann solver that, given a set of cosmological parameters, evolves the background and perturbations of the primordial Universe, returning the observed spectra. MontePython is a Monte Carlo sampler that is able to interact with CLASS and has been used to evaluate the posterior functions for the cosmological parameters of interest, in particular the ones constraining neutrino properties.

This thesis is structured as follows:

- In Chapter 1 neutrino properties and the basics of cosmology are described, focusing the attention on the effect of neutrinos on the evolution of the Universe.
- In Chapter 2 the Euclid experiment is described, together with the scientific requirements needed for weak lensing and galaxy clustering probes.
- In Chapter 3 the principles of Bayesian inference are discussed, together with the structure of the two codes used for the forecast.
- Chapter 4 reports the procedure used for the analysis and the results obtained for the Euclid forecasts on neutrino properties.

Chapter 1

Neutrinos and cosmology

Neutrinos are one of the most studied components of the Universe, since they were postulated by W. Pauli in 1930 to understand weak interactions. The modern knowledge about their properties has been reached in the last decades thanks to a vast suite of experiments and theoretical works, which has made possible for neutrino physics to quickly advance.

Neutrinos are fundamental particles with spin 1/2, color-less and charge-less. They therefore only interact with charged fermions and massive gauge bosons through weak interactions. In the Standard Model (SM) of particle physics, neutrinos ν and antineutrinos $\bar{\nu}$ are distinct and massless particles, and their helicity is always left-handed for the neutrinos and right-handed for the antineutrinos: these properties are well explained by the two-component model of neutrinos, first proposed by Landau [1], Lee and Yang [2] and Salam [3] in 1957. Being the upper limit for the neutrino mass considered very low at that time ($m_\nu \lesssim (100-200)\,\mathrm{eV}$), neutrinos were assumed to be massless and described by two chiral fields $\nu_L(x)$ and $\nu_R(x)$. The massless nature of neutrinos implies a permanent helicity state, measured later by the Goldhaber et al. experiment and discovered being left-handed for neutrinos and right-handed for antineutrinos.

In 1957, however, B. Pontecorvo theorized that if neutrinos were massive there could exist processes where the neutrino flavour is not conserved, called neutrino oscillations, which take place on macroscopic distances for small neutrino masses and require the introduction of a right-handed neutrino. In the last decades, the discovery of this oscillation phenomenon from a variety of experiments on solar, atmospheric, reactor and accelerator neutrinos requests that the mass of both neutrinos and antineutrinos is different from zero and that the Standard Model must be extended.

Lepton	$Q\,[e]$	L_e	L_μ	L_τ	L
e^-	-1	1	0	0	1
ν_e	0	1	0	0	1
μ^-	-1	0	1	0	1
ν_μ	0	0	1	0	1
τ^-	-1	0	0	1	1
ν_τ	0	0	0	1	1

Table 1.1: Quantum numbers of the three lepton generations: $Q\,[e]$ electric charge, L_e electron number, L_μ muon number, L_τ tau number and $L = L_e + L_\mu + L_\tau$ total lepton number.

1.1 Neutrino masses, mixing and oscillations

Neutrinos belong to the lepton family and, with the associated charged leptons, are grouped in three weak isospin doublets with defined quantum numbers, as showed in Table 1.1. Measurements of the invisible Z decay width at LEP had shown that the number of light neutrinos sensitive to weak interactions is $N_\nu = 2.994 \pm 0.012$ [4], with the three flavour neutrinos being ν_e, ν_μ and ν_τ and the corresponding antineutrinos $\bar{\nu}_e$, $\bar{\nu}_\mu$ and $\bar{\nu}_\tau$.

In 1998 were observed for the first time neutrino oscillations, which consist of transitions in flight between the different flavour neutrinos or antineutrinos and will be discussed more in detail in Sec. 1.1.1. Flavour oscillations are a consequence of neutrino mixing, since the flavour eigenstates of Standard Model $\nu_f = (\nu_e, \nu_\mu, \nu_\tau)$ do not correspond to the Hamiltonian eigenstates (ν_1, ν_2, ν_3) with defined mass (m_1, m_2, m_3). In this case, a left-handed flavour neutrino $|\nu_f\rangle$ is seen as a combination of mass eigenstates $|\nu_i\rangle$ (with $m_i \neq 0$)

$$|\nu_f\rangle = \sum_i U_{fi}\,|\nu_i\rangle\,, \qquad \text{with} \quad f = e, \mu, \tau; \quad i = 1, 2, 3. \tag{1.1}$$

The unitary matrix U is called the Pontecorvo-Maki-Nakagawa-Sakata (PMNS) mixing matrix [5, 6]. The minimal parametrization consist of a 3×3 matrix with three rotation angles θ_{23}, θ_{13}, θ_{12} $(0 \leq \theta_i \leq \pi/2)$ and 1 or 3 CP violation phases depending on whether the neutrinos are Dirac or Majorana particles. A massive Majorana particle is identical to its own antiparticle, on the basis of existing neutrino data it is impossible to determine whether massive neutrinos are Dirac or Majorana fermions. The PMNS matrix can be represented by the matrix product

$$
\begin{aligned}
U &= \begin{bmatrix} 1 & 0 & 0 \\ 0 & c_{23} & s_{23} \\ 0 & -s_{23} & c_{23} \end{bmatrix} \begin{bmatrix} c_{13} & 0 & s_{13}e^{-i\delta} \\ 0 & 1 & 0 \\ -s_{13}e^{i\delta} & 0 & c_{13} \end{bmatrix} \begin{bmatrix} c_{12} & s_{12} & 0 \\ -s_{12} & c_{12} & 0 \\ 0 & 0 & 1 \end{bmatrix} \times \operatorname{diag}\left(1, e^{i\alpha_{21}/2}, e^{i\alpha_{31}/2}\right) \\
&= \begin{bmatrix} c_{12}c_{13} & s_{12}c_{13} & s_{13}e^{-i\delta} \\ -s_{12}s_{23} - c_{12}s_{23}s_{13}e^{i\delta} & c_{12}c_{23} - s_{12}s_{23}s_{13}e^{i\delta} & s_{23}c_{13} \\ s_{12}s_{23} - c_{12}c_{23}s_{13}e^{i\delta} & -c_{12}s_{23} - s_{12}c_{23}s_{13}e^{i\delta} & c_{23}c_{13} \end{bmatrix} \times \operatorname{diag}\left(1, e^{i\alpha_{21}/2}, e^{i\alpha_{31}/2}\right)
\end{aligned}
\tag{1.2}
$$

where $c_{ij} = \cos\theta_{ij}$ and $s_{ij} = \sin\theta_{ij}$ for $ij = 23$, 13 or 12 ($\theta_{ij} = [0, \pi/2)$), and $\delta = [0, 2\pi]$ is the Dirac CP-violating phase. The phases α_{21} and α_{31} are two Majorana CP violation phases and play no role in neutrino oscillations [7]. For this reason, both Majorana phases can be considered null in the standard form of the neutrino mixing matrix discussed in this thesis.

1.1.1 Neutrino oscillations

If the mass eigenstates are not degenerate, the phase of each one will evolve as

$$|\nu_i(L,T)\rangle = e^{-iE_iT + ip_iL} |\nu_i\rangle , \tag{1.3}$$

with E and p being the energy and momentum operators and L the distance after the time T. The different evolution of the mass eigenstates which form the flavour eigenstate will therefore cause the flavour oscillation. In case of ultrarelativistic neutrinos, the propagation time is equal to the travelled distance up to some corrections depending on the mass and the energy of the neutrinos, leading to the approximation

$$E_iT - p_iL \simeq (E_i - p_i) L = \frac{E_i^2 - p_i^2}{E_i + p_i} L = \frac{m_i^2}{E_i + p_i} L \simeq \frac{m_i^2}{2E} L. \tag{1.4}$$

From the amplitude of the $\nu_\alpha \to \nu_\beta$ transition it is then possible to obtain the probability that a neutrino generated with an α flavour is found to have a different flavour β after the time T

$$
\begin{aligned}
P_{\nu_\alpha \to \nu_\beta}(L,T) = |\langle \nu_\beta | \nu_\alpha(L,T)\rangle|^2 &= \left| \sum_i U_{\alpha i}^* e^{-iE_iT + ip_iL} U_{\beta i} \right|^2 \simeq \left| \sum_i U_{\alpha i}^* e^{-\frac{i m_i L}{2E}} U_{\beta i} \right|^2 \\
&= \sum_i |U_{\alpha i}|^2 |U_{\beta i}|^2 + 2\Re \sum_{i>k} U_{\alpha i}^* U_{\beta i} U_{\alpha k} U_{\beta k}^* \exp\left(-i \frac{\Delta m_{ik}^2 L}{2E}\right),
\end{aligned}
\tag{1.5}
$$

where m_i are the mass eigenstates and the squared mass differences $\Delta m_{ik}^2 = m_i^2 - m_k^2$ (with $i \neq k$) can be investigated using different values of L/E. Experiments consisting of a neutrino beam travelling through detectors placed near and far from the source has been designed to reveal this oscillations and can be divided in short-baseline (SBL) and long-baseline (LBL) depending on the distance L of the detector from the source, which determines the sensitivity to Δm^2.

Two flavour case

An useful approximation of the three-neutrino mixing is the case in which only two different flavours are considered. Given two flavour states (ν_α, ν_β), linear superposition of two massive neutrinos (ν_1, ν_2), the PMNS matrix becomes

$$U = \begin{bmatrix} \cos\theta & \sin\theta \\ -\sin\theta & \cos\theta \end{bmatrix}. \tag{1.6}$$

The oscillation probability for the two-flavour case can be obtained from Eq. 1.5 and is

$$P_{\nu_\alpha \to \nu_\beta} = \sin^2 2\theta \sin^2 \frac{\Delta m^2 L}{4E} \qquad \alpha \neq \beta, \tag{1.7}$$

so that the maximum probability to find the neutrino in the $|\nu_\beta\rangle$ state is at a distance $L_{osc}/2 = 2\pi E/\Delta m^2$, while after a full oscillation length the system turns back to the initial state $|\nu_\alpha\rangle$.

The dependence of the oscillation probability on the squared mass difference makes possible to simplify the description of the oscillation phenomenon. Considering a convenient range of the ratio L/E, for example the atmospheric neutrino range $L/E \sim 10^3\,\mathrm{km/GeV}$, the two neutrinos with the lower Δm^2 are in fact considered as degenerate, so that only the mass difference with the third neutrino is responsible for the oscillation: this allows the two-flavour approximation. Considering for example the case $m_1 < m_2 < m_3$, i.e. the Normal Ordering described in the next Section, the mass eigenstate 1 and 2 are considered degenerate, so that the effective mixing is between ν_2 and ν_3, giving the flavour eigenstates ν_μ and ν_τ. Varying the distance L and the energy E of neutrinos, oscillations can be dominated by the squared mass difference between eigenstates 1 and 2 and with analogous consideration it is possible to obtain the other mixing angles [8]. The complete PMNS matrix parametrization showed in Eq. 1.2 has thus been divided into three sections which show the mixing of the couples of mass eigenstates (respectively (m_2, m_3), (m_1, m_3) and (m_1, m_2)), referring to experiments sensitive to the various parameters:

- the first part relates to atmospheric neutrino experiments, sensitive to $\sin^2\theta_{23}$ and Δm^2_{13};
- the second part relates to reactor neutrino experiments, sensitive to θ_{13};
- the third part relates to solar neutrino experiments, sensitive to $\sin^2\theta_{12}$ and Δm^2_{21};
- other long-baseline accelerator experiments are moreover sensitive to $\sin^2\theta_{23}$, Δm^2_{31} and θ_{13}.

1.1.2 Squared mass differences and limits on neutrino masses

Experimental data about the squared mass differences has been showing a positive value for Δm^2_{21} and a hierarchy between the mass splittings $\Delta m^2_{21} \ll |\Delta m^2_{31}| \simeq |\Delta m^2_{32}|$, with $\Delta m^2_{ij} \equiv m^2_i - m^2_j$. In the standard framework of three-neutrino mixing, there are therefore two possible orderings for the neutrino masses, named *Normal Ordering* (NO) with $m_1 < m_2 < m_3$, and *Inverted Ordering* (IO) with $m_3 < m_1 < m_2$.
The squared mass difference Δm^2_{21} has been experimentally measured thanks to the effects of the neutrino propagation in matter and is strictly greater than zero, so that $m_2 > m_1$, while the other measurable mass difference is denoted by Δm^2_{3l}, where

$$\Delta m^2_{3l} = \begin{cases} \Delta m^2_{31} > 0 & \text{for NO,} \\ \Delta m^2_{32} < 0 & \text{for IO.} \end{cases} \tag{1.8}$$

The current best fits of the two squared mass differences are [9]:

$$\Delta m^2_{21} = 7.53 \pm 0.18 \cdot 10^{-5}\,\mathrm{eV}^2 \tag{1.9}$$

$$\Delta m^2_{3l} = -2.55 \pm 0.04 \cdot 10^{-3}\,\mathrm{eV}^2\,(\mathrm{IO}) \tag{1.10}$$

$$= 2.444 \pm 0.034 \cdot 10^{-3}\,\mathrm{eV}^2\,(\mathrm{NO}) \tag{1.11}$$

Neutrino oscillation experiments are in fact insensitive to the absolute scale of neutrino masses and the knowledge of the sign of Δm^2_{21} leaves one neutrino mass unconstrained. This leads, if the mass of the lightest neutrino is small, to the two possible neutrino orderings characterized by the sign of Δm^2_{31}: the normal ordering, which prescribes the presence of two light and one heavy neutrinos, and the inverted one, with one light and two heavy neutrinos, as shown in Figure 1.1. If neutrino masses are much larger than the squared mass differences Δm^2, all neutrinos share in practice the same mass and can be considered degenerate. Nowadays neutrino oscillation measurements reported in Eq. 1.9-1.11 provide a lower limit for the sum of neutrino masses of 0.06 eV, when the lightest neutrino mass can be considered null or negligible with respect to the others [9].

Since oscillation experiments can measure only the squared mass differences between two mass eigenvalues, they are not sensitive to the absolute mass scale. Direct measurements of the neutrino masses are possible, in principle, using kinematic methods in the single beta decay, but only upper limits have been reached and the most stringent is set by the KATRIN experiment [10]: $m_{\nu_e} < 1.1\,\mathrm{eV}$ at 90% C.L.
From cosmology it is also possible to obtain an upper limit on the neutrino masses, but the disadvantage of these type of measurements is the fact that they are model dependent. The strongest constraint in this case comes from the Planck experiment [11], with a 95% upper limit on the sum of neutrino masses of $\sum m_\nu < 0.12\,\mathrm{eV}$ assuming the ΛCDM model.

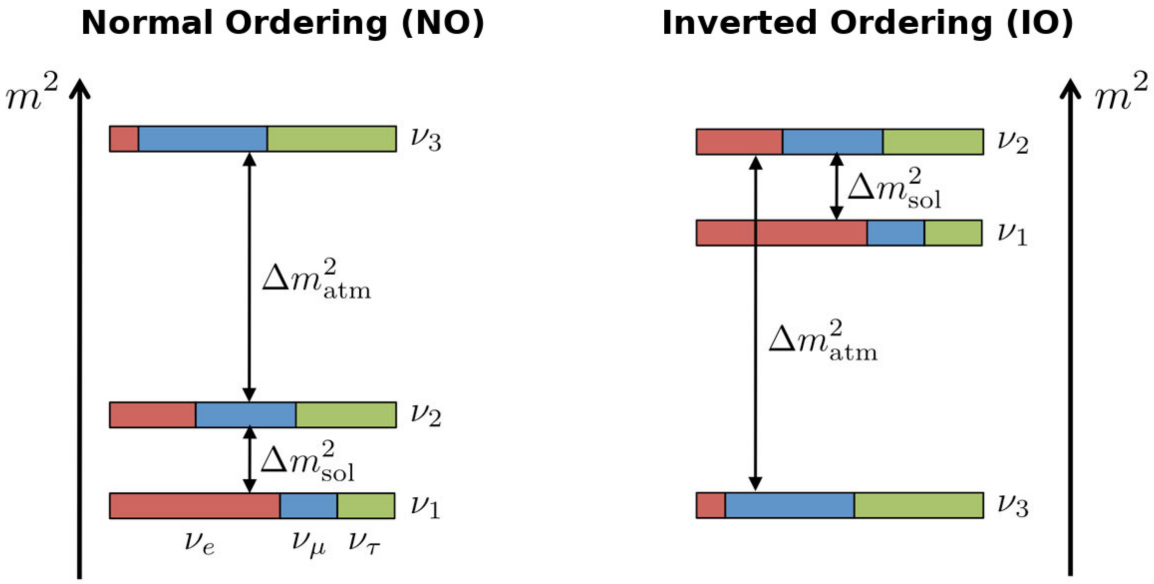

Figure 1.1: Normal and inverted ordering of neutrino masses.

1.1.3 Sterile neutrinos

A possible scenario of new physics beyond the Standard Model is the possibility that the number of massive neutrinos is larger than the number of flavour neutrinos. In this case, the extra neutrino states do not participate in electroweak interactions and are named as *sterile neutrinos*, while the others are referred to as *active*.

Possible hints of the existence of this type of neutrinos come from anomalies in short-baseline experiments as LSND (Liquid Scintillator Neutrino Detector) [12] and MiniBooNE [13–15], that could be described introducing this new particle, or from the re-evaluation of data from reactor experiments and from radio-chemical solar neutrino experiments based on gallium.

- The LSND experiment (a short baseline accelerator experiment at the Los Alamos National Laboratories) [12] observed a significant excess of events over the background of $\bar{\nu}_e$ from a $\bar{\nu}_\mu$ beam (appearance), so that the most straightforward interpretation is an antineutrino oscillation with a squared mass difference $\Delta m^2 \simeq 1\,\text{eV}$. Since in the previous section it has been shown that squared mass differences from solar and atmospheric neutrinos oscillation experiments are much smaller, the LSND experiment requires the introduction of another neutrino. This neutrino, however, can not weakly interact because of the constraint on the number of active neutrinos from LEP already seen in Sec. 1.1.

- The MiniBooNE experiment at Fermilab showed an excess of electron-like events in ν_μ and $\bar{\nu}_\mu$ beams, compatible with short baseline $\bar{\nu}_\mu \to \bar{\nu}_e$ and $\nu_\mu \to \nu_e$ oscillations. These oscillations require a mass splitting compatible with the LSND result, at the scale of $\Delta m^2 \simeq 1\,\mathrm{eV}$ [13–17].
- The re-analyses of data from short baseline (SBL) reactor neutrino oscillation experiments [18,19], using newly calculated fluxes of $\bar{\nu}_e$ from reactors, show a possible disappearance of about the 6% of antineutrinos. This is compatible with a sterile neutrino with $\Delta m_s^2 > 1\,\mathrm{eV}$.
- The GALLEX and SAGE solar neutrino experiments, during their calibration with radioactive electron neutrino sources, showed a lower number of events with respect to the ones expected from the knowledge of the source strength and reaction cross section. Again, it is possible to explain this disappearance introducing a sterile neutrino with $\Delta m_s^2 > 1\,\mathrm{eV}$ [19–21].

These data, however, are in strong tension with recent disappearance data from MINOS/MINOS+, NOvA and IceCube [22] and, for this reason, the SBN program at Fermilab has been designed to address the possible existence of 1 eV mass-scale sterile neutrino [10].

From the theoretical point of view, however, the existence of sterile neutrinos as neutral leptons with no ordinary weak interactions except those induced by mixing, i.e. as gauge singlets, does not imply a limit on their mass and some models predict instead the existence of a keV sterile neutrino as a warm dark matter candidate.

The existence of light sterile neutrinos has cosmological implications, because together with the neutrino mass hierarchy and their absolute values they affect the evolution of the Universe in several observable ways. Depending on their mass, neutrinos have chances to travel longer distances without falling into small potential wells, hence affecting structure formation in the early Universe, as analysed more in detail in the next sections. From cosmology it is possible for this reason to obtain better constraints on their absolute mass with respect to other Earth experiments, but in a model dependent way, assuming the standard cosmological model ΛCDM described in the next sections.

1.2 Big Bang cosmological model with dark matter

The study of the origin and evolution of the Universe has been through the centuries one of the most intriguing questions of physics. The formulation of the current Big Bang model began in the 1940s with the work of George Gamow and his collaborators, Ralph Alpher and Robert Herman, and it has modified and evolved in the last century thanks to various surveys.

One of the most important discovery was made by Hubble in 1929, seeing that other

galaxies are moving away from us and that the Universe is expanding, while another one was accidentally made in 1964 by Arno Penzias and Robert Wilson, two radio astronomers who first observed the *Cosmic Microwave Background* (CMB). The CMB is a diffuse microwave radiation which originated 380 000 years after the Big Bang and its study brought lot of information about the formation of structures as galaxies or clusters and about the cosmological parameters which constrain the Universe evolution. Being the oldest radiation emitted, its temperature has now dropped to 2.72548 ± 0.00057 K and the last and precisest measurements of its properties are nowadays provided by the Planck experiment [11, 23].
Another important ingredient in the Standard Cosmological Model is the presence of *dark matter*. It is a type of matter only weak-interacting, first theorized in 1933 by Fritz Zwicky. Observing the dynamic mass of the Coma galaxy cluster, he noticed that it was larger than the expected mass inferred from the luminosities of the galaxies composing the cluster and suggested a non-negligible mass emitting no light and forming part of the galaxy cluster. Later, his theory was supported by observations of the radial velocity distribution of spiral galaxies and of the correlation between the measured CMB anisotropy and the distribution of large structures.

The Big Bang cosmological model, nowadays based on an inflationary cosmology with the presence of both baryonic and dark matter and described in the next sections, can be decomposed in different periods beginning 13.8 billion years ago and showed in Fig. 1.2:

- *Planck era and primordial inflation* (from $10^{-43}\,$s, the *Planck time*, after the Big Bang): it is a brief era of accelerated expansion which is the origin of the tiny quantum fluctuations which will become cosmic structures. During this period the first particles (baryons, leptons and dark matter) are formed while the temperature gradually lowers and symmetries are broken.

- *Primary nucleosynthesis* ($\sim 1\,$s after the Big Bang): at a temperature $T \sim 1\,$MeV the synthesis of the light elements and neutrinos decoupling begin; it takes about three minutes for the lightest nuclei to form (deuterium, helium, lithium and beryllium). It is a radiation-dominated era and is often referred as Big Bang Nucleosynthesis (BBN) era.

- *Opaque Universe*: in this era the Universe is expanding but it is too dense to be observable. The photons mean free path is small and they are absorbed by the ionized matter very quickly. Dark matter particles evolve independently and start to clump around the cosmic seeds, slowly building a cosmic web of structures.

- *Recombination* (380 000 years after the Big Bang): when the Universe reaches a fairly low temperature, at about 3000 K, and the energy distribution of the photons sets below the ionization energy of nuclei, ordinary matter particles decouple from light and the CMB is released. The Universe becomes transparent to radiation.

- *Dark ages* (from 380 000 to 300-500 million years after the Big Bang): ordinary matter particles fall into the gravitational wells of structures created by dark matter, but stars and galaxies are yet to form. There are no astrophysical processes which can produce electromagnetic radiation.
- *Formation of structures* (about 500 million years after the Big Bang): the central regions of gravitational wells became hot enough to start burning hydrogen and the first stars were born. The emitted light split neutral atoms apart, turning them back into electrons and protons, and the Universe became half-ionized by the time it was about 700 million years old. For this reason, this is called the ‘epoch of reionisation’. At about 1 billion years after the Big Bang, collections of thousands and millions of stars grouped together to form the first galaxies and these galaxies collided and merged to form larger galaxies. These regions evolved then into the huge super-clusters of Galaxies which we see today.
- *Current era* (from 10 billion years after the Big Bang): the Universe is characterized by low density ($\approx 10^{-29}\,\mathrm{g/cm^3}$) and low temperature ($\approx 2.7\,\mathrm{K}$); photons from recombination are observable in the microwave domain.

1.3 Cosmology

A basic model of the Universe evolution was proposed by Albert Einstein. In his article about the theory of general relativity [24], published in 1915, he links the curvature of space-time, which governs the Universe evolution, to its mass-energy content. To study the global dynamics of the Universe, however, it is needed to make some assumptions about its symmetries and, in particular, to postulate the *cosmological principle.* This principle states that the Universe is homogeneous and isotropic, which means that the three-dimensional space geometry must be invariant under rotations or translations. This assumption is supported by the observation of the CMB, which shows that at its earliest stage inhomogeneities were at the 10^{-5} level. At the present age the existence of stars and galaxies means that homogeneity is valid only for scales larger than the biggest structures, but this does not affect the previously reported considerations as long as these scales are much smaller of the cosmological distances between these structures.
The evolution of an ideal smoothed Universe is therefore described and then the focus is given on how residual inhomogeneities grew to form cosmic structures.

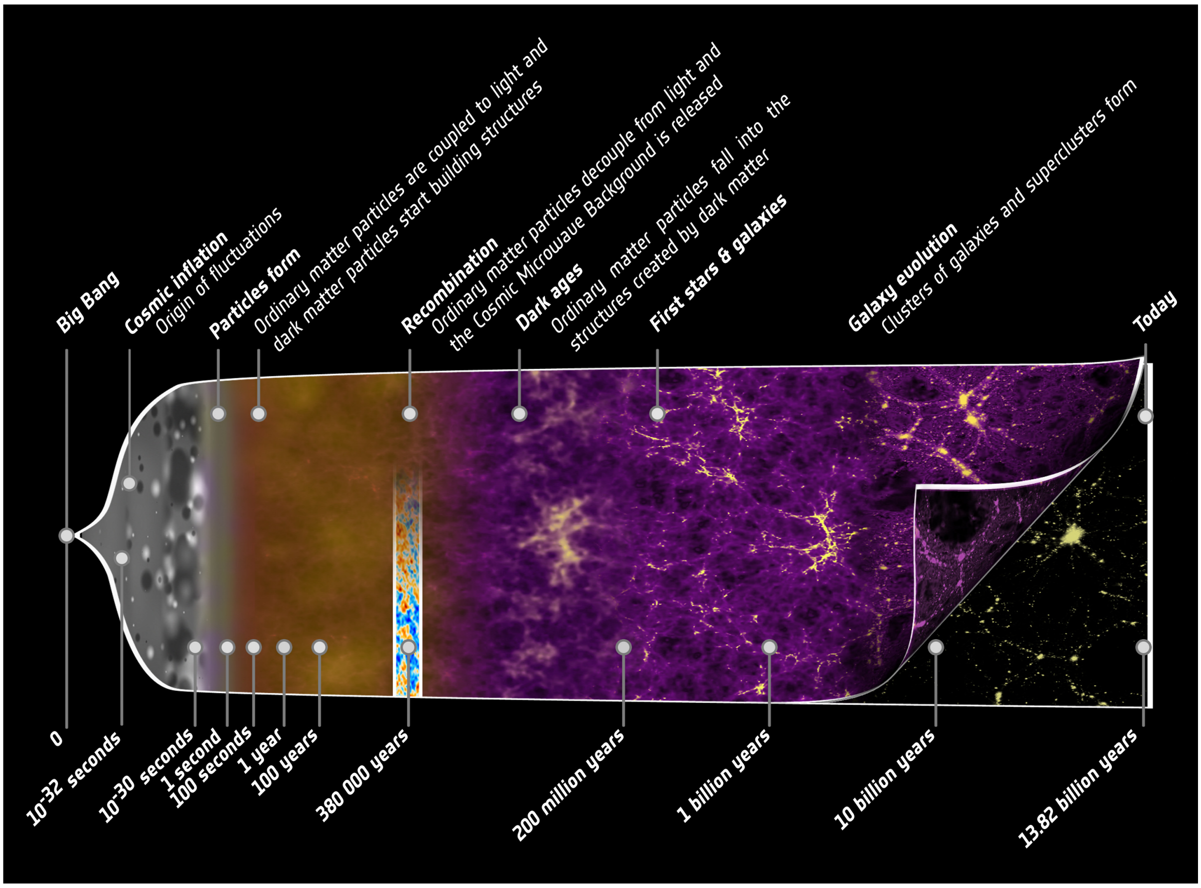

Figure 1.2: Illustration of the evolution of the Universe from the Big Bang.

1.4 Evolution of background

Under the assumption of the cosmological principle the simplest form of metric satisfying both the homogeneity and isotropy constraints is the Friedman-Robertson-Walker metric

$$g_{\mu\nu}dx^{\mu}dx^{\nu} \equiv ds^2 = c^2dt^2 - a^2\left(\frac{dr^2}{1-Kr^2} + r^2d\Omega^2\right), \tag{1.12}$$

where K parametrizes the Universe space-time curvature and only assumes the values -1, 0 or +1 respectively for hyperbolic (open), euclidean (flat) or spherical (close) geometry. The spatial part of the metric is parametrized as $d\Omega^2 = d\theta^2 \sin^2\theta d\phi^2$, with the spherical angular coordinates θ and ϕ, and t is defined as the *cosmological time*, that is the proper time of a particle travelling perpendicular to the homogeneous three-dimensional space. $a = a(t)$ is a scalar function called the *scale factor*, by which the distance scale is modulated as a function of time. Once defined the scale factor, it is possible to define also the *conformal time* as $\tau(t) = \int_0^t dt'\, a^{-1}(t')$. Below, when referring to the concept of time, it is considered the cosmological time if not explicitly stated otherwise.

The geometry of the space-time is contained in the Einstein tensor G_{ij} from the Einstein's field equation

$$G_{ij} \equiv R_{ij} - \frac{1}{2} g_{ij} R = \frac{8\pi G}{c^4} T_{ij} + \Lambda g_{ij} \tag{1.13}$$

where R_{ij} is the Ricci tensor, g_{ij} is the metric tensor previously defined, $R = g^{ij} R_{ij}$ is the Ricci scalar and $G = 6.67 \times 10^{-11}\,\mathrm{m}^3\,\mathrm{kg}^{-1}\,\mathrm{s}^{-2}$ is the gravitational constant. This equations show how space and time are determined by the energetic content of the Universe, represented on the right-hand side by the stress-energy tensor T_{ij} and by the term Λg_{ij}. This last term was introduced by Einstein trying to obtain a stationary flat solution, and will be examined in Sec. 1.4.3.

1.4.1 Friedmann equations

Solutions of the Einstein equation are two independent equations, named as *Friedmann cosmological equations*:

$$\frac{\ddot{a}}{a} = -\frac{4\pi G}{3} \left(\rho + \frac{3p}{c^2} \right) + \frac{\Lambda}{3} \tag{1.14}$$

$$\left(\frac{\dot{a}}{a} \right)^2 = \frac{8\pi G \rho}{3} - \frac{K c^2}{a^2} + \frac{\Lambda}{3} \tag{1.15}$$

with dots representing derivatives with respect of cosmological time.
p and ρ respectively represent the pressure and the density of a perfect fluid, related as

$$p = w \rho c^2, \tag{1.16}$$

where $w \sim 0$ for non-relativistic matter and $w = 1/3$ for radiation. Considering Λ null and in a spatially flat Universe, the solution of the Friedmann equations is

$$a\,(t) = a_0 \,(t/t_0)^{\frac{2}{3}(1+w)}\,, \tag{1.17}$$

which shows how the evolution of the scale factor $a\,(t)$ depends on the value of w, namely to the content of matter and radiation in the Universe. This equation is valid only for a flat geometry, for which the expansion remains positive but tends to zero when the time goes to infinity. In case of a closed universe the expansion will stop at a maximum value of a, then the universe will collapse back, while for an open universe it will continue its expansion indefinitely, with a speed $\dot{a}$ that remains positive and does not tend to zero, in opposition to the flat case. For small values of t all this models show a minimum value of a, close to zero, and indicate the start of the *Big Bang*.

1.4.2 Critical density

Friedmann equations not only show the evolution of the scale factor, but also how the geometry of the space-time depends on the energy content of the Universe. Considering Λ null and introducing the *Hubble parameter* $H \equiv \frac{\dot{a}}{a}$, Eq. 1.15 can be written as

$$H^2 = \frac{8\pi G\rho}{3} - \frac{Kc^2}{a^2} \tag{1.18}$$

and we can obtain how the energy density is related to the geometry parameter K

$$\rho = \frac{3}{8\pi G}\left(H^2 + \frac{Kc^2}{a^2}\right). \tag{1.19}$$

Using this equation it is possible to compute the *critical density* ρ_c, defined as the value of energy density for which the space is flat ($K = 0$):

$$\rho_c\left(t\right) \equiv \frac{3}{8\pi G}H^2\left(t\right). \tag{1.20}$$

If the energy density ρ is bigger than the critical density ρ_c the geometry is closed ($K > 0$) while for $\rho < \rho_c$ the geometry is hyperbolic and open ($K < 0$). It is always possible to rescale K to 1 or -1 without affecting any physical quantity.
Computing $H_0 = H\left(t = 0\right)$ at the present time is crucial to know the geometry of our Universe, though discussing the curvature K it is more convenient to use not the absolute density ρ, but the density fraction $\Omega\left(t\right)$, defined as the ratio of the density to the critical density

$$\Omega\left(t\right) \equiv \frac{\rho\left(t\right)}{\rho_c\left(t\right)}. \tag{1.21}$$

The geometry will therefore change if Ω is bigger, equal to, or smaller than one. It is important to note that in the definition of Ω does not appear the composition of the Universe, but only the sum of the different components densities. To measure the amount of each contribution the critical density ρ_c is usually used as an absolute scale, defining for example Ω_m as the matter contribution to the density parameter.
The current measured values of different components of Ω are [9]

$$\Omega_\gamma = 2.473 \times 10^{-5}\left(T/2.7255\right)^4 h^{-2} = 5.38\left(15\right) \times 10^{-5} \tag{1.22}$$

$$\Omega_m = 0.308 \pm 0.012 \tag{1.23}$$

$$\Omega_\Lambda = 0.692 \pm 0.012 \tag{1.24}$$

1.4.3 Cosmological constant Λ and dark energy

The new term Λ, called *cosmological constant*, was first introduced by Einstein in his General Relativity equations, trying to make a stationary solution possible for the evolution of Universe. This term was however abandoned after the expansion of the Universe was confirmed and only in the early 1970s it was recovered to explain the presence of an accelerated expansion ($\ddot{a} > 0$), discovered by studying the redshift in the spectrum of the Supernovae (SN) of type Ia. These SN are used as standard candles because their brightness, correlated to the mass of the star before the SN stage, is always the same and this makes them excellent distant markers once calibrated, showing that galaxies are moving away from us faster than expected from a constant expansion of the Universe (this process of reconstructing the distances of stars, called distance ladder, is examined below in Sec. 1.6.1).

It can be shown that a cosmological constant can be treated as a fluid with equation of state $p = -\rho c^2$, with $w = -1$ and an energy density

$$\rho_\Lambda \equiv \frac{c^2}{8\pi G}\Lambda; \tag{1.25}$$

the energy density is therefore constant in time as the Universe expands or contracts. This term contributes to a great part of the total energy density of the Universe but its physical interpretation is still unclear. This negative pressure fluid is usually referred as *dark energy* and there are many different proposals about its nature, from the vacuum quantum energy to a new, ultralight scalar field. Another possibility is that cosmic acceleration may arise from new gravitational physics, perhaps involving extra spatial dimensions.

The effect of the cosmological constant is to determine an acceleration in the evolution of the scale factor $a\left(t\right)$ and, studying it, it is useful to introduce the *deceleration parameter* q, defined as

$$q_0 \equiv -\left.\frac{\ddot{a}\left(t\right)a\left(t\right)}{\dot{a}^2\left(t\right)}\right|_{t=t_0}; \tag{1.26}$$

positive when the Universe expansion is slowing down. Recalling the Friedmann equations 1.14 and 1.15, for a universe containing radiation, matter and a cosmological constant it can be shown that the deceleration parameter is related to the density parameters as

$$q_0 = \Omega_{r,0} + \frac{1}{2}\Omega_{m,0} - \Omega_{\Lambda,0}. \tag{1.27}$$

The last term is therefore responsible for the acceleration in the evolution of the scale factor.

Dark energy, however, may not be a simple cosmological constant but a field that evolves dynamically with the expansion of the Universe. In this case, as its physical nature can be characterised at the most basic level by the equation of state $w\left(a\right) = \frac{p}{\rho c^2}$, any deviation from $w\left(a\right) = -1$ would imply a dynamical dark energy and its evolution with redshift can be parametrised through

$$w\left(a\right) = w_0 + w_a\left(1-a\right) = w_0 + w_a\frac{z}{1+z}. \tag{1.28}$$

1.4.4 Expansion history of the Universe

Given how each component in the Universe can influence its evolution, it is possible to study the various epochs through it has gone. The different components have in fact been dominating one over another during time, influencing the scale factor evolution. This relation can be seen writing the Friedmann equation 1.15 in a generalised way

$$H^2(t) = H_0^2 \left[\Omega_{r,0} \left(\frac{a}{a_0}\right)^{-4} + \Omega_{m,0} \left(\frac{a}{a_0}\right)^{-3} + \Omega_{\Lambda,0} - \frac{Kc^2}{H_0^2} \left(\frac{a}{a_0}\right)^{-2} \right] \tag{1.29}$$

and, considering $a_0 = 1$ and using Eq. 1.19 and 1.20, it becomes

$$\frac{H^2}{H_0^2} = \frac{\Omega_{r,0}}{a^4} + \frac{\Omega_{m,0}}{a^3} + \Omega_{\Lambda,0} + \frac{1-\Omega_0}{a^2}, \tag{1.30}$$

where the density parameters contributions are respectively from radiation, matter, cosmological constant Λ and $\Omega_0 = \Omega_{r,0} + \Omega_{m,0} + \Omega_{\Lambda,0}$. These components dominates the expansion alternatively and influence the scale factor $a(t)$ evolution. In Fig. 1.3 it is shown the scale factor a in function of time for various types of dominant components in the Universe, while in Fig. 1.4 it is shown the evolution of densities of the components of Universe. Evidences indicate we live in a Universe where radiation was dominant during

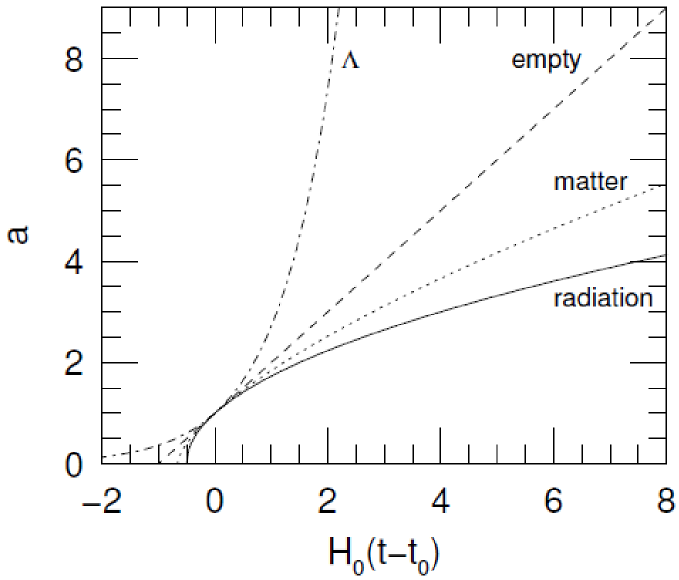

Figure 1.3: The scale factor as a function of time for an expanding, empty Universe (dashed), a flat, matter-dominated Universe (dotted), a flat, radiation dominated universe (solid), and a flat, Λ-dominated universe (dot-dash).

the early stages, followed by a period when matter was dominant. If the presently available evidence is correct we have only recently entered a period when the cosmological constant Λ is dominant.

Between the radiation-dominated and the matter-dominated periods we can define the *equivalence time*, when the densities of matter and radiation were equal. This can be written as

$$a_{eq} = \frac{\Omega_m}{\Omega_r}, \tag{1.31}$$

but it is commonly preferred to use the redshift at time of equality $z_{eq} = 3365 \pm 44$.

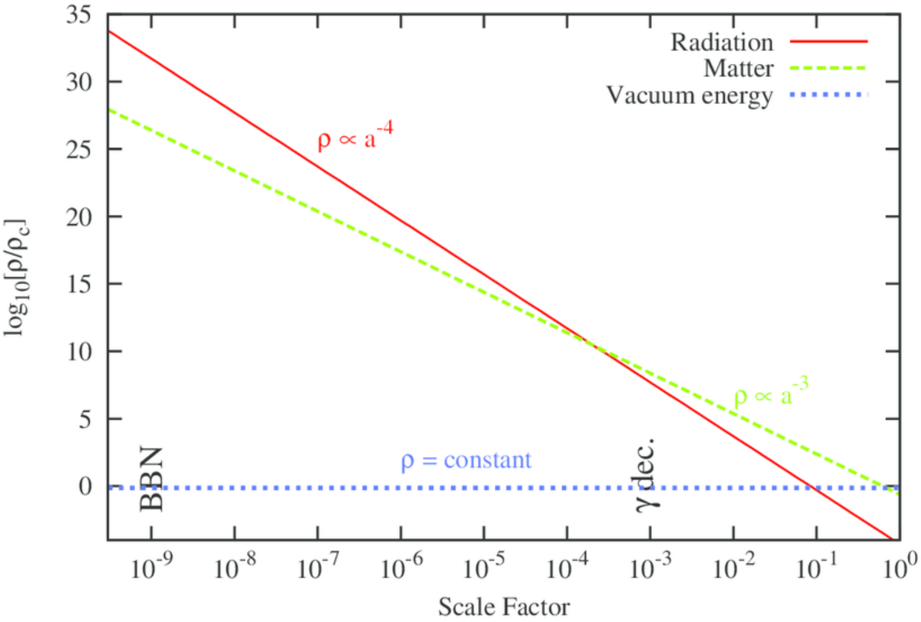

Figure 1.4: The evolution of densities of Universe components.

Redshift is often used in cosmology instead of time, because as the scale factor varies with time, the wavelength of the photons changes during their path from the place where they are emitted to the observer. If the redshift z is given by the formula

$$z = \frac{\lambda_0 - \lambda_{em}}{\lambda_{em}}, \tag{1.32}$$

using the relation

$$\frac{\lambda_{em}}{a\,(t_{em})} = \frac{\lambda_0}{a\,(t_0)} \tag{1.33}$$

we find that the redshift is related to the expansion factor at the time of emission t_{em} of the photon via the simple equation

$$1 + z = \frac{a\left(t_0\right)}{a\left(t_{em}\right)} = \frac{1}{a\left(t_{em}\right)}. \tag{1.34}$$

1.5 Formation of structures from inhomogeneities

The evolution of the small density inhomogeneities in the earlier Universe, originated by quantum fluctuations in the first moments after Big Bang, brings to the formation of large-scale structures. The mechanism for growing these structures, as galaxies, clusters and then groups of them in superclusters, is *gravitational instability*. In a homogeneous Universe, the gravitational force is the same everywhere because for each point the sum of the gravitational attraction by the surrounding matter does not change. The primordial density perturbations, on the contrary, generate a stronger gravitational attraction towards the overdense regions which are responsible for the instability. In an expanding Universe, overdense regions will thus expand less rapidly than other ones due to the gravitational attraction and, if their density is sufficiently great, they will collapse and become gravitationally bound and stable objects. These new virialized objects will, in addition, draw matter to themselves from the surrounding underdense regions, creating even bigger structures such as superclusters and voids.

To study the growth of inhomogeneities it is not used the absolute matter density $\rho\left(\vec{x}, a\right)$, but the dimensionless density fluctuation

$$\delta\left(\vec{x}, a\right) \equiv \frac{\rho\left(\vec{x}, a\right) - \bar{\rho}\left(a\right)}{\bar{\rho}\left(a\right)}, \tag{1.35}$$

where $\bar{\rho}\left(a\right)$ is the spatially averaged matter density, computed on a volume large compared to the size of the biggest structure in the Universe. The study of how large scale structure evolves with time under the influence of gravity is most tractable when $|\delta| \ll 1$, as in this limit it is possible to use linear perturbation theory. When the amplitude of the fluctuations approaches or is bigger than one, it is necessary to use different analytic approximations or numerical simulations.

In the linear approximation, the evolution of the density fluctuations field is studied making the Fourier transform of the field with respect to the comoving system and examining independently each comoving wavelength $(2\pi/k)$ of wavevector $\vec{k}$. The Fourier components $\delta_{\vec{k}} = \left|\delta_{\vec{k}}\right| e^{i\phi_{\vec{k}}}$ evolve separately when $\left|\delta_{\vec{k}}\right| \ll 1$, following the equation

$$\ddot{\delta}_{\vec{k}} + 2H\dot{\delta}_{\vec{k}} - \frac{3}{2}\Omega_m H^2 \delta_{\vec{k}} = 0, \tag{1.36}$$

as long as the proper physical wavelength $\lambda = a\left(t\right) 2\pi/k$ is small compared to the Hubble distance c/H and large compared to the *Jeans length*

$$\lambda_J = v_s \left(\frac{\pi}{G\rho} \right)^{1/2} . \tag{1.37}$$

The Jeans length λ_J is the scale which determines if a larger perturbation will collapse and grow due to gravity or if a smaller one will return to equilibrium and oscillate in density, constituting stable sound waves. In this equation $v_s = (\partial p/\partial \rho)^{1/2}$ is the *sound speed*; the speed at which the perturbation travels in a fluid with given pressure and energy density. The phase $\phi_{\vec{k}}$ remains constant as long as the amplitude $\left|\delta_{\vec{k}}\right|$ remains small. Even after fluctuations with a short proper wavelength have reached $\left|\delta_{\vec{k}}\right| \sim 1$ and collapsed, the growth of the longer wavelength perturbations is still described by Eq. 1.36. This means it is possible to use linear perturbation theory not only to study the growth of large scale structures such as galaxy clusters but even of very large structures, after the smaller ones have already collapsed.

1.5.1 Power spectra

The most important quantities for the analysis presented in this thesis are power spectra. For several measurements in cosmology, in fact, it is not important to know the exact location of maxima and minima of a field, but the statistical properties of this minima and maxima distribution. In Sections 1.3 and 1.4 it has already been examined how the Universe evolution can be approximated by the expansion of an homogeneous and isotropic universe, where inhomogeneities are studied separately and are responsible of the formation of structures. The distribution of these matter inhomogeneities can be studied for example observing the CMB anisotropies, or observing how large structures grew. This can be done through the study of the cosmic shear from weak gravitational lensing or directly computing the matter power spectrum.

CMB power spectra

In the case of the study of the CMB, the relic photons from the era of recombination, experimental data have shown that their spectrum is the same of a black-body source with a radiation temperature of $T = (2.7255 \pm 0.0006)\,\mathrm{K}$ [11]. Despite their remarkably uniform distribution over all the sky, the CMB photons show a pattern of little anisotropies in temperature and polarization of the order of about 10^{-5}, which reflect the distribution of matter anisotropies at the epoch of their last scattering, at a redshift $z \simeq 1100$ [11].

When the Universe was ionised and matter dominated, it was as a fluid of electrons and photons bounded together, where photons kept scattering smoothing out all density fluctuations. At the epoch of recombination the transition brought to a pair of coexisting gases, where the neutral hydrogen one was now free to gravitationally collapse and photons ceased to scatter beginning to propagate freely through the Universe. Photons coming from a slightly overdense region of space, however, needed to lose some energy to escape the gravitational well and free-stream, becoming colder. Photons coming from underdense regions, on the other hand, remained hotter generating temperature anisotropies: the study of CMB can therefore bring information about the first seeds of the universe we know. Although the photons at the time of their last scattering had a temperature of about 3000 K, the CMB photons have now a much lower temperature: this is caused by the expansion of the Universe, which cooled and redshifted them.

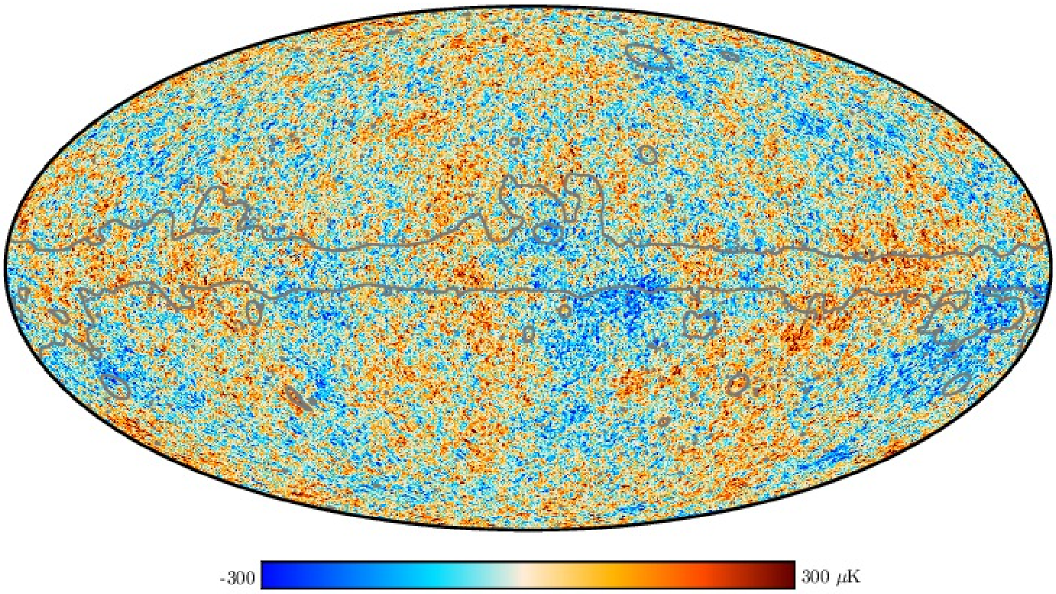

Figure 1.5: Planck temperature anisotropy map [23].

The most accurate CMB survey comes nowadays from the Planck experiment and in this case the temperature anisotropy is the component with the highest signal over noise ratio S/N. The polarization signal is instead more affected by noise and is dominated by E modes, generated by Thomson scattering in the last-scattering surface of the anisotropic temperature field. These two signals are correlated, as expected in the standard model where the degree of linear polarization is directly related to the quadrupole anisotropy in the photons when they last scatter. B-modes do not instead correlate with the temperature but are expected to be produced by primordial gravitational waves [25] [26]. CMB photons are also deflected in their path by the gravitational potentials associated with large-scale structure, allowing the measurement of the lensing potential over a wide area in the sky.

Data regarding the temperature of photons are usually summarized in maps (see Fig. 1.5) showing the temperature fluctuations $\delta T/\bar{T}\left(\theta,\phi\right)$, defined on the surface of a sphere. The most useful way to show the data is though expanding them in spherical harmonics:

$$\frac{\delta T}{\bar{T}}\left(\theta,\phi\right)=\sum_{l=0}^{\infty}\sum_{m=-l}^{l}a_{lm}Y_{lm}\left(\theta,\phi\right), \tag{1.38}$$

with $Y_{lm}\left(\theta,\phi\right)$ the usual spherical harmonic functions.
The most important statistical property of this field is the correlation function $C\left(\theta\right)$: considering two points in the directions $\hat{n}$ and $\hat{n}'$ on the last scattering surface, they are separated by the angle $\theta=\hat{n}\cdot\hat{n}'$ and the correlation function is the average product of $\delta T/\bar{T}$ couple of values over all points separated by the angle θ

$$C\left(\theta\right)=\left\langle\frac{\delta T}{\bar{T}}\left(\hat{n}\right)\frac{\delta T}{\bar{T}}\left(\hat{n}'\right)\right\rangle \tag{1.39}$$

The *CMB temperature anisotropy power spectrum* is thus defined as the angular two-point correlation function of CMB maps $\delta T/\bar{T}\left(\hat{n}\right)$. This function is usually expanded in Legendre multipoles

$$\left\langle\frac{\delta T}{\bar{T}}\left(\hat{n}\right)\frac{\delta T}{\bar{T}}\left(\hat{n}'\right)\right\rangle=\sum_{l=0}^{\infty}\frac{\left(2l+1\right)}{4\pi}C_lP_l\left(\hat{n}\cdot\hat{n}'\right), \tag{1.40}$$

where $P_l\left(x\right)$ are the Legendre polynomials. In this way, for Gaussian fluctuations, all the information is encoded in the multipole moments C_l, which are a measure of the temperature fluctuation on the angular scale $\theta\sim\pi/l$. Given an experiment, the value of C_l will be nonzero for angular scales larger than the resolution of the experiment and smaller than the patch of sky examined. In Figure 1.6 the CMB power spectrum measured by Planck is shown, where it has been defined the angular power spectrum

$$D_\ell^{TT}=\frac{l\left(l+1\right)C_\ell^{TT}}{2\pi}. \tag{1.41}$$

CMB polarization is mostly generated through Thomson scattering on the last scattering surface and to a small extent during the reionization era: this leads to a perturbation in the form of a gradient field on a sphere, called E-polarization. Gravitational waves, on the contrary, bring both a gradient (E) and a curl (B) component, but they are much more difficult to detect especially because lensing of scalar E-modes induces B-polarization [27]. It is possible to define two EE and BB *polarization anisotropy power spectra* in a similar way to the temperature one but, despite these two quantities could greatly help constraining cosmological parameters and bring informations about reionization and inflation, their precision is still limited by noise. An interesting property of temperature and polarization maps is that they superimpose quite well, showing they are strongly related one another. It is therefore possible to produce cross-correlation maps and power spectra measuring the angular or spatial correlation between two observables.

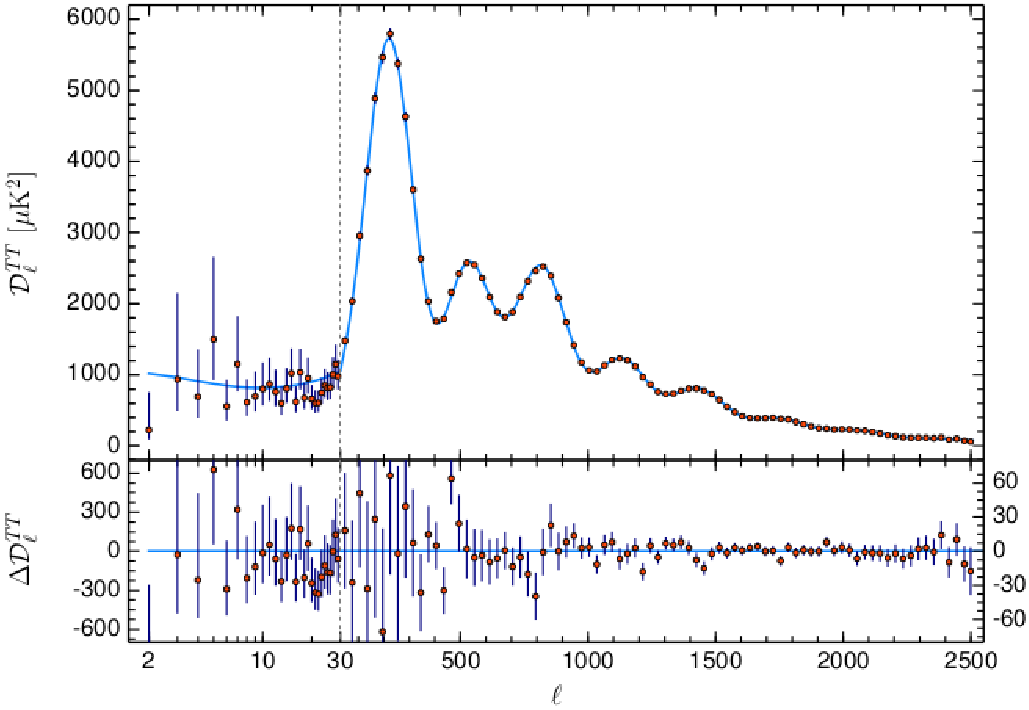

Figure 1.6: *Planck* 2018 CMB temperature power spectrum. The base-ΛCDM theoretical spectrum best fit to the TT,TE,EE+lowE+lensing likelihoods is plotted in light blue in the upper panel. Residuals with respect to this model are shown in the lower panel. The error bars show $\pm 1\sigma$ diagonal uncertainties, including cosmic variance (approximated as Gaussian) and not including uncertainties in the foreground model at $\ell \geq 30$. The vertical scale changes at $\ell = 30$, where the horizontal axis switches from logarithmic to linear [11].

Weak gravitational lensing

Another physical effect which affects photons is lensing. Due to gravitational potentials associated with density inhomogeneities, photons from distant galaxies are deflected from their original path and on small angular scales, like $l \gtrsim 1000$, the observed spectra can be changed in a relevant way.

Computing the effect of a gravitational lens, if the effective gravitational potential ϕ is such that $|\phi^2| \ll c^2$ and the lens is moving with respect to a cosmological frame with a velocity $v \ll c$, the deflection angle of the light ray is small and it is possible to take the gradient of the Newtonian potential perpendicular to the original unperturbed light path rather than the actual (perturbed) one. Considering the impact parameter b of the light ray as it crosses the lens plane and the relevant potential for a point lens

$\phi(b,z) = -\frac{GM}{\sqrt{b^2+z^2}}$, where z is the distance along the ray, the deflection angle can be written as

$$\hat{\alpha} = \frac{2}{c^2}\int \nabla_{\perp}\phi \, dz = \frac{4GM}{c^2 b}. \tag{1.42}$$

Large scale structures will cause distortions in the weak lensing limit, shearing galaxy images and also coupling adjacent l modes which would be otherwise uncorrelated. Computing the distortion permits to define the *lensing power spectrum*, which can probe fundamental physical quantities, such as the dark energy equation of state and neutrino masses, through its sensitivity to the geometry of the universe and the growth of structure.

Matter power spectrum

The most useful quantity to constrain neutrino properties, however, is the *matter power spectrum*. In Sec. 1.5 it has already been introduced the dimensionless density fluctuation $\delta(\vec{x}, a)$ and its Fourier components $\delta_{\vec{k}}$; in this case many models suggest that the primordial fluctuations, from which inhomogeneities have derived, should follow a Gaussian statistic. Their distribution is therefore completely determined by the matter power spectrum $P(k)$, defined as the two-point correlation function of non-relativistic matter fluctuations in Fourier space

$$P(k,z) = \left\langle \left| \delta_{\vec{k}(z)} \right|^2 \right\rangle, \tag{1.43}$$

where the average is taken over all possible orientations of the wavenumber $\vec{k}$. Since the energy density is related to the mass density of non-relativistic matter through $E = mc^2$, the equation refers indifferently to the energy or mass power spectrum. Depending on the redshift z, the matter power spectrum gives informations about the formation of structures during the Universe evolution. This allows to determine the densities of the various components of the Universe during its expansion, because each component has a different effect on structure formation and consequently it influences the shape of matter power spectrum. In Fig. 1.7 it is shown the matter power spectrum at $z = 0$ (today) from the ΛCDM model compared with values inferred from various experiments. In the next sections it will be examined the effect of different universe components, in particular neutrino masses, on the matter power spectrum.

1.5.2 Parametrizing ΛCDM

In 1980 the CDM model emerged, based on a flat geometry for the large scale Universe with a hierarchical formation of structures influenced by the distribution of dark matter at small scales. Adding a cosmological constant to this model makes possible to explain the CMB observations, the Universe large scale structure and its accelerated expansion,

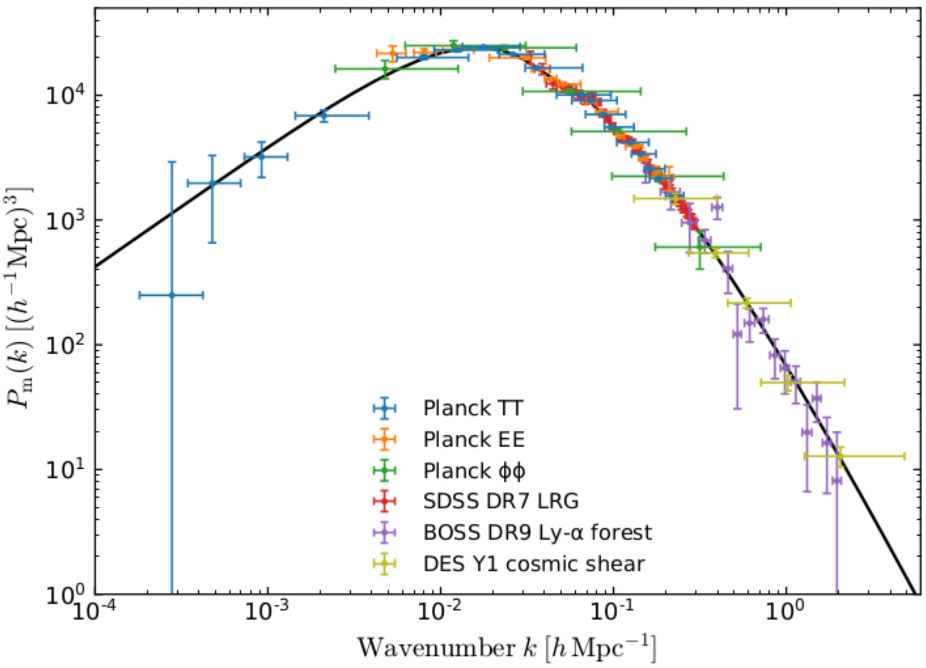

Figure 1.7: The (linear theory) matter power spectrum today inferred from different cosmological probes. The black line represents the ΛCDM model [23].

making the ΛCDM model capable to reproduce quite well the observations of Big Bang cosmology. The elements constituting this model, shown in Fig. 1.8, are dominated today by this cosmological constant, associated with dark energy, and cold dark matter. The model also includes radiation, baryonic matter and three neutrinos. Density anisotropies are assumed to result from the evolution of primordial power spectra.

A minimal flat ΛCDM model without neutrinos can be described with six independent parameters $(\omega_b, \omega_{cdm}, \theta_s, A_s, n_s, \tau_{reio})$. The first one is the baryon density $\omega_b = \Omega_b h^2$, while the second one is the density of cold dark matter $\omega_{cmd} = \Omega_{cdm} h^2$. The parameter θ_s is defined as the ratio between the sound horizon r_s and the angular diameter distance D_A at decoupling, where the sound horizon is defined as the comoving distance travelled by a sound wave by the conformal time τ, $r_s(\tau) \equiv \int_0^\tau d\tau' v_s(\tau')$, and the angular diameter distance D_A is defined as the ratio $D_A(z) = L/\theta$ between the proper size of an object and and its observed angular size. A_s and n_s are respectively the primordial density power spectrum amplitude and tilt. The last parameter, τ_{reio}, is the optical depth of CMB photons to reionisation. From the first two parameters, ω_b and ω_{cdm}, it is possible to derive the total non-relativistic matter density $\omega_m = \Omega_m h^2$ and, assuming a flat curvature, also the cosmological constant density parameter Ω_Λ.

These parameters control various physical effects which are responsible for the shape

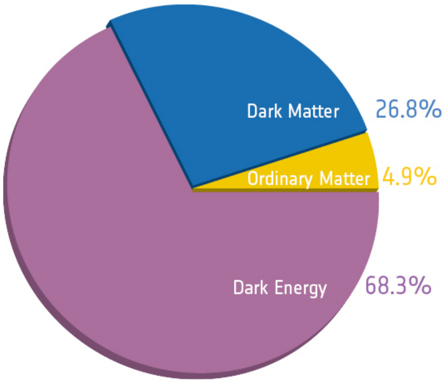

Figure 1.8: Composition of the Universe extracted from the Planck's CMB maps [28].

of the observable power spectra. While A_s, n_s and τ_{reio} have specific effects on the spectra (A_s fixes the global normalization of all spectra, n_s fixes the balance between large and small scale amplitudes and τ_{reio} damps the CMB temperature fluctuations for scales inside the Hubble horizon at the time of reionisation), Ω_Λ, ω_m and ω_b have intricate effects on the times of equality, on the balance in the photon-barion fluid, or on the amplitude of fluctuations. Nevertheless, since there are various effects for six parameters, it is in principle easy to measure all of them from CMB and Large Scale Structure (LSS) data, assuming a flat ΛCDM model.

1.5.3 ΛCDM model with massive neutrinos

Describing neutrino properties is one of the current goals of physics, but with present experiments it is only possible to put some upper limits on the sum of their masses with cosmology, or to study them with oscillation experiments on Earth. Neutrinos influence on cosmology can constrain much better their properties because, although it is still not possible to directly detect the relic neutrinos, their presence greatly influence the evolution of structures in time, thus many observable quantities and in particular the power spectra.

Hot neutrinos

It is assumed that, after the primordial inflation, the primordial power spectrum for density perturbations is described by the function $P(k) \propto k^n$, with $n = 1$ predicted by most inflationary models. During the radiation domination, it will change depending on the properties of dark matter that starts to clump. In this phase neutrinos, that have decoupled at $t \sim 1\,\mathrm{s}$ and that had a temperature of $kT \sim 1\,\mathrm{MeV}$ in equilibrium with the universe at the time of decoupling, are relativistic and act as hot dark matter (HDM), smoothing and erasing density contrasts on wavelengths smaller than their free-streaming scale equal to the Hubble radius. This primordial neutrinos form a *cosmic neutrino background*, predicted by the standard hot big bang model and similar in number to the photons of the CMB. Their spectrum is the same as the plasma at the moment of decoupling, due to the fact that the decoupling itself can be considered instantaneous in a good approximation. Right after decoupling neutrinos have some residual interactions with the $e^{\pm}$ and, during the $e^{\pm}$ annihilation heating photons, this interactions distort the spectra for the higher neutrino energies, more sensible to this type of relic interactions. The neutrino spectra for high energies also depend on neutrino flavour oscillations, the distortions growing with the neutrino momentum. To calculate the perturbation evolution, in principle, it should be necessary to include all these contributions for each mass eigenstate, as in calculations done with the Boltzmann code CLASS that will examined in Sec. 3.3. When calculating quantities that do not depend on neutrino masses, however, this distortions can be integrated and one can take them into account, for example calculating the total energy density and its relativistic neutrino contribution, just by using the integrated value $N_{eff} = 3.046$. These distortions therefore have only small consequences during perturbation growth and are easily taken into account or safely neglected.

During the era of radiation domination, neutrinos contribution can be considered together with the radiation one to determine the total radiation density responsible of expansion. This total radiation density can be parametrized in term of the previously introduced number of effective neutrinos $N_{eff} = 3.046$:

$$\rho_R = \left[1 + \frac{7}{8}\left(\frac{4}{11}\right)^{4/3} N_{eff}\right]\rho_\gamma, \tag{1.44}$$

with ρ_γ the energy density of photons known from the CMB temperature. Any measured value departing from $N_{eff} = 3.046$ can be a sign of new physics or other contributions, like for example sterile neutrinos described in Sec. 1.1.3. The neutrino density in addition can not be too high to avoid a too fast closure of the universe and given the contribution of matter $\Omega_m \simeq 0.3$ their mass is bounded to be $\lesssim 5\,\mathrm{eV}$ [29].

The contribution of relativistic neutrinos as HDM only have a small impact on the universe evolution. Observations showed that galaxies are older than clusters and the characteristic of hot neutrinos to erase perturbations during their free-streaming makes their contribution less significant than the ones from other components of the universe.

Cooling down during expansion, neutrinos become non-relativistic and their velocity drops like

$$v_{th} \equiv \frac{\langle p\rangle}{m} \simeq \frac{3T_\nu}{m} = \frac{3T_\nu^0}{m}\left(\frac{a_0}{a}\right) \simeq 150\,(1+z)\left(\frac{1\,\mathrm{eV}}{m}\right)\ \mathrm{km\,s^{-1}}, \tag{1.45}$$

where $T_\nu^0 \simeq (4/11)^{1/3}\, T_\gamma^0$ and $T_\gamma^0 \simeq 2.726$ K. The non-relativistic regime is reached at a redshift

$$z_{n\nu} \simeq 2 \times 10^4 \frac{\langle m_\nu \rangle}{10\,\mathrm{eV}} \simeq \frac{2 \times 10^5}{N_\nu} \Omega_\nu h^2, \tag{1.46}$$

and neutrinos start behaving like cold dark matter (CDM).

Growth of neutrinos density contrasts

During their relativistic regime, neutrinos density perturbations are damped to zero, but after their non-relativistic transition and when the universe becomes matter dominated at $z \simeq 3300$, their presence becomes significant enough to modify the evolution of perturbations. Although non-relativistic neutrinos do not contribute to gravitational clustering on scales smaller than the free-streaming scale, they in fact contribute to the homogeneous expansion through the Friedmann equation (see Eq. 1.30).

Without neutrinos, during matter domination super-Hubble modes of density perturbations remain constant, while sub-Hubble modes grow slowly like a. Introducing neutrinos, after their non-relativistic transition their density evolution is governed by the equation

$$\ddot{\delta}_\nu + \frac{\dot{a}}{a}\dot{\delta}_\nu = -k^2\phi + 3\left(\ddot{\psi} + \frac{\dot{a}}{a}\dot{\psi}\right), \tag{1.47}$$

where the metric perturbations ϕ and ψ are from the Eq. 1.12 written in the longitudinal gauge

$$ds^2 = g_{\mu\nu}dx^\mu dx^\nu = a^2(\tau)\left[(1+2\phi)\,d\tau^2 - (1-2\psi)\,\delta_{ij}dx^i dx^j\right]. \tag{1.48}$$

The density contrast for neutrinos δ_ν will thus evolve differently for modes inside or outside the Hubble radius at the time of non-relativistic transition.

- For modes inside the Hubble radius when neutrino enter in the non-relativistic regime ($k > k_{nr}$) the neutrinos density contrast is much smaller than the cold dark matter one as a consequence of free streaming, but it starts to grow faster than $\delta_{cdm} \propto a$. This difference tends to decrease with time and asymptotically the growth of neutrino inhomogeneities will be $\delta_\nu \propto a$, but for $\lesssim 1\,\mathrm{eV}$ massive neutrinos this will not happen as fast as the heaviest ones or as baryons.

- For modes outside the Hubble radius at the times of transition ($k < k_{nr}$) the density contrast δ_ν does not depend on time and is of the same order as the cold dark matter one, then after the horizon crossing it rapidly becomes equal to δ_{cdm}. Neutrino perturbation modes with small wavenumber are in fact never affected by free streaming and evolve as cold dark matter, like in a pure ΛCDM model. The three density contrasts δ_ν, δ_{cdm} and δ_b will thus be one equal to another for modes smaller than k_{nr} and the ratio $\delta_\nu/\delta_{cdm} = \delta_\nu/\delta_b$ will be smaller than one and tending towards zero as k increases.

The recent stage of Λ domination does not change significantly these considerations, and one would expect that the matter power spectrum today will be

$$P\left(k\right)=\left\langle\left(\frac{\delta\rho_{cdm}+\delta\rho_b+\delta\rho_\nu}{\rho_{cdm}+\rho_b+\rho_\nu}\right)^2\right\rangle=\left\langle\left(\frac{\Omega_{cdm}\delta_{cdm}+\Omega_b\delta_b+\Omega_\nu\delta_\nu}{\Omega_{cdm}+\Omega+\Omega_\nu}\right)^2\right\rangle$$
$$=\begin{cases}\langle\delta^2_{cdm}\rangle & \text{for } k<k_{nr},\\ \left[1-\Omega_\nu/\Omega_m\right]^2\langle\delta^2_{cdm}\rangle & \text{for } k\gg k_{nr},\end{cases}\qquad(1.49)$$

with $\Omega_m\equiv\Omega_{cdm}+\Omega_b+\Omega_\nu$.
Neutrinos presence, however, modifies the evolution of matter perturbations introducing a heavier suppressing factor in the $P\left(k\right)$. This effect involves both the background evolution through the density and pressure of neutrinos, which affect the expansion rate, and directly the matter and metric perturbations, even for scales bigger than their free streaming length.

Effects of neutrinos on the growth of matter perturbations

Without neutrinos, it is shown that inside the Hubble radius the density contrast $\delta_{cdm}=\delta_b$ gives a total density perturbation $\delta\rho=\left(\bar\rho_{cdm}+\bar\rho_b\right)\delta_{cdm}$ and an expansion rate of $3\left(\dot a/a\right)^2=8\pi Ga^2\left(\bar\rho_{cdm}+\bar\rho_b\right)\propto a^{-1}$, with a scale factor $a\propto\tau^2$. The equation for the perturbations evolution is

$$\ddot\delta_{cdm}+\frac{2}{\tau}\dot\delta_{cdm}-\frac{6}{\tau^2}\delta_{cdm}=0,\qquad(1.50)$$

with a growing solution $\delta_{cdm}\propto a$. The combination between the gravitational clustering and the stretching of spacetime thus balance themselves.

Introducing massive neutrinos, they only contribute to the homogeneous expansion through the Friedmann equations. During matter domination and on scales smaller than the free streaming length, neutrino perturbations do not in fact contribute to gravitational clustering both because they are much smaller compared to the CDM ones and because of the difference in the mean densities itself $\bar\rho_\nu<\bar\rho_{cdm}$. The expansion rate therefore becomes $3\left(\dot a/a\right)^2=8\pi Ga^2\left(\bar\rho_{cdm}+\bar\rho_b+\bar\rho_\nu\right)$ and, if $\bar\rho_\nu$ is dominated by non-relativistic neutrinos (so it decays like a^{-3}) and the number

$$f_\nu\equiv\frac{\rho_\nu}{\rho_{cdm}+\rho_b+\rho_\nu}=\frac{\Omega_\nu}{\Omega_m}\ll 1\qquad(1.51)$$

is approximately constant, the scale factor will evolve like τ^2 and the equation for the perturbations evolution becomes

$$\ddot\delta_{cdm}+\frac{2}{\tau}\dot\delta_{cdm}-\frac{6}{\tau^2}\left(1-f_\nu\right)\delta_{cdm}=0,\qquad(1.52)$$

with an approximate growing solution of $\delta_{cdm}\propto a^{1-\frac{3}{5}f_\nu}$: the growth is thus reduced.

Difference between effects of massless and massive neutrinos

The main difference between $P(k)$ of models with massless or massive neutrinos can be seen for small scales. For greater scales and smaller k the spectrum is the same, because if all parameters are equal except for the values of ω_ν and $\omega_{cdm} = \omega_m - \omega_b - \omega_\nu$, perturbations are not affected by neutrinos free-streaming as seen before. For $k \gg k_{nr}$ and $k \gg k_{eq}$ there are two main differences:

- The equality does not take place for the same value of the scale factor a. Being the ratio $(a_{eq}/a_0) = \omega_r/(\omega_b + \omega_{cdm}) = (1 - f_\nu)^{-1} \omega_r/\omega_m$, with ω_r including not only the density of photons but also the one of massless neutrinos, at equality it is easily seen that $a_{eq}^{f_\nu}/a_{eq}^{f_\nu=0} = (1 - f_\nu)^{-1}$. As a consequence from equality and before the non-relativistic transition the two models only differ in a factor
$$\delta_{cdm}^{f_\nu}[a] = \delta_{cdm}^{f_\nu=0}[(1 - f_\nu)\, a]\,. \tag{1.53}$$
- After the non-relativistic transition, as seen in the solution of Eq. 1.52, the growth of CDM perturbation is slowed down and becomes
$$\delta_{cdm}^{f_\nu}[a_0] = \left(\frac{a_0}{a_{nr}}\right)^{1-\frac{3}{5}f_\nu} \delta_{cdm}^{f_\nu}[a_{nr}]\,, \tag{1.54}$$
while for the massless case numerical results show that the growth is given by
$$\delta_{cdm}^{f_\nu=0}[a_0] \simeq \left(\frac{a_0}{(1 - f_\nu)^{1/2} a_{nr}}\right) \delta_{cdm}^{f_\nu=0}[(1 - f_\nu)\, a_{nr}]\,. \tag{1.55}$$
Using Eq. 1.49 and replacing a with its value during Λ domination ($a\, g(a)$, with $g(a)$ normalized to $g = 1$ for $a \ll a_\Lambda$), the total matter power spectrum is reduced by
$$\frac{P(k)^{f_\nu}}{P(k)^{f_\nu=0}} = (1 - f_\nu)^3 \left(\frac{a_0\, g(a_0)}{a_{nr}}\right)^{-\frac{6}{5}f_\nu}. \tag{1.56}$$
It is possible to obtain this equation showing its dependence by the number of neutrinos N_ν and by the value $f_\nu = \frac{\Omega_\nu}{\Omega_m}$
$$\frac{P(k)^{f_\nu}}{P(k)^{f_\nu=0}} = (1 - f_\nu)^3 \left[1.9 \times 10^5 g(a_0)\, \omega_m f_\nu / N_\nu\right]^{-\frac{6}{5}f_\nu} \tag{1.57}$$
replacing a_0/a_{nr} with $2000\, m_\nu/(1\,\mathrm{eV})$ and using $m_\nu = (\omega_\nu/N_\nu)\, 93.2\,\mathrm{eV}$ if all the neutrino mass is shared by N_ν families [29].

This equation is a very good approximation of the exact numerical results, but it is possible to obtain another useful linear approximation for $f_\nu < 0.07$, using plausible values of ω_m, N_ν and Ω_Λ as shown in Ref. [29]:
$$\frac{P(k)^{f_\nu}}{P(k)^{f_\nu=0}} \simeq -8 f_\nu. \tag{1.58}$$

Effects of non-degenerate neutrino masses on power spectra To probe the single neutrino masses, and consequently the normal or inverted ordering, it is necessary to examine more precisely the matter power spectrum. Effects on the CMB power spectra of different values of mass eigenstates are in fact only indirect and depend on the total mass M_ν. Studying the $P\left(k\right)$ it has been previously showed that the position of the break is related to the value of k_{nr}, the time of non-relativistic transition which depend on the individual mass of the neutrino m_ν. The amplitude of the break depends instead on both values of the total mass M_ν and the separate masses m_ν, respectively through f_ν and a_{nr}. The total mass has however the most important effect on the shape of the $P\left(k\right)$ and very precise measures are needed to constrain the single mass values. In Ch. 4, for this reason, only models with degenerate active neutrino masses will be examined.

1.6 Discrepancies between measurements of cosmological parameters

1.6.1 H_0 tension

The values of the six parameters for the ΛCDM model have been inferred from a number of independent experiments in the last decades, but especially for the Hubble constant H_0, which express the expansion rate of our Universe, a disagreement between the measurements has emerged.

The measurements of H_0 come in fact from two types of experiments:

- **Early universe observations** This type of experiments interpret measurements from the primordial epoch of the universe, such as CMB, BAO (Baryon Acoustic Oscillations) and BBN, to estimate the value of parameters such as H_0. This prediction is done applying our knowledge of the early universe physics, so it is strongly dependent from guesses about the nature of dark matter and dark energy and from the list of particles considered in the model. The most precise measurement nowadays is from the Planck experiment, which gives a result of $H_0 = (67.37 \pm 0.54)\ \mathrm{km\,s^{-1}Mpc^{-1}}$, but another completely independent measurement from the Dark Energy Survey (DES) weak lensing with BAO and BBN provides the same value with a different precision, as showed in the upper panel of Fig. 1.9.

- **Late universe observations** The more direct method to measure the present rate of expansion of the universe is through the building of a *distance ladder*, a series of methodologies used to calibrate the luminosity of particular stars in order to measure the cosmic expansion. The use of parallax to determine the distance of cosmological objects can be used only within a fraction of the Milky Way, so it is necessary to study other luminous and more distant objects such as Cepheids and

type Ia Supernovae (SN Ia). The first ones are supergiant stars with luminosities that reach 100 000 times that of the Sun, whose period of variation strongly correlates with their luminosities, while the second ones are a family of stars with very similar masses, which exploding reach a peak of 10 billion solar luminosities but occur about once a century in a galaxy.
There have been some experiments which have obtained similar values for H_0, listed in the middle panel of Fig. 1.9. The SH0ES (Supernovae H_0 for the Equation of State) project expanded and improved the calibrations of SN Ia by Cepheids; H0LiCOW (H_0 Lenses in COSMOGRAIL's Wellspring) measured the time delays between multiple images of background quasars to constrain the different image path lengths caused by the strong gravitational lensing from a foreground galaxy; the Megamaser Cosmology Project (MCP) uses observations of water masers (sources of microwave stimulated emission) orbiting around black holes to measure geometric distances; the CCHP collaboration substituted, for the calibration of SN Ia, the Cepheids with the Tip of the Red Giant Branch (TRGB, the peak brightness reached by red giant stars after they stop fusing hydrogen and begin fusing helium in their core); measurements from Miras (variable, oxygen-rich red giant stars) have allowed another type of calibration of SN Ia alongside the ones with Cepheids and TRGB and the IR Surface Brightness Fluctuations (SBF) have provided an H_0 local measurement independent of the use of SN Ia.

The comparison of results from these two types of experiments, which References can be found in [30] and showed in Fig. 1.9, makes evident that all recent local measurements exceed the early universe prediction by at least 4σ. This could be interpreted as an hint for new physics beyond ΛCDM that could resolve the discrepancy. In Ref. [30, 31] are listed some of the possible theoretical solutions proposed.

1.6.2 σ_8 tension

The parameter $\sigma_8(z)$ is the root mean square fluctuation of density perturbations at $8\,h^{-1}$Mpc scale, at redshift $z = 0$, and its value represents the matter power spectrum amplitude. The Planck experiment has inferred its value to be $\sigma_8 = 0.8101 \pm 0.0061$ for a base-ΛCDM model [11], or equivalently $S_8 \equiv \sigma_8 \left(\Omega_m/0.3\right)^{0.5} = 0.830 \pm 0.013$, but these values do not agree with the ones inferred from LSS observations. Cosmic shear measurements from experiments such as Canada-France-Hawaii Telescope Lensing Survey (CFHTLenS), DES and Kilo Degree Survey (KiDS) have found lower values for σ_8 with respect to Planck, but the tension is below the 3σ level and not as dramatic as for H_0. In Fig. 1.10 are shown constraints in the $\Omega_m - \sigma_8$ plane for DES, KiDS and Planck. In particular the DES cosmic shear constraint (green) is of comparable statistical power to CMB lensing (grey), but the degeneracy directions are different.

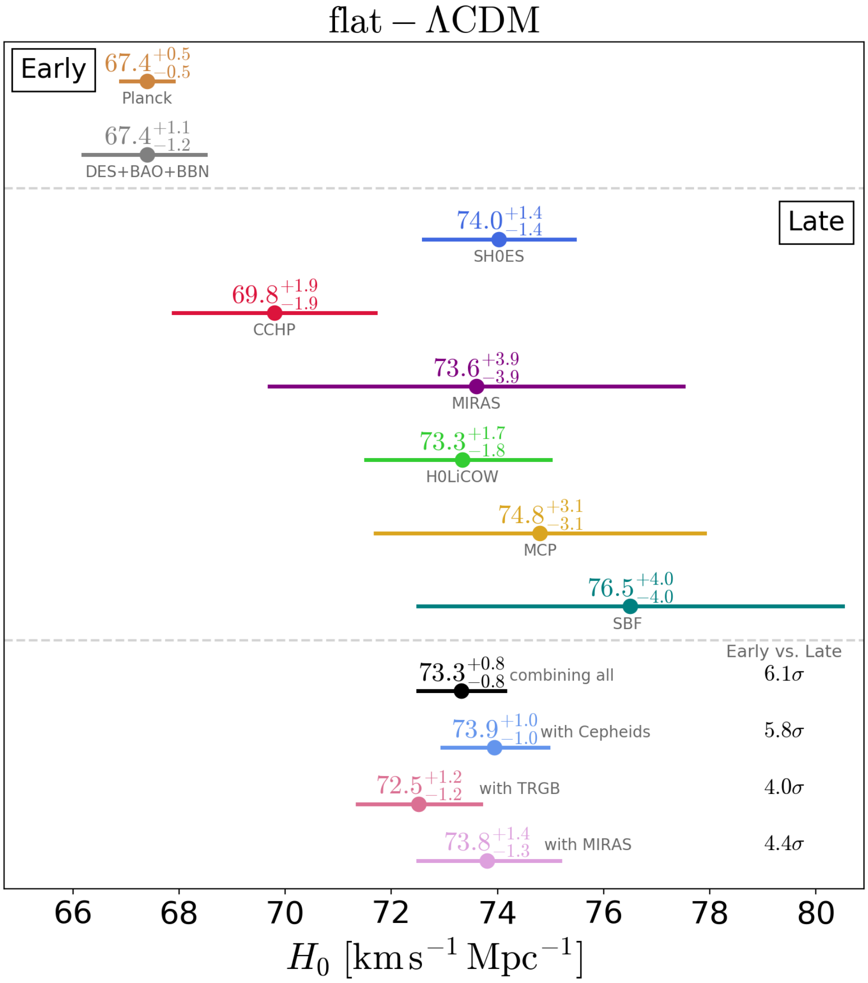

Figure 1.9: H_0 tension between early and late measurements [30]. In the bottom panel are shown some combinations of the late measurements using only one of the results from Cepheids, TRGB and Miras at a time, because of the overlap in data between these three methods.

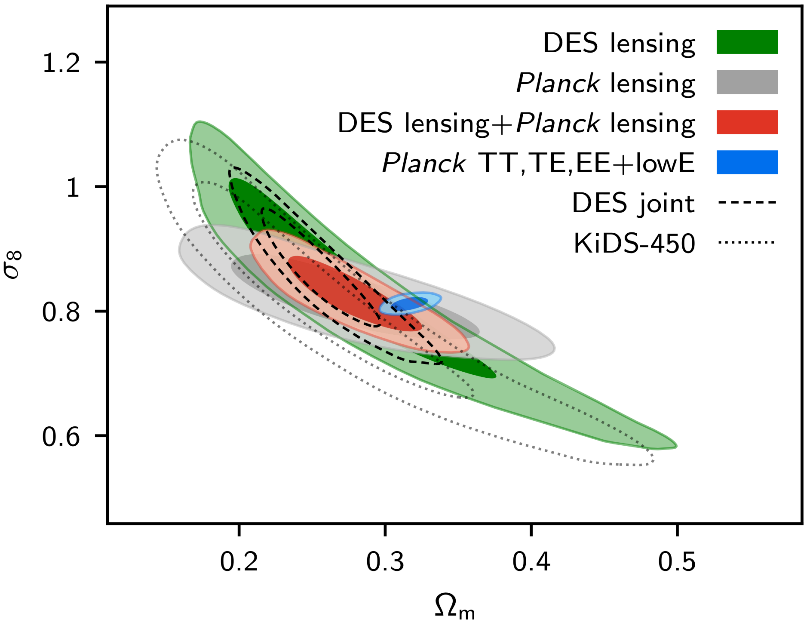

Figure 1.10: σ_8 tension between CMB and LSS measurements [11] for a base-ΛCDM model. The constraint contours on the matter-density parameter Ω_m and fluctuation amplitude σ_8 shown are 68% and 95% CL.

Chapter 2

EUCLID

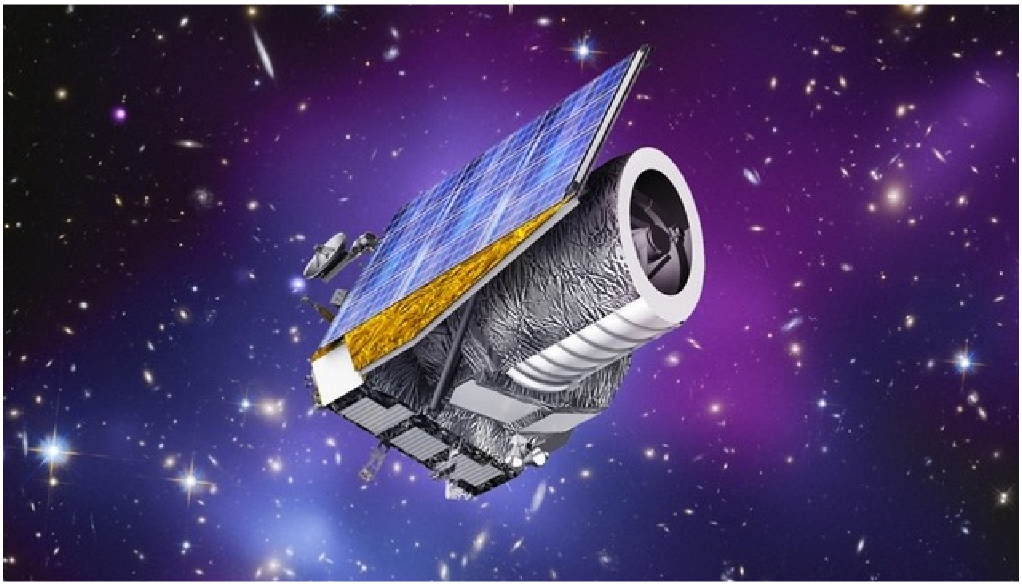

Figure 2.1: An artistic view of the Euclid's spacecraft.

Euclid is an European Space Agency (ESA) mission, which has the main goal to investigate the nature of dark matter and dark energy, which constitute the main components of the energy budget of the Universe. It will also verify General Relativity on large scales and it will investigate the primordial Universe.

The Euclid launch on a Soyuz ST 2.1-B rocket is scheduled in 2022 from Kourou Space Center (French Guiana) and, after reaching the second Sun-Earth Lagrange point L2, 1.5 million km from Earth, it will observe the universe with a wide survey of $15\,000\,\mathrm{deg}^2$ of the extragalactic sky, complemented by two $20\,\mathrm{deg}^2$ deep fields observed on a monthly basis. The L2 point offers optimum operating conditions for Euclid: a benign radiation environment, necessary for the sensitive detectors, and observing conditions sufficiently far away from the Earth-Moon system. The experiment, whose artistic reproduction is showed in Fig. 2.1, is equipped with a 1.2 m diameter telescope, with a field of view of about $0.54\,\mathrm{deg}^2$, and will take about 6 years to complete the wide survey with the deep survey interspersed. The calibration of the instruments will be mostly done in the first year, pointing to specific calibration targets as white dwarfs, planetary nebulae and dense stellar fields.

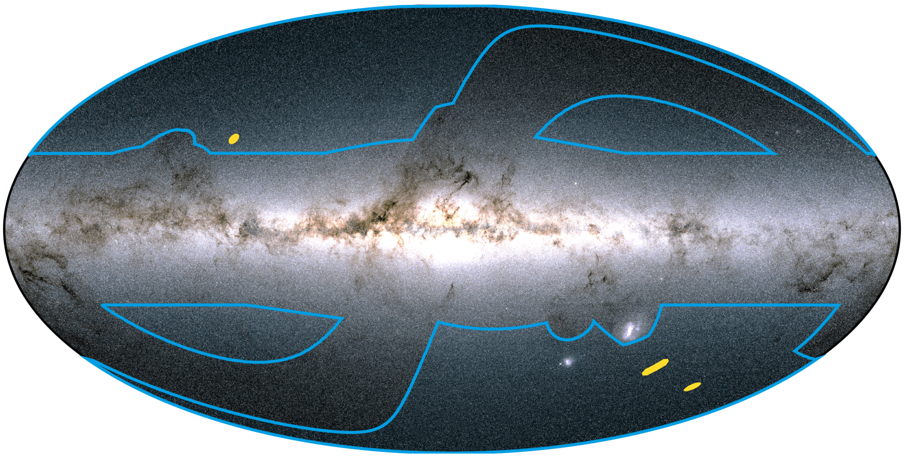

Figure 2.2: A representation of the areas covered by Euclid's wide (blue) and deep (yellow) surveys on an all-sky map in the Galactic coordinate system. The bright horizontal band correspond to the plane of the Milky Way galaxy, where most of the stars reside, avoided together with the regions of the sky dominated by interstellar matter or by diffuse dust in the Solar System.

The *wide survey* consists in a scanning of the extragalactic sky (defined by the regions covering $|b| > 30$ degrees with respect to the galaxy plane) in a *step-and-stare* mode, with the telescope pointing to a position on the sky and performing imaging and spectroscopic measurements on an area of ~ 0.5 deg^2 around this position. Being necessary to keep the thermal stability of the spacecraft, Euclid is also equipped with a sunshield, which is maintained orientated towards the Sun. The pointing direction has therefore to be as much as possible perpendicular to the Sun-spacecraft axis, making the viewing area on each day confined to a circle perpendicular to this axis.

The *deep survey* consists instead of repeated scanning of the same areas on the sky at regular intervals during the mission and will cover ~ 40 deg^2, consisting of patches of at least 10 deg^2, about 2 magnitudes deeper than the wide survey. The Euclid Deep fields are respectively the Euclid Deep Field North, located in the northern sky and of 10 square degrees, plus the Euclid Deep Field Fornax, spanning 10 square degrees, and the Euclid Deep Field South, spanning 20 square degrees, both in the southern sky.

The areas of these fields of view, showed in Fig. 2.2, have been optimized to obtain the necessary figure of merit *FoM* for the dark energy measurement, defined as the reciprocal ratio of the product of the $1\,\sigma$ error on the parameters w_0 and w_a seen in Eq. 1.28, and to improve the sensitivity on the parameters γ, f_{NL} and m_ν, described in Section 2.1. They respectively are a General Relativity modification index which influences the growth of primordial density perturbations, the weight for non-Gaussianity correction in the primordial density fluctuations and the sum of neutrino masses. The scientific requirements will be further examined in Section 2.1. To obtain the expected sensibility, the experiment is equipped with two instruments, a camera which will obtain visible images called VIS (VISible imager) and and one capable of both NIR imaging and slitless spectroscopy, called NISP (Near Infrared Spectro-Photometer). The two instruments will be examined more in detail in Section 2.2.

2.1 Science objectives

An essential parametrization of the evolution of the universe can be done using the parameters γ, f_{NL}, w_0, w_a and m_ν. They in fact summarise the universe expansion, clusterisation and composition and their precise knowledge is crucial to create a reliable model for the growth of all structure in our universe.

- Testing the General Relativity at large scales, it is possible to introduce the *growth factor*

  $$f\left(\Omega\right) \equiv \frac{d\,\log\delta}{d\,\log a}, \tag{2.1}$$

  where the density contrast defined in Eq. 1.35 determines together with the scale factor the growth of inhomogeneities in an Einsteinian universe [32]. The growth depends on the density fraction Ω defined in Eq. 1.18 and an useful approximation for models without a cosmological constant Λ is

  $$f\left(\Omega\right) \simeq \Omega^\gamma, \tag{2.2}$$

  with the value of the density fraction being referred to the sum of all the different components densities. Introducing the cosmological constant, the growth factor is only slightly affected and a better fit can be written as

  $$f\left(\Omega, \Omega_\Lambda\right) \simeq \Omega^\gamma + \frac{\Omega_\Lambda}{70}\left(1 + \frac{1}{2}\Omega\right). \tag{2.3}$$

  The parameter γ is close to 0.55 for standard relativistic gravity, but can differ by around 0.1 from this value in many non-standard models [9]. The current error on this value is given by [33] and is of 0.2; with Euclid it is expected to improve this value of a factor 30 [34], permitting to probably understand the cause of the cosmic acceleration.

- An important characteristic of the cosmological model, it is the assumption regarding the *Gaussianity* of the initial random field of perturbations, already introduced in Sec. 1.5.1 and necessary for the definition of the power spectra. In many inflationary models, however, it is expected a small deviation from this Gaussian probability distribution, parametrized with the term f_{NL}, which could affect the evolution of inhomogeneities. Positive distortion will cause, for example, a bigger probability for large overdensities, bringing to the formation of greater objects at earlier times. A simple model to parametrize the primordial non-Gaussianity is the gauge-invariant Bardeen's potential

  $$\Phi(\mathbf{x}) = \Phi_G(\mathbf{x}) + f_{NL}\left(\Phi_G^2(\mathbf{x}) - \left\langle \Phi_G^2(\mathbf{x}) \right\rangle\right), \tag{2.4}$$

  where $\Phi_G(\mathbf{x})$ denotes the linear Gaussian part of the perturbation and f_{NL} the weight for the second-order non-linear term [35]. The current best limit for f_{NL} comes from Planck, and is $f_{NL} = -0.9 \pm 5.1$ [23].
  Another parametrization for non-Gaussianity is the slope of the primordial matter power spectrum n_s, for which the best measurement also comes from Planck and gives $n_s = 0.967 \pm 0.004$ [23].

- The parameters w_0 and w_a have been introduced in Sec. 1.4.3 and describe the equation of state of dark energy, considered as a field evolving along with the universe and not a simple cosmological constant. The equation of state and its dependence from redshift are shown in Eq. 1.28.

- The last relevant parameter examined is the sum of *neutrino masses* $M_\nu = \sum_i m_{\nu_i}$, which has been examined in detail together with its consequences on the evolution of the Universe in Chapter 1.

Improving the constraints on these parameters will be the goal of Euclid, through the observation and study of two independent probes: the weak gravitational lensing and the galaxy clustering.

2.1.1 EUCLID primary probes

The choice as primary probes of the weak lensing and of the galaxy clustering has been done because they are the most sensitive to the effects of dark energy and can be efficiently used to verify the General Relativity on large scales. Their combination, in addition, gives strong constraints on the growth of structures and on the relation between the dark and luminous matter, keeping errors low. This remains true even at small scales, where baryonic effects become important, because Euclid will be able to correct them through the baryonic feedback mechanism [34].

Cosmic shear

Cosmic shear is a distortion of background galaxies images due to the effect of the mass distribution along the line-of-sight of these distant galaxies, called *weak gravitational lensing*. Galaxies images are distorted due to the gravitational field, induced by large scales structures, that deviates the photons and, working in the weak regime, these distortions are much smaller that the galaxies intrinsic ellipticity. Observing the Universe at different times, i.e. at different redshift, it is thus possible to correlate the distortions at the various epochs, reconstructing the masses distribution between the observer and the source.

These measurements, dealing with very small variation in the apparent shapes of background galaxies (less than a 1% change in a galaxy ellipticity), require high-quality images to perform an accurate evaluation of the weak lensing galaxy shear, plus photometry at visible and infrared wavelengths in order to measure the distances of each lensed galaxy out to redshift $z \leq 2$, with a precision of $\sigma_z/(1+z) < 0.05$ [34]. They also require a minimum density of galaxies in the observed area to extract a measurable signal, averaging over many galaxies because of the little shear, and a wide knowledge of the instrument to correct systematic effects as optical aberration, which could simulate the shear effect. The galaxy shape measurement also requires some criteria to be useful: the radius of the galaxy must be larger than 1.25 times the point-spread function (PSF, the response of the detector to a point source) and the signal-to-noise ratio must be of at least 10 [34]. A number density of 30 galaxies per arcmin^2 has been calculated for almost all source galaxies be useful for weak lensing, meeting these criteria.

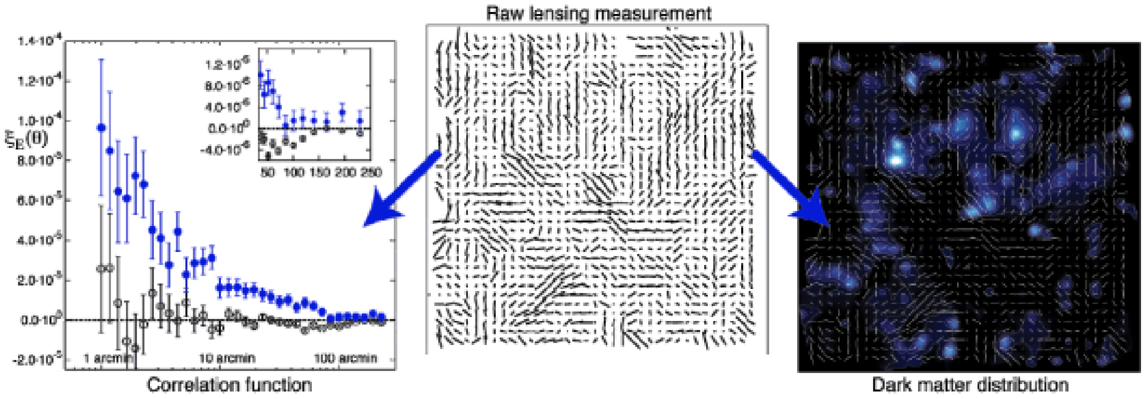

Figure 2.3: Study of the dark matter distribution using weak lensing. Datas are from HST observations. [34].

An example of the dark matter field reconstruction from the cosmic shear measurement is shown in Fig. 2.3, taken from the HST (Hubble Space Telescope) mission. The lines in the middle panel represent the average ellipticity of about 200 galaxies, with the line length representing the magnitude of the lensing effect and the orientation showing the direction of the major axis. In the right panel it is shown how dark matter lenses are mapped, filtering the observed shear (the distribution of mean ellipticity) for the circular patterns. In the left panel the clumpiness of dark matter on different scales is quantified, correlating the shear effect along different line-of-sights (ground-based-results from [36]).

The cosmological information from cosmic shear is extracted using auto- and cross-correlations functions, related to the matter distribution.

All weak lensing quantities can in fact be defined as a function of the lensing potential $\psi\left(\boldsymbol{\theta}\right)$, that arises from the gravitational potential integrated along the line of sight at the position $\boldsymbol{\theta}$ in the sky and that can be expanded in spherical harmonics as

$$\psi\left(\boldsymbol{\theta}\right) = \sum_{l,m} \psi_{lm} Y_l^m\left(\boldsymbol{\theta}\right). \tag{2.5}$$

The effect of this field is to modify the galaxy image, both in size and shape, so it is possible to define two quantities: the convergence κ and the shear $\boldsymbol{\gamma}$.

The lensing convergence κ is a scalar field that depends on the mass density fluctuation field defined in Eq. 1.35 as [37]

$$\kappa\left(\boldsymbol{\theta}, r\right) = \frac{3H_0^2\Omega_m}{2c^2} \int_0^r dr' \frac{r'\left(r - r'\right)}{r} \frac{\delta\left(\boldsymbol{\theta}, r'\right)}{a\left(r'\right)} \tag{2.6}$$

and can be written also as a function of the lensing potential

$$\kappa = \frac{1}{2}\left(\partial_1^2 + \partial_2^2\right)\psi, \tag{2.7}$$

where the partial derivatives ∂_i are with respect to the two angular coordinates of the position in the sky θ_i, with $i = 1, 2$. These parameter expresses the isotropic magnification of the galaxy image.

The complex shear is instead a pseudo vector field $\boldsymbol{\gamma} \equiv \gamma_1 + i\gamma_2 = \gamma e^{-2i\alpha}$, where α is the orientation angle of the shear. Its two components are

$$\gamma_1 = \frac{1}{2}\left(\partial_1^2 - \partial_2^2\right)\psi \qquad \text{and} \qquad \gamma_2 = \partial_1\partial_2 \tag{2.8}$$

and it expresses the deformation of the galaxy image from circular to elliptical, without changing its area.

In order to obtain information about the mass distribution along the line of sight, at first it is calculated the two-point correlation function of the shear for source galaxies in the i-th and j-th redshift bin from the observed galaxies catalogue, to quantify the lensing signal. The obtained correlation function is

$$\xi_{\gamma_i\gamma_j}\left(\theta\right) = \left\langle \boldsymbol{\gamma}_i\left(\boldsymbol{\theta}_1\right) \boldsymbol{\gamma}_j^*\left(\boldsymbol{\theta}_2\right)\right\rangle, \tag{2.9}$$

with $\theta = |\boldsymbol{\theta}_1 - \boldsymbol{\theta}_2|$. This can also be decomposed in two components, one depending on the tangential component of the shear $\gamma_t = -\Re\left(\gamma e^{-2i\alpha}\right)$ and the other one at 45°, depending on the cross-component $\gamma_r = -\Im\left(\gamma e^{-2i\alpha}\right)$, that are respectively defined as tangential $\xi_{tt}(\theta) = \langle \gamma_{it}(\boldsymbol{\theta}_1)\,\gamma_{jt}(\boldsymbol{\theta}_2)\rangle$ and rotated $\xi_{rr}(\theta) = \langle \gamma_{ir}(\boldsymbol{\theta}_1)\,\gamma_{jr}(\boldsymbol{\theta}_2)\rangle$ ellipticity correlation functions. It is also possible to define

$$\xi_{\pm}(\theta) \equiv \xi_{tt}(\theta) \pm \xi_{rr}(\theta) \tag{2.10}$$

and the E and B modes (useful to test systematics, as the intrinsic alignment of galaxies or errors on the PSF)

$$\xi_{E,B}(\theta) = \frac{\xi_{+}(\theta) \pm \xi'(\theta)}{2}, \quad \text{being} \quad \xi' = \xi_{-}(\theta) + \int_{\theta}^{\infty} \frac{d\vartheta}{\vartheta}\xi_{-}(\vartheta)\left(4 - 12\left(\frac{\theta}{\vartheta}\right)^{2}\right). \tag{2.11}$$

All these two-point correlation functions can be written as integrals over the convergence power spectrum, that, as seen before, is related to the mass distribution and to the three-dimensional matter power spectrum.

It is possible to demonstrate [38] that, using Poisson's equation, the angular power spectrum of the lensing potential

$$\langle \psi_{lm}\psi_{l'm'}\rangle = C_l^{\psi\psi}\delta_{ll'}\delta_{mm'} \tag{2.12}$$

can be related to the three-dimensional matter power spectrum $P(k)$ and, making use of the weak lensing tomography (i.e. binning the redshift space), the shear auto or cross-correlation power spectrum can be written as

$$C_l^{ij} = \int_0^{\infty} dz \frac{c}{H(z)} \frac{W_i(z)\,W_j(z)}{r^2(z)} P(k,z), \tag{2.13}$$

where $r(z)$ is the comoving distance to redshift z and $W_i(z)$ is the window function for the i-th redshift bin, describing the normalised distribution of sources $n_i(z_s)$ in it and its lensing efficiency

$$W_i(z) = \frac{3}{2}\Omega_m \left(\frac{H_0}{c}\right)^2 (1+z)\,r(z) \int_{z_i^{min}}^{z_i^{max}} dz_s n_i(z_s) \frac{r(z_s) - r(z)}{r(z_s)}. \tag{2.14}$$

Galaxy clustering

The second probe analysed, the galaxy clustering, consists in the searching for close galaxies, accurately measuring their redshift and distances. This type of probe can give informations about the expansion of the Universe and about its components properties, as for examples the neutrino masses, through the precise measurement, at a redshift accuracy of $\sigma_z/(1+z) \leq 0.001$ [34], of the Baryon Acoustic Oscillations (BAO) and about the statistical properties of the galaxy field such as the galaxy correlation function and the galaxy power spectrum.

BAO are a wiggle pattern in the clustering of galaxies and were generated during the era preceding the recombination, in the inhomogeneous photon-baryon fluid: the overdense area attracted matter by gravity, creating an overpressure which travelled in the plasma thanks to the interaction between photons and electrons and between electrons and baryons. Baryons, as a consequence, kept moving away from the centre of the denser region, creating a spherical wave of matter. Dark matter instead, only weakly interacting, remained in the centre of the inhomogeneities. These waves propagated in the hot plasma until the time of recombination, when photons dissociated from matter and atoms in the Universe became neutral as previously showed. As a consequence, the pressure which kept the waves propagates stopped and leaved shells of baryonic matter at a fixed distance from the center of each inhomogeneity, the sound horizon. These shells continued attracting matter by gravitational effect, so it is expected to find a greater number of galaxies at this distance. The value of this radius measured by Planck is $r_* = 144.9 \pm 0.4\,\mathrm{Mpc}$ [9] and it is a sort of standard ruler measurably at different redshifts, making possible to study the property of the Universe during its expansion, like its geometry, and the effects of dark matter.

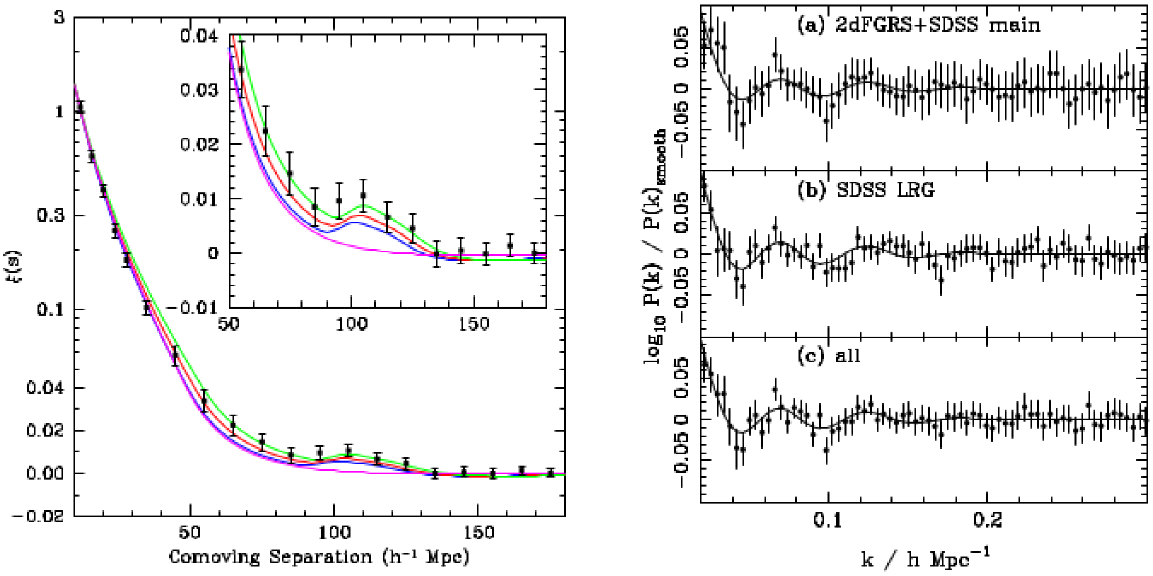

(a)

(b)

Figure 2.4: (a) Large-scale redshift-space correlation function of SDSS Luminous Red Galaxies (LRG), in which the BAO peak at $\sim 105\,h^{-1}\,\mathrm{Mpc}$ has been clearly detected. [39]. (b) Examples of BAO in power spectra calculated from different SDSS samples and assuming a flat Λ cosmology with $\Omega_m = 0.25$ [40].

One method of extracting cosmological information from the clustering of galaxies is through the two-point correlation function $\xi\left(r\right)$ which quantifies the excess (or deficiency) of clustering on a given scale relative to a uniform distribution with the same mean density. This is shown for example in Fig. 2.4a, where the evident peak due to the BAO measured by the Sloan Digital Sky Survey is compared with other model predictions with different Ω_m. This peak represents an excess of clustering at a given scale, that will correspond to a series of oscillations in the observed matter power spectrum $P\left(k\right)$, which definition has already been introduced in Sec. 1.5. These oscillations are usually pointed out calculating the ratio between the sample and a reference smooth model. The relation between the two-point correlation function and the matter power spectrum is given by

$$P\left(k\right)=\int_{\infty}^{\infty}\xi\left(r\right)\exp\left(-ikr\right)r^2dr, \tag{2.15}$$

so for example a peak described by a δ function at a characteristic scale r_* in $\xi\left(r\right)$ will correspond to oscillations in the matter power spectrum $P\left(k\right)\propto e^{-ikr_*}$. A precise measurement of amplitude and shape at various redshift of the $P\left(k\right)$ therefore permits to know the evolution of density fluctuations and as a consequence to discriminate among the various cosmological models and to compute the composition of the Universe at the various epochs. The observed matter power spectrum, however, will be influenced by the characteristic of the detector and by the expected number of observed galaxies. The estimator for the true density contrast [41]

$$\left\langle\left|\widehat{\delta}\left(\mathbf{k}\right)\right|^2\right\rangle=\frac{\widetilde{P}\left(\mathbf{k}\right)}{V}+\left\langle S\right\rangle \tag{2.16}$$

will thus include the power spectrum convolved with the survey window function $W\left(\mathbf{k}\right)$

$$\widetilde{P}\left(\mathbf{k}\right)\equiv\frac{V}{\left(2\pi\right)^3}\int d^3\mathbf{k}'P\left(k'\right)\left|W\left(\mathbf{k}-\mathbf{k}'\right)\right|^2 \tag{2.17}$$

and a shot noise $\left\langle S\right\rangle$ arising from the sampling of a finite number of galaxies.

The choice of an observation from the space instead than from the ground for this type of observable has been done because the latter one is limited by the presence of the atmosphere, that blurs the galaxy images. Although it can be possible to take in account this effect, the spatial and time variation of the atmosphere conditions does not permit to obtain a sufficient small systematic error to compute the weak lensing effect. Observing from the space makes also possible to measure with no gaps the wavelength range between 1 and 2 microns, necessary for the galaxy clustering probe and otherwise partially obscured from earth. In the next section the experiment architecture is described more in detail, showing the characteristics of the detectors which makes possible to obtain the desired precision of measurements.

2.2 Mission architecture

The Euclid experiment spacecraft consists of two modules: the Service Module and the Payload Module.

The *Service Module* (SVM) includes the subsystems needed to operate the payload, such as telemetry, power, thermal control, and attitude and orbit control (AOCS). It also includes instruments for telecommanding and communications, that will be carried out daily for a period of 4 hours. The data collected will be a large amount so, to transfer them from the internal memory of 2.6 Tbit, X and K band communications will be used, with a K band science data rate of $\sim$ 55 Mbit/s. In the SVM it is also located the instrument warm electronics, where the stable ambient temperature needed for precise measurements is granted by the sunshield previously introduced, also equipped with solar panels to provide energy for the spacecraft.

The *Payload Module* (PLM) will carry the Korsch telescope and the two instruments: the visible imager (VIS) and the near-infrared spectro-photometer (NISP). The external cylindrical baffle will protect the optical surfaces and the instruments from stray light and will provide a cold stable environment, at a temperature of $\sim$ 150 K or lower.
The Korsch telescope has been chosen to collect high quality images, reducing to the minimum the optical aberrations, such as spherical aberration, coma (chromatic aberration) and astigmatism, and is composed by three anastigmat mirrors, with the primary one (M1) of a 1.2-m-diameter and the secondary one (M2) of 0.35 m. The position of the secondary mirror is adjustable, to allow the correction of possible alignment errors after the launch. The telescope simultaneously directs the light to the two instruments via a dichroic filter in the exit pupil, directing the reflected light to the VIS and the transmitted one to the NISP as shown in Fig. 2.5, such that the instruments can both cover a common field-of-view of $\sim 0.54\,\mathrm{deg}^2$ and benefit from the similar exposure times.

The Euclid field of view will thus be of about $0.54\,\mathrm{deg}^2$ (approximately the size of the moon seen from the Earth) and, to cover the $15\,000\,\mathrm{deg}^2$ of the extragalactic sky required for measurements precision in the 6 years lifetime of the mission, Euclid will observe on a daily basis strips of about 15-20 degrees: these are observations of adjacent sky fields along a great circle of (roughly) constant ecliptic longitude. The covered surface will depend on the geometry of the instruments field of view and on the integration time per field; for example, with a field of 0.5 degree wide and an exposure time per field of 4000 s, the daily coverage would be a strip of about 18 degrees.

With these characteristics the wide survey will observe about 1.5 billion galaxies up to redshift $z \sim 2$, so that the late-time cosmic acceleration period is completely covered. Obtaining spectra and redshifts of about 50 million galaxies on a redshift interval of $0.7 < z < 2.1$, Euclid will also map the three dimensional galaxy distribution of the Universe.
In the next sections both the VIS and the NISP instruments will be examined, then it will be presented the in-flight calibration strategy for the two detectors.

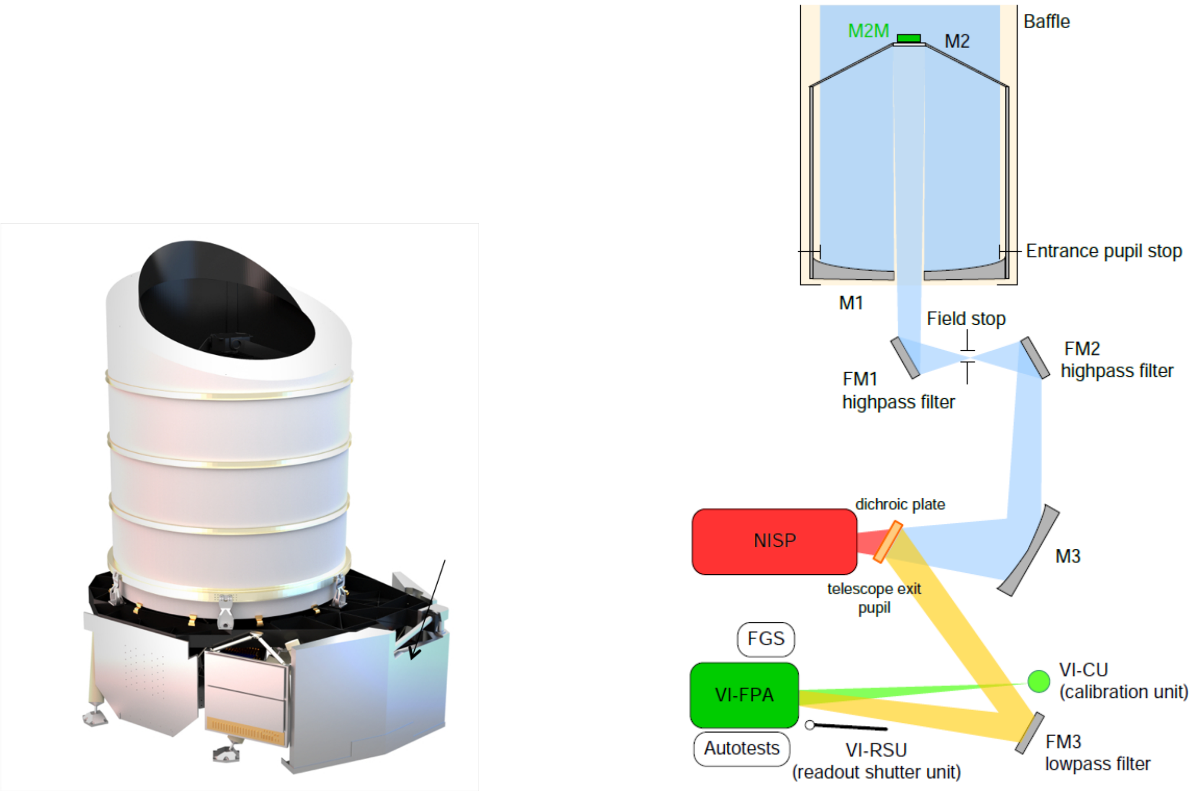

Figure 2.5: Representation of the payload module and scheme of its internal structure [34].

2.2.1 VIS

The VIS instrument provides high-quality images for the weak lensing probe. It operates in the 550 nm $< \lambda <$ 900 nm wavelength range (R+I+Z visible band) and the high resolution is needed to measure the shape of the observed galaxies. Combining measurements with the ones from the NISP and from the ground, it is not necessary for VIS to provide multicolour information within the optical band [42, 43]. The appearance of galaxies in the ultraviolet is in fact more clumpy and the expansion of the Universe shifts these wavelengths in the visible blue band, making shear measurements suffer. VIS implements therefore only a broad red band. The whole instrument is composed of several subsystems, positioned in the payload or service module as shown in Fig. 2.6.

- The incident light from the dichroic filter is directed on the *Focal Plane Array* (VI-FPA), a 6×6 grid of CCDs (Charge Coupled Devices). Each CCD273-84 detector, one of which is pictured in Fig. 2.7, has an area of 4096×4132 pixels, which together with the telescope precision provides an image scale of 0.101 arcsec per

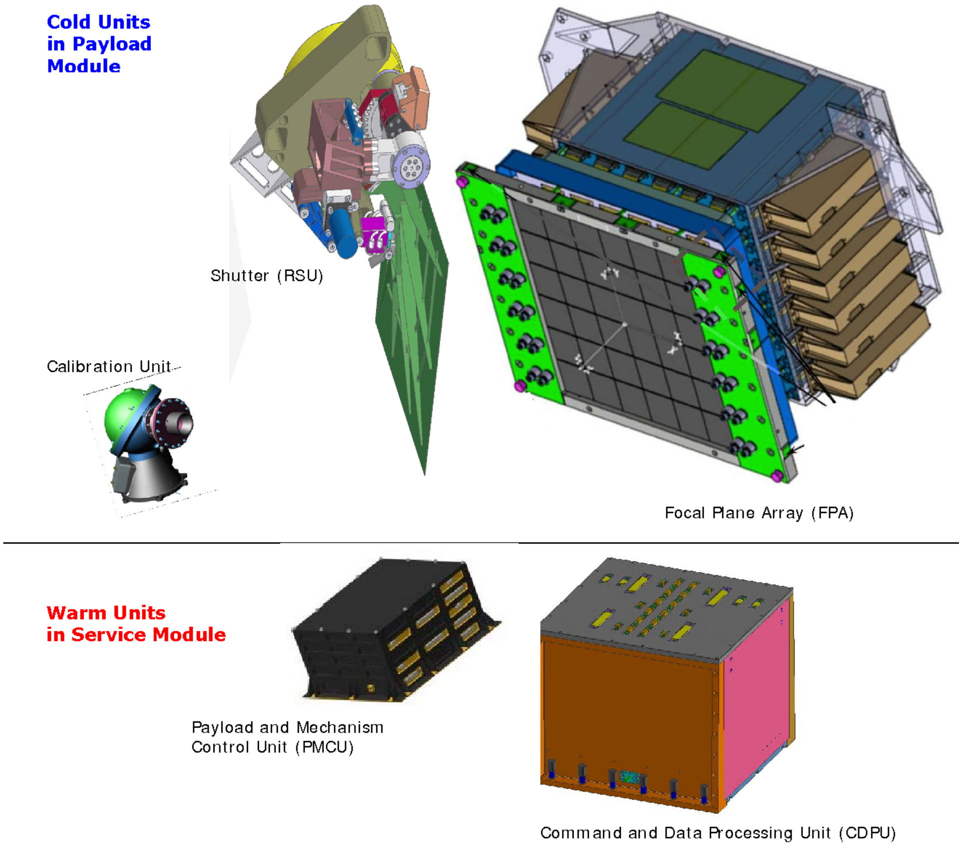

Figure 2.6: The units comprising VIS [44].

12 μm pixel with a field of view of $0.787\,\text{deg} \times 0.709\,\text{deg}$. The CCDs are held in a Silicon Carbide (SiC) structure, with minimum thermo-elastic responsiveness to keep a precise positioning with respect to the focal plane, so that the whole FPA has dimensions of ~ 0.45m on each side. Since CCDs have shown optimal charge transfer efficiency at a temperature of $150 - 155$ K, the whole array is positioned in the cold payload module environment to reduce the thermal noise.

- A *Shutter Unit* (VI-SU) in front of the FPA has the task of blocking the light while the detectors are not making exposures or being read out, avoiding stray light during data processing. The shutter mechanism is momentum-compensated (linear and angular), to minimise disturbances to both the spacecraft and the NISP instrument.

- The *Calibration Unit* (VI-CU) is an integral sphere equipped with LEDs, providing light at different wavelengths within the VIS passband to the entire FPA: in this way, it is possible to measure the pixel-pixel variation in the CCDs, used for the

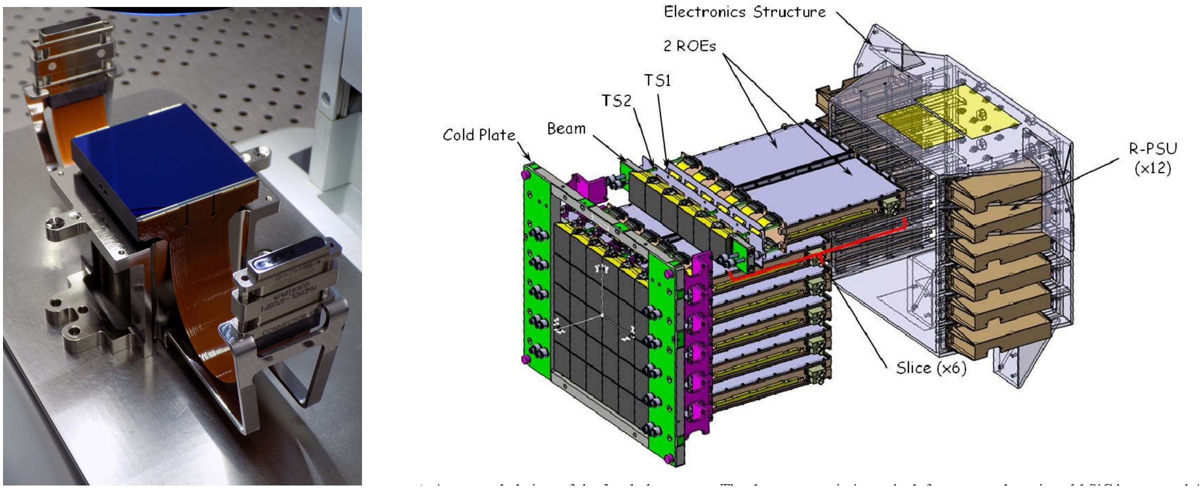

Figure 2.7: One of the VIS CCDs and extended scheme of the FPA.

flat-field calibration. A shutter is not present in this case, because the exposures for calibration are short and the sky signal does not much affect the flat field signal.

- The *Command and Data Processing Unit* (VI-CDPU), positioned in the service module, is responsible for the:
    - telemetry and telecommand exchange;
    - instrument commanding;
    - instrument monitoring and control;
    - synchronisation and sequencing of all the instrument activities;
    - data acquisition from CCDs, pre-processing and formatting them for transfer to the spacecraft bulk memory (MMU).
- The *Power and Mechanism Control Unit* (VI-PMCU) provides power and controls the activation of the calibration unit and of the shutter.

VIS observations are carried out without windowing the focal plane with an exposure time of 565 s, then data from CCDs are digitalised, buffered and compressed. This process is repeated four times for each field with displacements of 100 arcsec between the exposures and an additional lateral 50 arcsec for the fourth one. This type of observation strategy permits to cover gaps in the detector matrix, allows some recovery of the spatial resolution, minimises radiation damage impact on the data and allows cosmic rays to be identified. The coadded image obtained from this ditherings has at least three exposures for more than 95% of the pixels and four exposures for about 50% pixels, improving the signal-to-noise ratio [34]. With these measurements VIS can reach to deeper than a magnitude $m_{AB} = 24.5$ for sources with an extent ~ 0.3 arcsec.

2.2.2 NISP

The Euclid's Near-Infrared Spectrometer and Photometer (NISP) instrument has been designed to perform slitless spectroscopy and imaging photometry in the three near-infrared wavelength bands (Y, J and H) and its characteristics have been optimized to reach the imaging quality and depth requirements for weak lensing and galaxy clustering previously showed in Sec. 2.1.1. Its main goal is thus to measure both the photometric redshift of the weak lensing galaxies and the spectroscopic redshift for the galaxy clustering using respectively two observing modes: the first (photometric mode NISP-P) through three broad band filters, together with ground-based multiband measurements, and the second (spectroscopic mode NISP-S) dispersing the light through a *grism.* The grism is a transmission grating ruled on the hypotenuse of a prism and thus at a particular wavelength the diffraction of the grating is compensated by the prism deviation, providing a linear dispersion.

The NISP instrument operates at a temperature lower than 140 K except for the detectors, cooled to ~ 120 K, and for the warm electronics, located in the service module at a temperature higher than 240 K. The units which compose the NISP are organized in three main assemblies:

- The *Opto-Mechanical Assembly* (NI-OMA) holds the optical elements at a cryogenic temperature and its optics is schematised in Fig. 2.8. It is composed of:
    - the *Mechanical Support Structure* (NI-SA), which also supports the detection system;
    - the *Thermal Control* (NI-TC);
    - the *Corrector Lens Assembly* (NI-CoLA), which corrects residual abberation after the telescope pupil;
    - the *Filter Wheel Assembly* (FWA), which houses the three broad band filters Y, J and H, respectively of wavelength ranges Y $= [900 - 1192]$ nm, J $= [1192 - 1544]$ nm and H $= [1544 - 2000]$ nm, and switches between them. It is configured with five slots in order to integrate in addition to the filters an open slot and a closed one;
    - the *Grism Wheel Assembly* (GWA), with four different grisms and a counterweight. The grisms differ from each other for the passband coatings and for their orientation: one, used for calibration and for the deep survey, transmits between $1.1\,\mu$m and $1.45\,\mu$m (Blue) and has a 0 deg orientation, while the other three are transparent between $1.45\,\mu$m and $2\,\mu$m (Red) and have orientations at 0 deg, 90 deg and 180 deg in order to reduce confusion in spectra;
    - the *Camera Lens Assembly* (NI-CaLA), which images the field of view onto the focal plane;

  - the NISP *Calibration Unit* (NI-CU), mounted near the rim of the last lens (part of CaLA), which generates flat fields for the calibration and measurements of the detector linearity. It illuminates the focal plane at five different infrared wavelengths using 2×5 LEDs pointing onto a reflector.

  To compensate the thermo-mechanical effects, adaptation rings are glued to the various optical elements. These rings introduce quasi zero forces and torques, preserving the shape and position of the elements.

- The *Detector System Assembly* (NI-DS), composed of:
  - the *Sensor Chip System* (NI-SCS), a grid of 4×4 H2RG detectors, their cryoflex cables (10 cm) and their ASICs (Application Specific Integrated Circuits) SIDECAR (System Image, Digitizing, Enhancing, Controlling And Retrieving) electronics which manage all operations and output digitalizations;
  - the *Focal Plane Assembly* (NI-FPA), that is the mechanical part and is made up of a SiC panel screwed on the structure of the NI-OMA with three bipods anchoring the Support Structure for the Sidecars (SSS) and a Cold Plate (CSS) that supports the detectors with a protection baffle fixed on it.

  The detectors are cooled to an operating temperature of $\sim 95\,\mathrm{K}$, while the ASICs SIDECAR have a higher temperature of $\sim 139\,\mathrm{K}$ due to their active dissipation. The whole mechanical structure has a temperature around 132 K.

- The *Warm Electronic Assembly* (NI-WE), composed of:
  - two *instrument Data Processing Unit* (NI-DPU) both with eight *Detector Control Unit* (NI-DCU), providing clock and power to a sensor, and its ASIC SIDECAR preprocessing the data (such as images coadding). Each NI-DPU includes a CPU that completes the onboard data processing and then compresses, formats and sends the scientific data to the central spacecraft memory;
  - one Instrumental Control Unit (NI-ICU) which provides a general power supply and commands the functions of the NI-OMA and of the NI-CU. It is interfaced with the spacecraft via a 1553 bus.

The HgCdTe infrared sensors in the focal plane, named H2RG, (see Fig. 2.9) are composed of a matrix of 2048×2048 pixels of 18 microns in size, with a wavelength cut-off at $2.3\,\mu$m. Each pixel scale is set to 0.30 ± 0.03 arcsec to reduce crowding, so the total field of view is about $0.5\,\mathrm{deg}^2$.

In the photometer mode NISP will thus operate from 920 nm to 2000 nm (Y, J, H bands) range, with a limit magnitude for $\mathrm{Y_{AB}}$, $\mathrm{J_{AB}}$ and $\mathrm{H_{AB}}$ bands of 24 mag (5σ) and high image quality. These characteristics allows the NISP to measure redshifts of tens of millions of galaxies, basing the observation on the detection of emission lines (mainly the H-α) in the near infrared at over 3.5σ of detection for a $2.10^{-16}\,\mathrm{erg/cm^2/s/pixel}$ line flux [45].

In the spectrometer mode, the light from the target is dispersed in the range from 920 nm to 1850 nm. The grisms provide a flat resolution over their specified range, with a mean spectral resolution

2.2.3 In-flight calibrations

In Fig. 2.10 it is shown the timeline for a field observation of both VIS and NISP: the VIS exposure takes place during the spectroscopic exposure of NISP because they have the same duration, but the time during the NISP photometric exposures cannot be used for science observations, because of pointing disturbances caused by the NISP filter wheel. This time can instead be used for VIS calibrations such as bias fields and dark exposures. The last ones can be of three types: in the first one the dark current in the detector and hot pixels are measured, while in the second and the third one charge is injected respectively in a few lines or over the whole region of the CCD. The last two types of calibrations are used to measure the radiation damage to the detector.

Flat field calibrations are made, instead, at the end of the four exposures composing the sequences (and just before the spacecraft slew), since they need the use of the Calibration Unit and might interfere with NISP measurements. The flux needed for this calibration is provided in only 10 seconds, a time short enough to not interfere with the standard measurement operations.

Linearity calibrations are more complex and are held during all the four exposures with different timings, while the shutter opens and closes. In this way it is possible to estimate the flux in the image and to determine linearity.

For the NISP instrument the dark measurement is performed at the end of the science sequence, when during the slew both the VIS shutter is closed and the NI-FWA is in close position. Most of the calibrations, especially for the NISP, will be available from the science data themselves, in particular the photometric, spectroscopic and the point spread function ones, highly representative of the instrument characteristics. For this purpose, the calibration fields will be repeatedly observed over the six years of the mission to assess the stability and accuracy of the measurements.

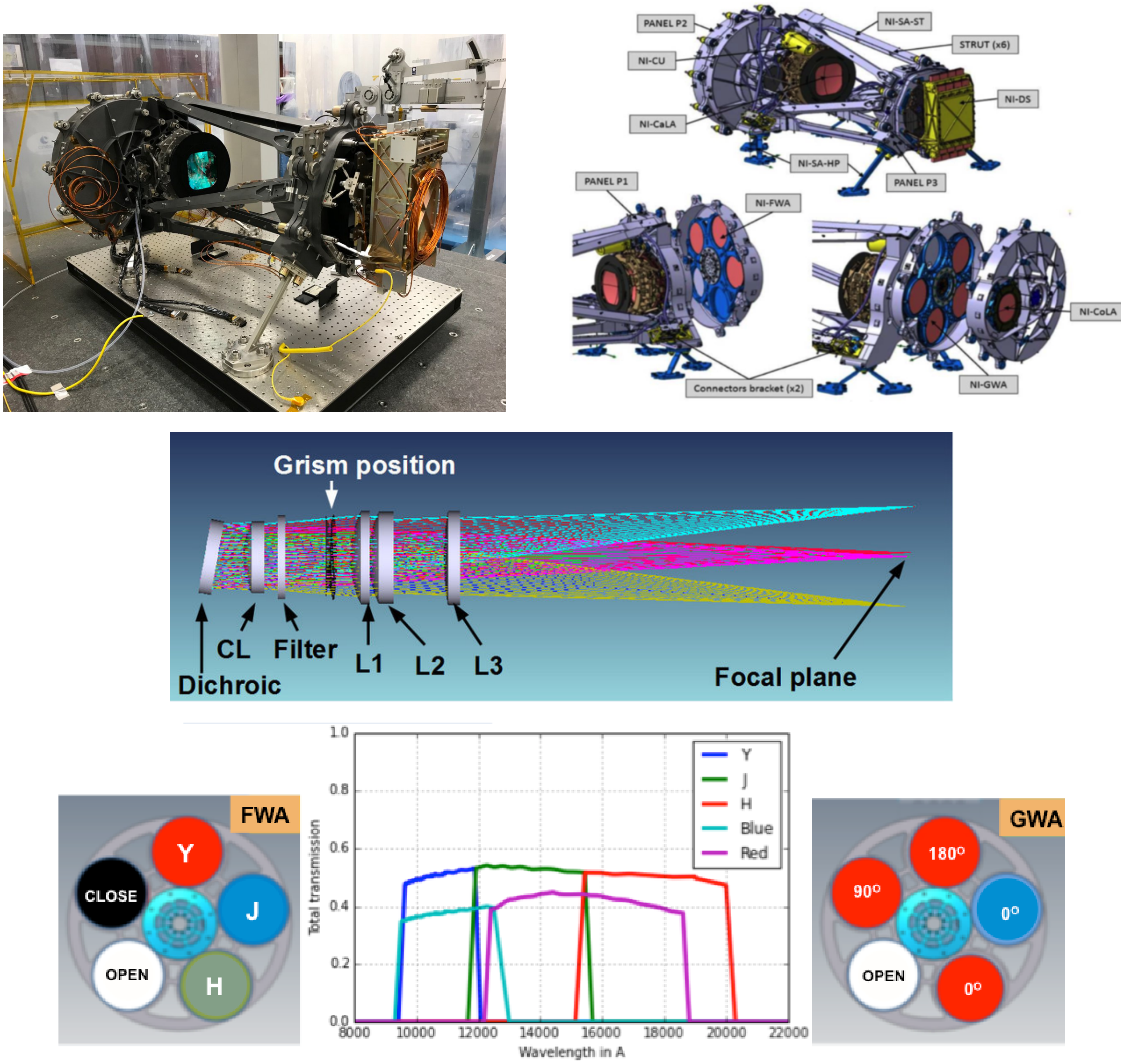

Figure 2.8: The photo shows the NISP instrument during assembly at LAM. In the top panel sketch are pictured the elements of the NISP Opto-Mechanical Assembly together with the Detector System Assembly (NI-DS). The elements are NISP Calibration Unit (NI-CU), NISP Camera Lens Assembly (NI-CaLA), NISP Structure Assembly (NI-SA), NISP Corrector Lens Assembly (NI-CoLA) and the the NISP Filter Wheel Assembly and the Grism Wheel Assembly, respectively NI-FWA and NI-GWA. The middle panel shows a sketch of the NISP optics: CL is the Corrector Lens, while L1, L2 and L3 are the Camera Lens Assembly. The dichroic is part of the telescope assembly [34]. In the bottom panels are shown the filter positions (left), grism positions (right) and the transmission curves of the Y, J and H filters and of red and blue grisms. Courtesy Euclid Consortium/NISP team.

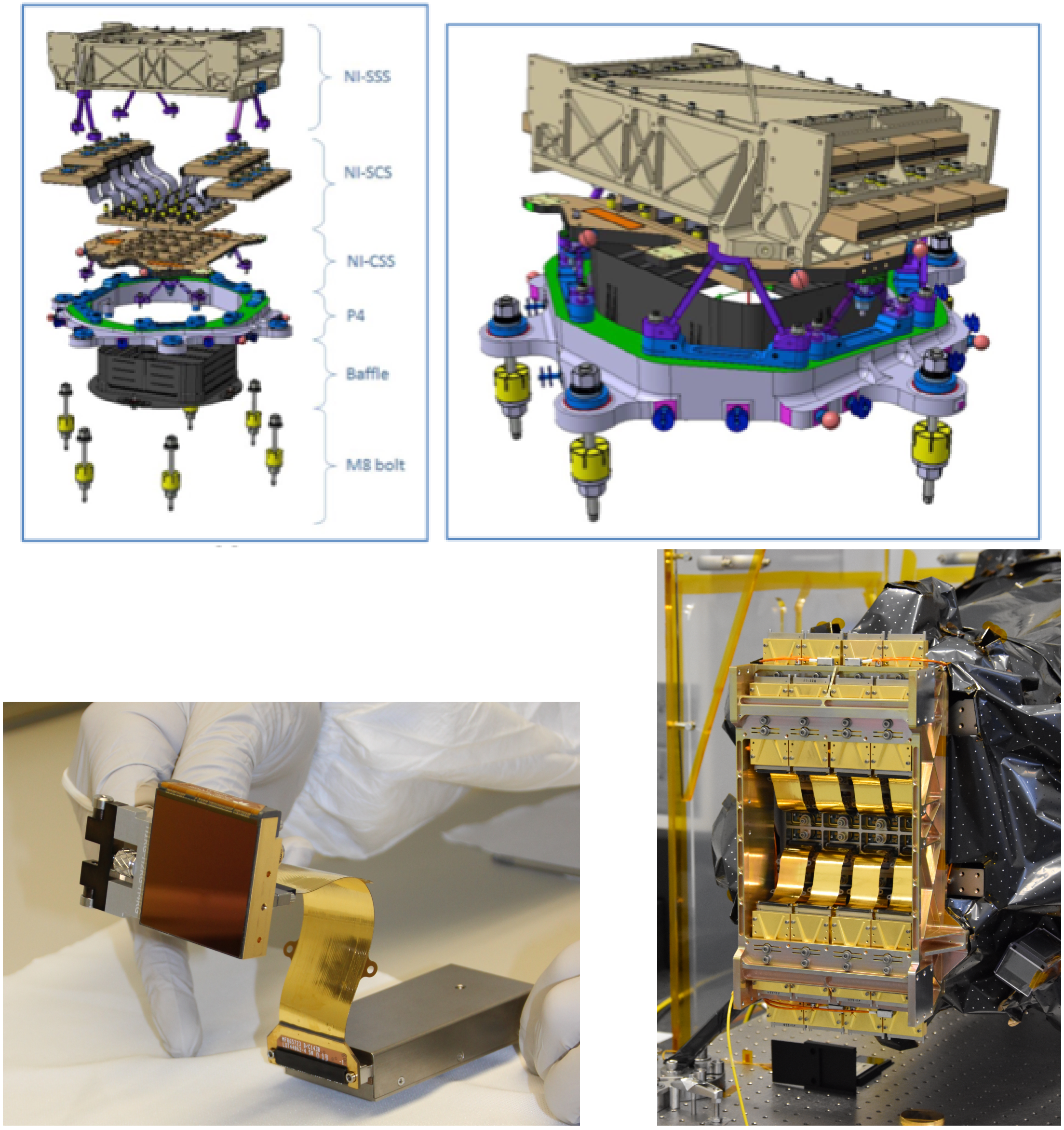

Figure 2.9: In the top panels it is shown the NISP focal plane and the elements of the NISP Detector System: NISP Sidecar Support Structure (NI-SSS), NISP Sensor Chip System (NI-SCS) and NISP Cold Support Structure (NI-CSS) for the detectors. The bottom photos show one of the H2RG infrared sensors (on the left) and the Detector System Assembly (NI-DS) (on the right). In the last one the Sensor Chip System (NI-SCS) is pointed out, with the gold coated hardware being the 16 Read Out Electronics (SCEs) integrated with the sensors (enclosed inside the black multi-layer insulation). Courtesy Euclid Consortium/NISP team.

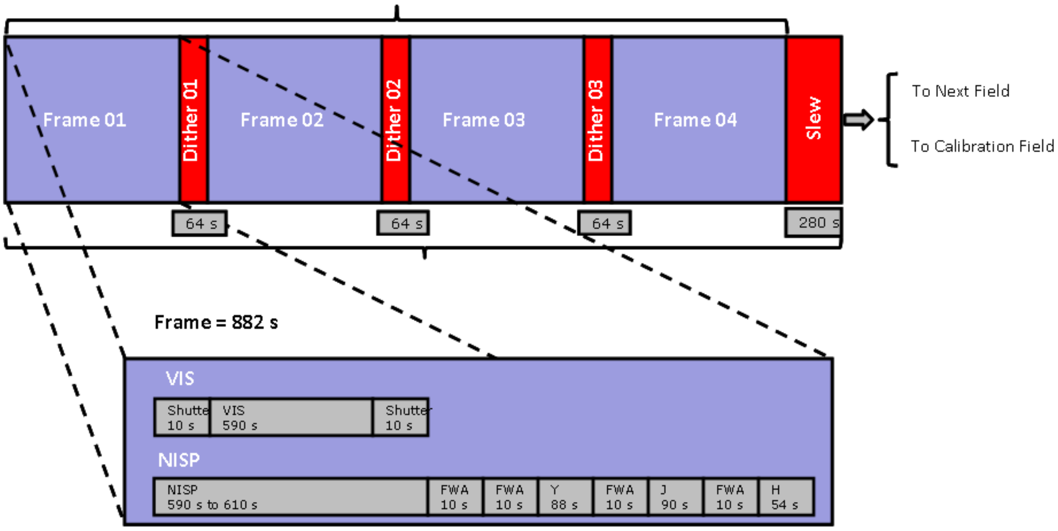

Figure 2.10: Timeline of observations [34].

Chapter 3

Statistical tools for analysis

In the first part of this chapter, the Bayesian concept of probability used for cosmological data analysis and the notation employed are presented. In the second part the codes used to compute the forecasts, CLASS and MontePython, are described.

3.1 Bayesian interference from cosmological data

The first historical approach to probability was based on its *frequentist* definition, which considers the probability of an event as [46]

> *'the number of times the event occurs over the total number of trials, in the limit of an infinite series of equiprobable repetitions.'*

This definition, however, has some limitations and various unsatisfactory aspects. First of all, the definition itself is circular, because it assumes that trials have the same probability of outcomes while explaining the concept of probability, then it is necessary that trials are repeatable, so for certain events or observables it is not possible to define their probability at all. Another problem is that this type of definition holds exactly only for an infinite number of repetitions, while an experiment or an observation gives back a finite number of them. A consequence of this approach is that also the definition of the 'randomness' concept is ill-posed and circular, because it is related to a certain probability of an event already supposed to be random.

To avoid these limitations and paradoxes, in late 1700s was born the *Bayesian* approach. It is completely different with respect to the frequentist one, because it affirms that

> *'probability is a measure of the degree of belief about a proposition.'*

For this reason this approach is called *subjective*, as deals with hypotheses or propositions that are either true or false and expresses our logical deductions in presence of incomplete informations about the system. In this way, it is possible to apply this definition both to repeatable and unrepeatable events, simultaneously solving the circularity problem. The Bayesian interpretation of probability can also provide a more natural treatment of systematic uncertainties, often deriving from partially known effects, of nuisance parameters and of physically meaningless results of the inference; in addition it solves the problem of randomness, seeing it as a consequence of the lack of information about the exact condition of the system. Below it will be examined the details of this type of approach, used in this thesis to derive all the constraints on cosmological quantities.

3.1.1 Bayes' theorem

Given the definition of conditional probability of A given B

$$P\left(A|B\right) = \frac{P\left(A,B\right)}{P\left(B\right)}, \tag{3.1}$$

where $P\left(A,B\right)$ is the joint probability of A and B and the analogous conditional probability of B given A is $P\left(B|A\right)$, since for the joint probability $P\left(A,B\right) = P\left(B,A\right)$ it is possible to derive the *Bayes' theorem*

$$P\left(A|B\right) = \frac{P\left(B|A\right)}{P\left(B\right)}. \tag{3.2}$$

This theorem is fundamental analysing cosmological data since, with respect to high energy physics that deals with a great number of events, cosmological observations can only be compared to existing models. Replacing in Eq. 3.2 the hypothesis H for A and the observed data d for B, it is obtained the equation

$$P\left(H|d\right) = \frac{P\left(d|H\right)P\left(H\right)}{P\left(d\right)}, \tag{3.3}$$

which summarise our statistical approach to cosmological observations. On the left-hand side of the equation $P\left(H|d\right)$ is the *posterior probability* of the hypothesis, i.e. the probability of the hypothesis (our model) taking the observed data d into account. On the right-hand side $\pi\left(H\right) \equiv P\left(H\right)$ is the *prior probability* for the hypothesis, which is obtained from all external informations available before the experiment. The term $P\left(d|H\right)$ is the sampling distribution of the data assuming the hypothesis is true, also called for fixed data (the observed ones) the *likelihood function* $\mathcal{L}\left(d|H\right) \equiv P\left(d|H\right)$. Finally, the normalisation constant in the denominator is the *marginal likelihood*, often called *Bayesian evidence* and given by the sum over all possible models or hypothesis H,

$$P\left(d\right) \equiv \sum_{H}\left[P\left(d|H\right)P\left(H\right)\right]. \tag{3.4}$$

Below will be given a wider definition of prior and likelihood functions, then in the next sections will be treated more in detail the Bayesian techniques for parameter inference and model comparison.

Prior functions The definition of the prior function representing the knowledge about an hypothesis or a physical quantity is the first step of any Bayesian inference. Taking as example a parameter extraction, if the assumed theoretical model $\mathcal{M}$ comes with a set of N free parameters θ_i, it will also comprehend N probability distributions $\pi(\theta_i)$ representing the present knowledge on each parameter *a priori*, before using the data. The theory does not explain how this prior functions should be selected, but this is not a problem: for physical quantities θ_i, as long as the prior $\pi(\theta_i)$ has a support that is non-zero in regions where the value of the likelihood is large, repeated applications of the Bayes' theorem will lead to a posterior probability density function (pdf) that converges to a common inference on the parameter [46]. Only if data are not strong enough to override the prior, the convergence will not be reached and this will still make possible to conclude that the data are not informative enough to constrain the value of the physical quantity analysed. Some examples of classical prior functions can be the simple flat distribution over the interval in which the parameter is meaningful, also called top-hat distribution, or a Gaussian function with the mean value and standard deviation taken from an external data set.

For model comparison and selection, however, the impact of the prior is much stronger with respect to the case of parameter extraction. An example is about the choice of the *ignorance priors*, better referred as *noninformative priors*, reflecting our lack of knowledge. This type of pdfs have to be chosen carefully: a top-hat prior on a parameter θ can be uninformative, but the prior on the function $\psi(\theta)$ of the parameter θ can be strongly informative, as the two priors are related by the function

$$\pi(\psi) = \pi(\theta) \left| \frac{d\theta}{d\psi} \right| . \tag{3.5}$$

If the function $\psi(\theta)$ is non-linear, its derivative is a function of the parameter θ itself and this can lead to errors due to the hidden prior information, which can mimic the constraining power on the data.

Another type of prior functions can be *reference priors*. They are chosen in order to represent the least informative state of knowledge about a model but, contrary to the uninformative ones, they take in account the characteristics of what the experiment is expected to provide maximising the divergence between the posterior and prior function, so that the data could have the maximum effect on the posterior estimates.

The last characteristic of prior functions is that they must be *proper*, i.e. normalizable to unity probability content, in order to be well-defined probability distributions.

Likelihood functions The likelihood function $\mathcal{L}(d|\mathcal{M})$ has been defined as the probability of observing the obtained data d, given an hypothesis or a theoretical model $\mathcal{M}$ with its parameters θ_i. This function is usually constructed reflecting the way the data have been obtained and is strongly dependent on the characteristics of the experiment.

The likelihood function can be, for example, a normal distribution if the measurement presents a Gaussian noise, or it can be a Poisson distribution for counts of a γ-ray detector. It is possible that the likelihood function contains some nuisance parameters together with the ones of physical interests: in this case, one can simply consider their prior function and deal with them when calculating the posterior function.

Likelihood functions are fundamental for Bayesian model comparison, as will be shown in Sec. 3.1.3.

3.1.2 Parameter inference and marginalisation techniques

The Bayesian approach to parameter inference aims to obtain the posterior function for a parameter θ, given a model $\mathcal{M}$ and taking into account the observed data d. After the specification of the prior function $\pi(\theta|\mathcal{M})$ and the construction of the likelihood $\mathcal{L}(d|\theta,\mathcal{M})$, using the Bayes' theorem it is possible to compute the posterior pdf for the parameter θ

$$P(\theta|d,\mathcal{M}) = \frac{\mathcal{L}(d|\theta,\mathcal{M})\,\pi(\theta|\mathcal{M})}{P(d|\mathcal{M})}. \tag{3.6}$$

The constant $P(d|\mathcal{M})$ normalises the posterior pdf to one and is called *Bayesian evidence*. This term, although negligible for parameter inference, will instead be fundamental for model comparison (see Sec. 3.1.3).

Nuisance parameters related to insufficiently constrained aspects of the physics of the observed object, or uncertainties in the measuring process might be present in the likelihood, for example if the variance of the Gaussian noise is unknown, if there is an uncertainty on the background rate without a source, or other ones. In this case the Bayesian approach uses the whole likelihood to calculate the joint posterior function for the parameters of interest ϕ and the nuisance parameters ψ, referred together as $\theta = (\phi,\psi)$. The posterior pdf is obtained through the Bayes' theorem as in Eq. 3.6, then the result is integrated over the nuisance parameters, obtaining the posterior probability density function only for the parameters of interest. This process is called *marginalization* technique and allows to obtain the marginal posterior on the parameters ϕ

$$P(\phi|d,\mathcal{M}) = \int \frac{\mathcal{L}(\phi,\psi)\,\pi(\phi,\psi|\mathcal{M})}{P(d|\mathcal{M})} d\psi. \tag{3.7}$$

Bayesian intervals Obtaining the posterior function is the first step of Bayesian parameter inference. This function can be used to communicate the inference on the parameters of interest ϕ in many ways:

- using the mean, mode or median of the distribution itself, its standard deviation and the correlation matrix among the components;
- plotting some one or two dimensional subsets of the parameters ϕ;

- determining credible intervals.

A *confidence interval* at a probability level n is defined as the interval $[\phi_l, \phi_u]$, for which the integral of the posterior function $P(\phi|d, \mathcal{M})$ in ϕ is equal to n,

$$\int_{\phi_l}^{\phi_u} P(\phi|d, \mathcal{M})\, d\phi = n. \tag{3.8}$$

Using this equation, it is possible to obtain a *central interval* if the two values ϕ_l and ϕ_u have been calculated by having probabilities of $(1-n)/2$ below the interval and $(1-n)/2$ above it. *Upper limits* ϕ_{UL} and *lower limits* ϕ_{LL} values for *one-sided intervals* are obtained on the other hand setting the limits of integration respectively from zero (or from the minimum value of the parameter) to ϕ_{UL} or from ϕ_{LL} to infinity.

The Bayesian interpretation of the meaning of a confidence interval is very different from the frequentist one. Frequentists build intervals at a confidence level CL $= n$ computing the values for which each interval has a probability of n to cover the true value of the parameter, obtaining thus a *coverage probability.* The probability in this case only refers to the range ϕ_l to ϕ_u, because the parameter ϕ is unknown but has a true value and can not be the subject of probability statements. Bayesians, on the other hand, calculate the values ϕ_l and ϕ_u from the observed data and the parameter value has the n% probability to fall in the obtained *credibility interval.* The real value of ϕ is thus considered as a variable computing the integral value.

3.1.3 Model comparison and Bayesian evidence

The Bayesian model comparison offers a very simple and efficient way to select which model has to be preferred, but in contrast with the frequentist goodness-of-fit tests, which consider other possible outcomes but focuses only on one hypothesis, it is necessary that the examined model is compared with another one. In this context, models can be considered as a set of parameters θ with their prior distribution $\pi(\theta|\mathcal{M})$. For model selection it is used the *Bayesian evidence*, previously introduced in Eq. 3.4 and here explicitly rewritten for model comparison in a continuous parameter space $\Omega_{\mathcal{M}}$ as

$$P(d|\mathcal{M}) \equiv \int_{\Omega_{\mathcal{M}}} \mathcal{L}(d|\theta, \mathcal{M})\, \pi(\theta|\mathcal{M})\, d\theta. \tag{3.9}$$

In this case the integral is calculated over the whole parameter space because, for the purpose of model comparison, any parameters are considered as nuisance parameters, even if they are physically meaningful. The prior function choice, as anticipated in Sec. 3.1.1, has for this reason a stronger effect in model comparison with respect to parameter inference. This is due to the fact that, while constraining parameters the prior function could be easily overwritten by the posterior, in this case there could be parameters which occur in one hypothesis but not in the other ones, or another parameter which has a wider range for a model with respect to the others. This will affect the normalisation parameter, favouring one model over another one.

Bayes' factor To evaluate the model's performance in the light of the observed data, it is used the Bayes' theorem with $P(\mathcal{M})$ the prior probability assigned to the model itself, obtaining

$$P(\mathcal{M}|d) \propto P(\mathcal{M})\, P(d|\mathcal{M})\,. \tag{3.10}$$

The model prior probabilities are generally taken to be non-committal and equal to $1/N_m$, with N_m the number of different models considered. The comparison between the validity of two models $\mathcal{M}_0$ and $\mathcal{M}_1$ goes thus through the evaluation of the ratio of their probabilities given the data, called *posterior odds*,

$$\frac{P(\mathcal{M}_0|d)}{P(\mathcal{M}_1|d)} = B_{01}\frac{P(\mathcal{M}_0)}{P(\mathcal{M}_1)} \tag{3.11}$$

where the *Bayes' factor* is the ratio of the models' evidences previously calculated in Eq. 3.9

$$B_{01} \equiv \frac{P(d|\mathcal{M}_0)}{P(d|\mathcal{M}_1)}\,. \tag{3.12}$$

A small value of B_{01} will thus favour the $\mathcal{M}_1$ model, while a higher one will support $\mathcal{M}_0$.

3.2 Markov Chain Monte Carlo techniques

As seen in the previous sections, Bayesian analysis requires to compute of the value of integrals, but the integrated functions such as the likelihood or the posterior pdf are often complex and the problem is not analytically tractable. It has been necessary, for this reason, to use numerical techniques in order to evaluate the distributions: the most commonly used and the one adopted in this thesis is the *Markov Chain Monte Carlo* technique.

The *Monte Carlo* (MC) techniques are numerical algorithms which generate random numbers and permit to compute integrals or to simulate physics processes. For our purposes the technique used to compute integrals consists on repeated random sampling of the function or of the integral that is been examined, followed by a statistical analysis of the results. The error on the result typically decreases as $1/\sqrt{N}$, where N is the number of points in the sample.

The sequence of random variables $\left\{X^{(0)}, X^{(1)}, \ldots, X^{(M-1)}\right\}$ in the parameter space, called 'chain', is generated such as the probability of the $(t+1)$-th element only depends on the value of the t-th one and the point density is proportional to the distribution that has to be studied. The random point generation is made using various pseudo random number generators. They are mathematical sequences with statistical properties similar to real casual number sequences, preferred with respect to the physical generated ones because they are much more fast. The most popular algorithms include the Metropolis-Hastings algorithm, Gibbs sampling, Hamiltonian Monte Carlo and importance sampling. In the MontePython code it is possible to choose between some types of algorithms, presented in Sec. 3.3.2.

Once this *Markov chain* has been constructed, the value of an integral can be computed using a Monte Carlo estimator, doing the sum over all the elements of the chain. The expectation value for a generic function $f(\theta)$, where the parameter θ has a pdf $P(\theta|d)$, becomes then

$$\langle f(\theta)\rangle = \frac{1}{b-a}\int_a^b P(\theta|d)\, f(\theta)\, d\theta \approx \frac{1}{M}\sum_{t=0}^{M-1} f\left(\theta^{(t)}\right) \tag{3.13}$$

where $\theta^{(t)}$ are the M the random values of the chain in the (a, b) interval. The MC estimator converges to the exact value of the integral when M goes to infinity. In this way, to obtain for example the posterior mean it is sufficient to compute

$$\langle\theta\rangle = \int P(\theta|d)\, \theta d\theta \approx \frac{1}{M}\sum_{t=0}^{M-1} \theta^{(t)} \tag{3.14}$$

Generalising to an n-dimensional parameter space, it is possible to calculate the 1-dimensional marginal probability for the j-th element of $\theta = (\theta_1, \ldots, \theta_j, \ldots, \theta_n)$ simply taking the elements of the Markov chains, which density reflects the value of the full posterior pdf, and binning the density of only the j-th element, ignoring the other coordinates value of θ. An important issue working with Markov Chain Monte Carlo (MCMC) methods is to ensure that the parameter space has been explored in the correct way, covering all its relevant parts in order to do not avoid secondary peaks or wells of the posterior pdf.

3.3 CLASS and MontePython codes

CLASS and MontePython are the two software codes used for the forecasts in this thesis. The CLASS code is the Boltzmann solver, while MontePython is the sampler that interfaces with CLASS in order to compute the posterior functions for the parameters of interest. In this section the main characteristics of these two software codes are described.

3.3.1 CLASS

CLASS is the acronym for Cosmic Linear Anisotropy Solving System [47, 48] and is a Boltzmann solver code. Given a cosmological model defined by the input parameters (as seen in the first chapter and in particular in Sec. 1.5.2), the code evolves the Universe background and the cosmological perturbations, returning to the user the observed CMB spectra and matter power spectrum (previously described in Sec. 1.5.1).

CLASS is written in C, without the use of external libraries. This choice has been done due to the diffusion and the greater velocity of this language, better with respect to C++ or other ones. The code is structured in modules, each one dealing with a different step of the process needed to compute the observed power spectra from an initial background with some perturbations.

The first module sets all input and precision parameters to default values, and then eventually replace some of them with the values indicated in the input file. In this file are contained the parameters describing a certain cosmological model, as shown in Sec. 1.5.2. In the input file it is possible to enter the cosmological parameter of interest in different bases, as some basic logic implemented in the code prevents errors and repetitions, expecting only one parameter out of an array. The code for example complains if fed with more than one between $\{H_0, h, 100 \cdot \theta_s\}$. The missing input parameters are also inferred from the given ones or, if this is not possible, their value is taken from the default ones, that are in-built in the code.

The second module solves the background equations (as the Friedmann equations 1.14 and 1.15), then the third one computes the thermodynamical evolution saving values connected to the recombination and reionization processes. The fourth one solves the evolution of all perturbations, then the fifth and sixth ones compute respectively the spherical Bessel functions and transfer functions. In the end, the final modules compute the primordial and observable power spectra, with the possibility to give an estimate of the non-linear version of the observable one, or to compute lensed temperature and polarisation CMB spectra. The code eventually returns the output written on a file.

All the perturbation equations and the notation used for the synchronous and Newtonian gauges are taken from the Ma and Bertschinger paper [49], while for non-flat universes it has been used the Tram and Lesgourgues paper [50].

3.3.2 MontePython

MontePython [51, 52] is a Monte Carlo code written in Python and its purpose is to create the Markov chains needed to compute posterior functions. In order to explore the parameter space, it communicates with CLASS at every step to calculate the cosmological values characteristic for each point. MontePython does in fact not implement any cosmological or physics equation, but deals only with the statistical part of the analysis, resorting to the interface with CLASS when in need. The likelihood functions needed for the analysis are implemented outside the main code, that contains instead the exploration algorithm.

In the released version of the code are included likelihoods for different experiments, but it is also present a basic likelihood class to whom inherit the basic functions for the implementation of new likelihoods. In this thesis, it has been used the ones accounting for the sensitivity of Planck and for the Euclid galaxy clustering and cosmic shear surveys.

In the input MontePython file are contained, together with the used likelihoods names, all the cosmological parameters, with their mean values, ranges, scaling and the list of extra parameters that have to be derived or that are considered fixed. In order to work with new parameters, it is possible to add them directly to the CLASS input module, or to modify the MontePython file `data.py` that contains all internal parameters redefinition in function of the parameters known by CLASS. In order to recover derived parameters the CLASS wrapper routine, that converts CLASS C functions into Python and send the derived quantities back to MontePython, should know about them.

When starting a new MontePython run, together with the input file is given the path to the output folder and the number and size of steps (the jumping factor) of the chain. With the option `--update` it is also possible to change the default number of steps after which the covariance matrix is updated, while with `--superupdate` it is possible to set the number of steps after the update of the covariance matrix to update the jumping factor. The parameter space can in addition be explored with different algorithms, called `methods`: it is possible to choose between the Metropolis-Hastings, Nested Sampling, Cosmo Hammer, Fisher sampling and Importance Sampling methods, where the default one is the Metropolis-Hastings.

After the start of the run, the `log.param` file is created: it contains all the informations from in the input file, plus the path to fiducial files, the version of the Boltzmann code, the version and the characteristics of each data likelihood, etc. In this way it is possible to remember the details of the run end eventually restart a chain with the same parameters as the first one. If the input file is not provided to the code, this `log.param` file is in fact read and used instead, while if both are present the code will run only if the data contained are the same. It is also possible to provide a covariance matrix for the set of parameters, from which the code will get all possible information after automatically doing all the necessary matrix manipulation steps.

After the creation of the chains using the `run` mode, MontePython allows to analyse them with the `info` mode. The analysis module produces from the chains in the given directory the output files and one or two dimensional plots in PDF format, showing the posterior contours at 68% and 95% CL in the triangle plot and the shapes of the marginalised posterior and of the mean likelihood per bin in the one dimensional plots.

Chapter 4

Forecasts and data analysis

In this thesis work it has been evaluated the future sensitivity of the Euclid experiment using Bayesian inference. In this chapter will be presented at first the results obtained using the ΛCDM model, that has been established as the standard model for cosmological structure formation, as a base for forecasts. After testing the sensitivity in case of this standard ΛCDM model, the study has been extended considering three massive neutrinos and estimating the sensitivity for their total mass in case of the Normal or Inverted Ordering. After that, it has been considered the hypothesis of a sterile neutrino with a mass of about 1 eV, in a model with three massless active neutrinos or three massive active neutrinos.

4.1 Methodology

To compute the sensitivity of the Euclid experiment, the CLASS and MontePython softwares presented in the previous chapter have been used. For the analysis developed in this thesis, the data samples are generated using fiducial parameter values of the ΛCDM model, taken from state-of-the-art reviews [9]. Starting from these values, given in the input file, MontePython automatically creates the fiducial files, that are the spectra that are expected to be seen by the experiments if the model described by the fiducial parameters is correct. These files are then stored and used as mock data in the analysis. For these fiducial parameters have been used values taken from Ref. [9] and shown in Tab. 4.1. They have been tightly constrained by observations and are characteristic of a standard ΛCDM model.

In the fiducial file are also contained data regarding the nuisance parameters of the Euclid matter power spectrum likelihood, described in Sec. 4.2.1: $\sigma_{NL} = 7$, $\beta_0^{Euclid} = 1$ and $\beta_1^{Euclid} = 1$. These values are treated in the analysis as fitting parameters to be determined along with the cosmological ones, in order to assess the effect of the redshift space distortions (RSDs). The shape and parameters of the likelihood are treated in

ω_b	ω_{cdm}	$100 \cdot \theta_s$	$\log[10^{10}A_s]$	n_s	τ_{reio}
0.02226	0.1186	1.0410	3.062	0.968	0.066

Table 4.1: Standard ΛCDM fiducial parameters values [9].

detail in the next section.

After the creation of fiducial files, it has been launched the first run creating four chains, in order to explore the parameter space and create an initial approximation of the target distribution, overdispersed but not too much inaccurate. In this way, it is possible to compute an initial covariance matrix, good enough to allow the convergence in the following run. This passage has been done using the eigenvectors of the proposal density to compute the jumps of the algorithm (with the `−j sequential` mode of MontePython), in order to accumulate points for the evaluation of the covariance matrix.

The second run has been launched using the same fiducial parameters and files of the first one and including the newly created covariance matrix to speed the convergence of the chains to the target distribution. In this case the chosen jumping method has been the default one, with a lower acceptance rate but a much lower correlation between the points. The four chains have been analysed with the MontePython `info` function during their creation, to check the value of the R-1 parameter for the Gelman Rubin criteria for convergence [53]. After reaching a satisfactory value for the R-1 value (less than 0.01), the run has been stopped and the plots have been created. The software, together with the plots, computes the convergence estimates, best-fit values, minimum credible intervals and the covariance matrix. 1-dimensional plots contain the posterior function (solid line) and the mean marginalised likelihood for each bin (dashed line), while the 2-d plots show the 2-dimensional posterior contours that emphasise the correlation between the parameters. During the runs have also been computed values of derived parameters such as the optical depth to reionisation τ_{reio}, the matter and dark energy densities Ω_m and Ω_Λ, H_0 and σ_8 (see Sec. 1.5.2, 1.4 and 1.6.2).

4.2 Likelihoods

The likelihoods for the Euclid cosmological probes described in Sec. 2.1.1, that have been used for this analyses, are already implemented in the MontePython code. From the cosmic shear survey it is possible to obtain informations about the weak gravitational lensing effect, that deviates at small angles the light from background galaxies due to the mass distributed between the source and the observer. The cosmic shear likelihood function is written in function of the three-dimensional matter power spectrum. The matter power spectrum is obtained from the galaxy clustering, i.e. from the correlation function quantifying the variations of clustering on a given scale, in relation to a uniform distribution. In this section the equations for the matter power spectrum likelihood and for the cosmic shear likelihood will be briefly described (see Ref. [54]).

4.2.1 Euclid matter power spectrum $P\left(k\right)$ likelihood

Given an observable $\mathbf{X_{obs}} = [X_1, \ldots, X_N]$ which is a function of the parameter set $\theta = [\theta_1, \ldots, \theta_n]$, it is possible to estimate the value of these parameters with a certain probability.
Given the likelihood function $\mathcal{L}\left(\mathbf{X_{obs}}/\theta\right)$, evaluated for the observed data and that depends on the parameter set, the minimum variance bound for the mean values of the observable is given by the Fisher information matrix, defined as

$$F_{ij} = \left\langle -\frac{\partial^2 \log \mathcal{L}\left(\mathbf{X_{obs}}/\theta\right)}{\partial\theta_i \partial\theta_j} \right\rangle . \tag{4.1}$$

If the parameters are gaussianly distributed, their likelihood can simply be written as

$$\mathcal{L}\left(\theta\right) \propto \exp -\frac{1}{2}\sum_{ij}\theta_i F_{ij}\theta_j . \tag{4.2}$$

In the case of the examined Euclid experiment, to compute the probability of the observed data E given the theory P, it is considered a single variable δ gaussianly distributed and centred on zero with a variance $\langle\delta^2\rangle = P$. Observing N independent realizations δ_n of δ, the estimator of the variance P is

$$E = \frac{1}{N}\sum_n \delta_n^2 . \tag{4.3}$$

The variance of E is $2P^2/N$ and, considering N large, the estimator E is nearly a Gaussian. The probability of the data E given the theory P can in this case be described by a Gaussian of mean P and variance $2P^2/N$, so that

$$-2\mathrm{ln}\mathcal{L}\left(E|P\right) = \frac{\left(E-P\right)^2}{2P^2/N} . \tag{4.4}$$

For a fixed theoretical model, the observed power spectrum P^{obs} in a bin b centred on the point (k_{ref}, μ, z) follows to a good approximation a Gaussian distribution. Here k_{ref} is the observed wavenumber (the subscript ref refers to the values assumed for the fiducial cosmological model), while $\mu = \hat{k}_{ref} \cdot \hat{r}$ is the cosine of the angle between the observed wavevector and the line of sight. If the spectrum that is expected to be seen given the theoretical model is P^{th}, the likelihood for each k_{ref} and μ bin is, using Eq. 4.4,

$$-2\ln\mathcal{L}_b = \sum_{i,j} \frac{\left(P^{obs}_{ij} - P^{th}_{ij}\right)^2}{2\left(P^{th}_{ij}\right)^2 / N_{ij}}, \tag{4.5}$$

where N_{ij} is the number of independent measurements in the bin. For a narrow redshift bin b, centred on $\bar{z}$, the likelihood becomes thus [54]

$$\mathcal{L}_b = \mathcal{N}_b \exp\left[-\frac{1}{2}\int_{-1}^{1} d\mu \int_{k_{min}}^{k_{max}} \frac{k^2_{ref} dk_{ref}}{(2\pi)^2} V_{eff} \frac{\left(P^{obs} - P^{th}\right)^2}{2\left(P^{th}\right)^2}\right], \tag{4.6}$$

where $P^{th/obs} = P^{th/obs}\left(k_{ref}, \mu, \bar{z}\right)$. $V_{eff} = V_{eff}\left(k_{ref}, \mu, \bar{z}\right)$ is the effective survey volume, that depends on the volume of the survey per bin $V_{survey}\left(\bar{z}\right)$ and from the galaxy number density per comoving volume $n_g\left(\bar{z}\right)$, while $\mathcal{N}_b$ is a normalisation factor. A shot noise $P_N\left(\bar{z}\right) = 1/n_g\left(\bar{z}\right)$, caused by the discreteness of the survey, is usually considered when computing the observed power spectrum for each bin, obtaining $P^{obs}\left(k, \mu, \bar{z}\right) = P_g\left(k, \mu, \bar{z}\right) + P_N\left(\bar{z}\right)$. The term $P_g\left(k, \mu, \bar{z}\right)$ is thus called the galaxy spectrum.

The error on the measurement of the redshift has been introduced in the code computing the likelihood with $\sigma_r = \sigma_z / H\left(z\right)$ representing the absolute error on the measurement of the distance r and $\sigma_z = 0.001\left(1+z\right)$ the absolute error on redshift. These value matches the one needed for the NISP instrument to measure the galaxy clustering and the BAO (see Ch. 2).

The matter power spectrum likelihood presents in addition three nuisance parameters:

- σ_{NL} represents the non-linear velocity dispersion and its squared value is added to σ_r^2. The effect of this velocity dispersion, measured from the neutral Hydrogen 21 cm line intensity, gives a sharp reduction of the power spectrum on small scales compared to the predictions of the linear model [55].
- β_0^{Euclid} and β_1^{Euclid} accounts instead for inaccuracies in the determination of the matter bias factor, that relates the distribution of mass to the distribution of galaxies and is assumed Gaussian and redshift dependent.

4.2.2 Euclid cosmic shear likelihood

Considering Eq. 2.13 and using $dz/dr = H$, the relation between the three-dimensional matter power spectrum and to the two-dimensional shear power spectrum [56, 57] can be written as

$$C_l^{ij} = \frac{9}{16}\Omega_m^2 H_0^4 \int_0^\infty \frac{dr}{r^2} g_i\left(r\right) g_j\left(r\right) P\left(k = \frac{l}{r}, z\left(r\right)\right), \tag{4.7}$$

with

$$g_i\left(r\right) = 2r\left(1 + z\left(r\right)\right) \int_0^\infty dr_s \frac{H\left(r_s\right) n_i\left(z\left(r_s\right)\right)\left(r_s - r\right)}{r_s}. \tag{4.8}$$

where $n_i\left(z\right)$ is the number of galaxies per steradian in the i-th bin, that depends on a Gaussian uncertainty on the photometric redshift with $\sigma_{ph} = 0.05\left(1+z\right)$, a precision required from the scientific requirements for the probes and seen in Chapter 2.

To obtain the cosmic shear likelihood the covariant matrices of observed/mock $\widetilde{\mathbf{C}}_l^{obs}$ and theoretical $\widetilde{\mathbf{C}}_l^{th}$ data are computed, where the elements $\widetilde{C}_l^{obs/th\,ij}$ comes respectively from the observed spectra $C_l^{obs/th\,ij}$. The elements can be calculated from the observed multipoles $a_{lm}^{obs\,i}$ as

$$\widetilde{C}_l^{obs\,ij} = \frac{1}{2l+1}\sum_{m=-l}^{l}\left[a_{lm}^{obs\,i*}a_{lm}^{obs\,j}\right], \tag{4.9}$$

where the multipoles are supposed Gaussian distributed and uncorrelated in (l,m) space for an ideal full-sky experiment. The likelihood of the observed spectra given the theoretical spectra becomes thus

$$\mathcal{L} = \mathcal{N}\prod_{lm}\left\{\frac{1}{\sqrt{\det \widetilde{C}_l^{th\,ij}}}\exp\left[-\frac{1}{2}\sum_{i,j}a_{lm}^{obs\,i*}\left(\widetilde{C}_l^{th\,-1}\right)^{ij}a_{lm}^{obs\,j}\right]\right\}, \tag{4.10}$$

with $\mathcal{N}$ a normalisation factor.

Defining the determinants of the $N\times N$ covariance matrices including the noise spectra $\widetilde{C}_l^{th/obs\ ij} = C_l^{th/fiducial\ ij} + N_l^{ij}$ as

$$d_l^{obs/th} = \det\left(\widetilde{C}_l^{obs/th\ ij}\right), \tag{4.11}$$

$$d_l^{mix} = \sum_k \det\left(N_l^{ij} + \left\{\begin{array}{ll} C_l^{th\,ij} & j\neq k \\ C_l^{fiducial\,ij} & j=k \end{array}\right.\right), \tag{4.12}$$

the likelihood in Eq. 4.10 can be written as [54]

$$\mathcal{L} = \mathcal{N}\prod_{l}\left\{\frac{1}{\left(d_l^{th}\right)^{1/2}}\exp\left[-\frac{(2l+1)}{2}\frac{d_l^{mix}}{d_l^{th}}\right]\right\}. \tag{4.13}$$

The value of the effective chi-square, defined as

$$\chi^2_{eff} \equiv -2\ln\mathcal{L} = -2\ln\mathcal{N} + \sum_l (2l+1)\left(\frac{d_l^{mix}}{d_l^{th}} + \ln d_l^{th}\right), \tag{4.14}$$

reaches a minimum value when the theoretical results are equal to the observed one. Due to this definition, it is possible to relate the value of the minimum χ^2 to the maximum likelihood as $\chi^{2\,min}_{eff} \equiv -2\ln\mathcal{L}_{max}$.

The χ^2 relative to the best fit model and implemented in the code is thus, introducing the sky coverage factor $f_{sky} = 0.3636$,

$$\Delta\chi^2_{eff} \equiv -2\ln\frac{\mathcal{L}}{\mathcal{L}_{max}} = \sum_l (2l+1)\, f_{sky} \left(\frac{d_l^{mix}}{d_l^{th}} + \ln\frac{d_l^{th}}{d_l^{obs}} - N \right). \tag{4.15}$$

4.3 Models

The ΛCDM model, as shown in Sec. 1.5.2, is based on the assumption of inflation, cold dark matter and of a cosmological constant and it is characterised by essentially six independent parameters $(\omega_b, \omega_{cdm}, \theta_s, A_s, n_s, \tau_{reio})$. The first value $\omega_b = \Omega_b h^2$ is the density of baryonic matter, while $\omega_{cmd} = \Omega_{cdm} h^2$ is the density of cold dark matter, A_s and n_s are the amplitude and tilt of the primordial power spectrum and τ_{reio} the reionisation optical depth. θ_s is the ratio between the sound horizon r_s and the angular diameter distance D_A at decoupling. From the values of ω_b and ω_{cdm} it is also possible to obtain the total matter density Ω_m and, assuming a flat Universe, the cosmological constant density parameter Ω_Λ.

4.3.1 Standard Cosmological Model ΛCDM

The first model tested is the ΛCDM Standard Model, with one massive neutrino ν and two massless (and consequently ultra-relativistic) neutrinos ν_0. Fiducial values of cosmological parameters are the ones from Tab. 4.1, while the ones regarding neutrinos have been chosen so that the number of effective neutrinos in the early universe is $N_{eff} = 3.046$, i.e., the standard one for three active neutrinos:

$$N_{\nu_0} = 2.0328, \quad N_\nu = 1,$$

while the total neutrino mass, i.e. the sum of the 3 neutrino masses, is fixed to the minimal value in case of Normal Ordering, $m_\nu = 0.06\,\mathrm{eV}$. Neutrinos are treated in CLASS as non cold dark matter, because their mass is low enough that, at sufficiently early times, they can be assumed massless. The default value for the non cold dark matter temperature $T_{ncdm} = 0.71611$ (where $T_{ncdm} \equiv T_\nu/T_\gamma$ is the ratio of neutrino to the photon temperature) is designed to give $M_\nu/\omega_\nu = 93.14\,\mathrm{eV}$ in the non-relativistic limit (see Sec. 1.5.3 and Ref. [48]) and has been used in all runs.

The mock data resulting from the run are compatible with the fiducial values and are shown in Tab. 4.2. Comparing the sensitivity that will be reached by the Euclid experiment to the Planck measurements, as shown in Tab. 4.3, a noticeable improvement is found for all the cosmological parameters. In this table the sensitivities have been compared defining the ratio r_x, with $x = P, E$ (where P stands for Planck and E stands for Euclid), as the percent ratio between the sigma and the mean value. The best

Param	best-fit	sigma	mean$\pm\sigma$	95% lower	95% upper
$100\ \omega_b$	2.226	0.011	$2.226^{+0.011}_{-0.011}$	2.203	2.248
ω_{cdm}	0.1187	0.00029	$0.1186^{+0.0003}_{-0.00028}$	0.118	0.1191
$ln10^{10}A_s$	3.061	0.0056	$3.063^{+0.0053}_{-0.006}$	3.052	3.073
n_s	0.9679	0.0022	$0.9681^{+0.0022}_{-0.0022}$	0.9638	0.9726
τ_{reio}	0.06558	0.0032	$0.0664^{+0.003}_{-0.0033}$	0.06034	0.07203
H_0 $[\mathrm{km\,s^{-1}Mpc^{-1}}]$	67.49	0.14	$67.48^{+0.14}_{-0.13}$	67.22	67.74
σ_8	0.8142	0.0020	$0.8145^{+0.0019}_{-0.0021}$	0.8107	0.8183

Table 4.2: Standard ΛCDM results.

improvements are obtained for the ω_{cdm} and H_0 values. The measurement of ω_{cdm} from Planck shows a sensitivity at 1.0%, while this forecast predicts a sensitivity for Euclid at 0.24%, for an improvement of 76%. Similarly, the sensitivity on H_0 will improve by 74%, while σ_8 and $ln\,[10^{10}A_s]$ will have an improvement of more than 60%. Even the ω_b parameter, that will experience the worst improvement, will increase its sensitivity by 26%.

Parameter	Planck			Euclid			Improvement
	mean	sigma	r_P	mean	sigma	r_E	$(r_P - r_e)/r_P$
$100\ \omega_b$	2.233	0.015	0.67%	2.226	0.011	0.49%	26%
ω_{cdm}	0.1198	0.0012	1.0%	0.1186	0.00029	0.24%	76%
$ln10^{10}A_s$	3.043	0.014	0.46%	3.063	0.0056	0.18%	61%
n_s	0.9652	0.0042	0.44%	0.9681	0.0022	0.23%	48%
τ_{reio}	0.0540	0.0074	14%	0.0664	0.0032	4.8%	65%
H_0 $[\mathrm{km\,s^{-1}Mpc^{-1}}]$	67.37	0.54	0.80%	67.48	0.14	0.21%	74%
σ_8	0.8101	0.0061	0.75%	0.8145	0.0020	0.25%	67%

Table 4.3: Comparison of Planck sensitivities for ΛCDM (combined results from Tab. 1 of Ref. [11]) and Euclid forecasts from this analysis. r_P and r_E are respectively the ratio between the sigma and the mean value for the Planck and for the Euclid experiments.

The triangular plot of Fig. 4.1 shows the marginalised likelihoods (dashed lines) and the 1-dimensional and 2-dimensional shape of the posterior functions (solid lines and shaded plots) obtained from this analysis and from which the sensitivities for each parameter have been calculated. The results brought by the Euclid experiment will thus help to strengthen the constraints on the values of the fundamental cosmological parameters.

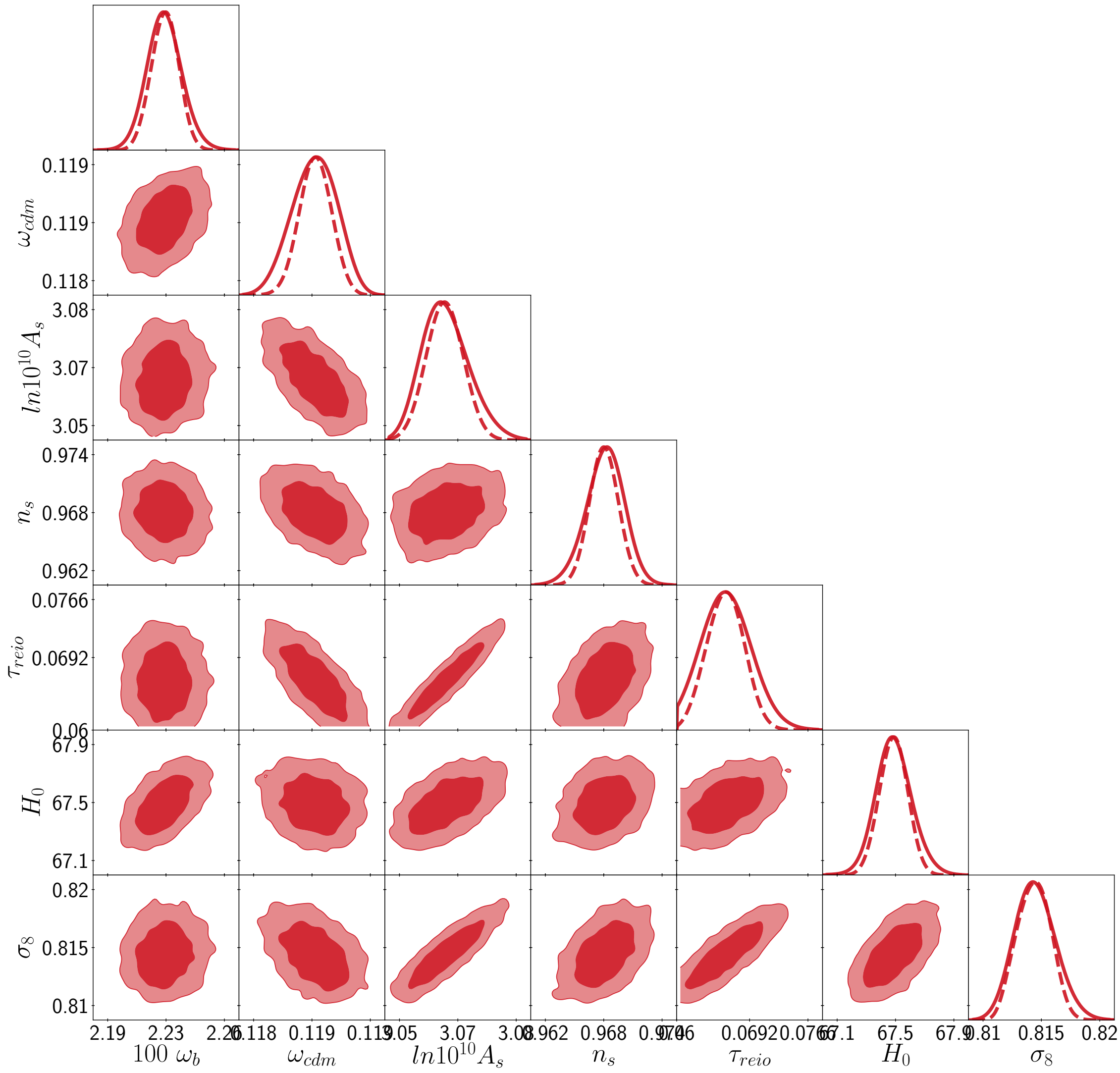

Figure 4.1: Standard ΛCDM model posterior distributions for the cosmological parameters 100 ω_b, ω_{cdm}, $ln10^{10}A_s$, n_s, τ_{reio}, H_0 and σ_8.

4.3.2 ΛCDM with three massive neutrinos

After the study of the standard ΛCDM model, it has been tested the sensitivity of the Euclid experiment assuming the ΛCDM and three massive neutrinos model. The total mass has been supposed equally divided into the three neutrino mass states, because previous studies have shown this choice reduces the computation time needed for the inference on cosmological parameters, but the differences with the results of an analysis with the correct mass splittings between neutrinos are negligible [56].

In this work both the case of Normal Ordering of the neutrino masses, with a total neutrino mass $M_{tot} = 0.06\,\mathrm{eV}$ corresponding to the minimal sum for NO assuming m_{ν_1} negligible, and the case of the Inverted Ordering, with a total mass $M_{tot} = 0.1\,\mathrm{eV}$ corresponding to the minimal sum assuming m_{ν_3} negligible, have been tested.
To evaluate the sensitivity on the total mass and on the number of effective neutrinos, two types of run have been executed. In the first type the number of effective neutrinos was fixed and the total neutrino mass was left free to vary, while vice versa in the second one the mass was considered fixed and it has been tested the sensitivity on the number of effective neutrinos.

Fixed neutrino number and varying total mass

For this type of analysis the parameters reported in Tab. 4.1 have been used, with in addition three effective neutrinos of equal mass:

$$N_{\nu_0} = 0.00641, \quad N_{ncdm} = 1 \text{ with } N_\nu = 3, \quad M_{tot} = 0.06\,\mathrm{eV}/0.1\,\mathrm{eV}.$$

The first term, accounting for relativistic neutrinos, has been added to maintain the value of $N_{eff} = 3.046$ in the early universe, while the second one, N_{ncdm}, describes the number of non-cold dark matter species such as massive neutrinos (active or sterile), warm dark matter or relics. In this case the only species considered is the massive active neutrino type, with a multiplicity of three ($N_\nu = 3$). This multiplicity stands for the number of families, i.e. of the couples of one particle and its antiparticle.

In order to test the sensitivity on the total neutrino mass in case of the Normal Ordering and the Inverted Ordering, the parameter N_ν (the number of neutrinos) was considered fixed, while two different runs have been done to account for the different total masses.

- In the first case studied, testing the Normal Ordering, the total neutrino mass M_{tot} has been set to $0.06\,\mathrm{eV}$. Results for the expected sensitivity are shown in Tab. 4.4.
- In the second case, testing the sensitivity for the Inverted Ordering, the total neutrino mass has been set to $M_{tot} = 0.1\,\mathrm{eV}$ and results are shown in Tab. 4.5.

The sensitivities for the cosmological parameters do not change significantly between the two runs despite the different masses. With respect to the Euclid standard ΛCDM prevision, however, the sensitivity slightly worsen for the parameters $ln10^{10}A_s$, τ_{reio} and σ_8. The obtained results show anyway a remarkable improvement with respect to the Planck measurements. The expected sensitivity on the measurement of the total neutrino mass M_{tot} is evaluated to be of the order of $0.02\,\mathrm{eV}$ not depending on the neutrino mass

Param	best-fit	sigma	mean$\pm\sigma$	95% lower	95% upper
$100\ \omega_b$	2.228	0.012	$2.227^{+0.012}_{-0.012}$	2.204	2.251
ω_{cdm}	0.1185	0.00031	$0.1186^{+0.00032}_{-0.00029}$	0.118	0.1192
$ln10^{10}A_s$	3.064	0.0077	$3.064^{+0.0054}_{-0.01}$	3.05	3.079
n_s	0.9681	0.0022	$0.9682^{+0.0022}_{-0.0023}$	0.9638	0.9727
τ_{reio}	0.06702	0.0042	$0.06688^{+0.0029}_{-0.0055}$	0.06001	0.07463
M_{tot} [eV]	0.071	0.023	$0.06166^{+0.024}_{-0.022}$	0.01614	0.106
H_0 [$\mathrm{km\,s^{-1}Mpc^{-1}}$]	67.48	0.19	$67.54^{+0.18}_{-0.19}$	67.19	67.93
σ_8	0.8142	0.0036	$0.816^{+0.0034}_{-0.0038}$	0.8093	0.8232

Table 4.4: Sensitivity for ΛCDM+M_{tot} (total neutrino mass) with three massive neutrinos (NO). The number of neutrinos $N_\nu = 3$ is fixed.

Param	best-fit	sigma	mean$\pm\sigma$	95% lower	95% upper
$100\ \omega_b$	2.227	0.011	$2.226^{+0.011}_{-0.012}$	2.204	2.249
ω_{cdm}	0.1186	0.0003	$0.1186^{+0.00032}_{-0.00028}$	0.1179	0.1192
$ln10^{10}A_s$	3.06	0.0077	$3.064^{+0.0059}_{-0.0094}$	3.05	3.079
n_s	0.9674	0.0022	$0.9683^{+0.0023}_{-0.0022}$	0.9638	0.9726
τ_{reio}	0.0648	0.0041	$0.06699^{+0.003}_{-0.0051}$	0.06	0.07453
M_{tot} [eV]	0.09936	0.021	$0.1032^{+0.02}_{-0.021}$	0.06317	0.1445
H_0 [$\mathrm{km\,s^{-1}Mpc^{-1}}$]	67.11	0.18	$67.17^{+0.19}_{-0.18}$	66.8	67.54
σ_8	0.8058	0.0034	$0.8067^{+0.0034}_{-0.0034}$	0.7999	0.8135

Table 4.5: Sensitivity for ΛCDM+M_{tot} (total neutrino mass) with three massive neutrinos (IO). The number of neutrinos $N_\nu = 3$ is fixed.

ordering, allowing to distinguish between the two mass orderings once the experimental data will be obtained.

In Fig. 4.2 and Fig. 4.3 are shown the most interesting and pronounced parameter degeneracies involving the total neutrino mass M_{tot}, that is strongly correlated with H_0 and σ_8. Considering the neutrino number fixed, if the total neutrino mass becomes greater both H_0 and σ_8 becomes smaller, due to the strong degeneracy between their values. This effect does not depend on the neutrino mass ordering and, for this reason, other data sets are required to be added in the global analysis to break the degeneracy. As an example, the direct measurements of the Hubble constant H_0 could make possible to put more stringent constraints on the value of the neutrino total mass M_{tot}.

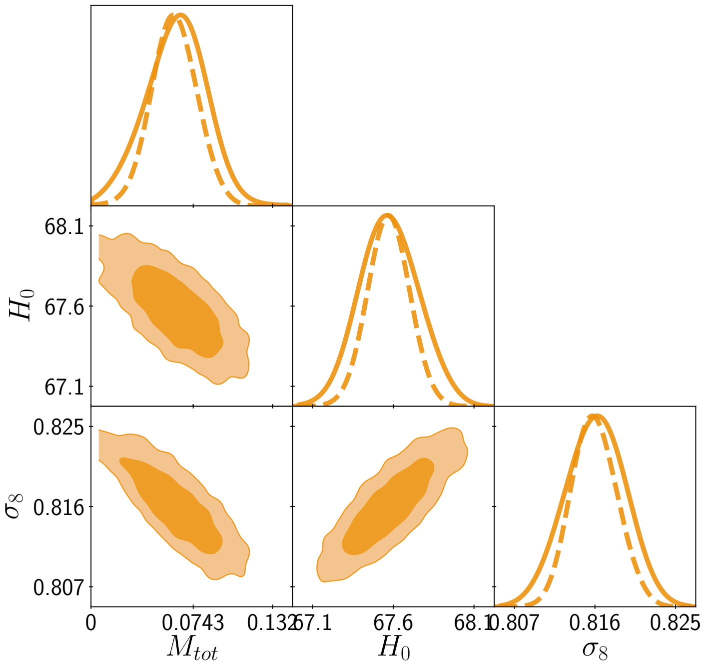

Figure 4.2: ΛCDM+M_{tot} model with three massive neutrinos posteriors for M_{tot} (total neutrino mass), H_0 and σ_8 (NO). The number of neutrinos $N_\nu = 3$ is fixed.

Fixed total neutrino mass and varying number of neutrinos

In the second type of analysis with three massive neutrinos, the total mass M_{tot} has been considered fixed and it has been evaluated the sensitivity on the number of active neutrinos. The fiducial parameters have been taken from Tab. 4.1 as in the first type of analysis, with

$$N_{\nu_0} = 0.00641, \quad N_{ncdm} = 1 \text{ with } N_\nu = 3, \quad M_{tot} = 0.06\,\text{eV}/0.1\,\text{eV},$$

and choosing a different value for the total neutrino mass in case of the tested ordering. Results for NO are shown in Tab. 4.6, while for IO they are shown in Tab. 4.7.

Also in this type of analysis the sensitivity does not depend on the chosen value for the total mass M_{tot}, i.e. it does not depend directly on the neutrino mass ordering, but there is a different effect with respect to the previous analysis on the results for previsions on cosmological parameter sensitivities. All the sensitivities slightly worsen with respect to the standard ΛCDM model forecasts for Euclid, but for H_0 and ω_{cdm} they worsen remarkably and the two sensitivities respectively triples and nearly quadruples. Their values show however a little improvement with respect to the Planck measurements, so the addition of other datasets constraining both the values of total neutrino mass and H_0 could bring to an improvement for the determination of the values of the cosmological

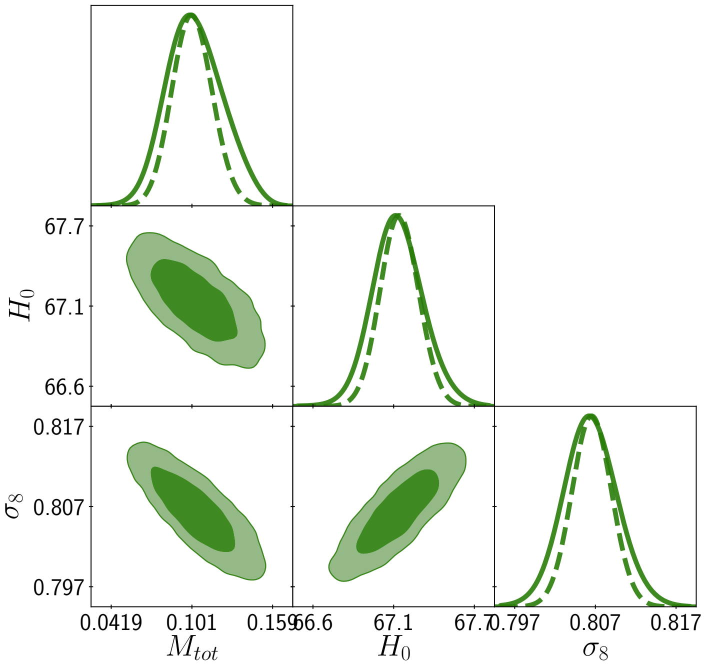

Figure 4.3: ΛCDM+M_{tot} model with three massive neutrinos posteriors for M_{tot} (total neutrino mass), H_0 and σ_8 (IO). The number of neutrinos $N_\nu = 3$ is fixed.

parameters as a whole. The sensitivity for the number of neutrinos is of the order of 0.066, a value precise enough to determine the exact number of neutrino species.

In Fig. 4.4 are shown the superimposed posterior functions (solid line) and the marginalised likelihoods (dashed lines) for both the analysis for NO and IO. The posterior functions for the number of neutrinos are as expected the same, while the differences for the mean values of σ_8 are compatible with the effect of a different total neutrino mass on clustering. In this case too it is possible to observe the strong degeneracy between the H_0 and σ_8 values and the neutrino-related parameter N_ν. Considering a fixed value of the total neutrino mass M_{tot}, if the neutrino number becomes higher also the values of H_0 and σ_8 increase, independently on the chosen value of M_{tot} for NO or IO. This degeneracy makes necessary the addition of an independent dataset, constraining one of the values in order to break the degeneracy.

4.3.3 Adding a sterile neutrino to the ΛCDM model

In this section a 1 eV sterile neutrino has been added to the ΛCDM model, testing the Euclid sensitivity to its mass. Introduced in Sec. 1.1.3, sterile neutrinos do not weakly interact, but only modify the Universe evolution and, as a consequence, the derived values for H_0 and σ_8.

Param	best-fit	sigma	mean$\pm\sigma$	95% lower	95% upper
$100~\omega_b$	2.23	0.013	$2.226^{+0.013}_{-0.014}$	2.199	2.253
ω_{cdm}	0.1191	0.0011	$0.1185^{+0.0011}_{-0.001}$	0.1164	0.1206
$ln10^{10}A_s$	3.061	0.0059	$3.063^{+0.0054}_{-0.0064}$	3.051	3.075
n_s	0.9681	0.0024	$0.968^{+0.0023}_{-0.0024}$	0.9632	0.9728
τ_{reio}	0.06497	0.0034	$0.0666^{+0.0029}_{-0.0039}$	0.06015	0.07273
N_ν	3.024	0.067	$2.997^{+0.065}_{-0.068}$	2.867	3.129
H_0 $[\mathrm{km\,s^{-1}Mpc^{-1}}]$	67.64	0.42	$67.53^{+0.43}_{-0.42}$	66.68	68.36
σ_8	0.816	0.0027	$0.8162^{+0.0027}_{-0.0027}$	0.8109	0.8217

Table 4.6: Sensitivity for ΛCDM+N_ν (number of effective neutrinos) with three massive neutrinos, with their total mass fixed to $M_{tot} = 0.06\,\mathrm{eV}$ (NO).

Param	best-fit	sigma	mean$\pm\sigma$	95% lower	95% upper
$100~\omega_b$	2.221	0.013	$2.226^{+0.013}_{-0.013}$	2.199	2.253
ω_{cdm}	0.1186	0.0011	$0.1186^{+0.001}_{-0.0011}$	0.1165	0.1208
$ln10^{10}A_s$	3.061	0.0056	$3.063^{+0.0052}_{-0.0059}$	3.052	3.074
n_s	0.9677	0.0024	$0.9682^{+0.0024}_{-0.0024}$	0.9635	0.973
τ_{reio}	0.06569	0.0033	$0.06646^{+0.0029}_{-0.0036}$	0.06006	0.07238
N_ν	3.002	0.066	$3.001^{+0.065}_{-0.067}$	2.872	3.135
H_0 $[\mathrm{km\,s^{-1}Mpc^{-1}}]$	67.17	0.43	$67.2^{+0.4}_{-0.45}$	66.37	68.07
σ_8	0.8067	0.0027	$0.8071^{+0.0025}_{-0.0029}$	0.8018	0.8123

Table 4.7: Sensitivity for ΛCDM+N_ν (number of effective neutrinos) with three massive neutrinos, with their total mass fixed to $M_{tot} = 0.1\,\mathrm{eV}$ (IO).

In this analysis two scenarios have been considered: in the first case it has been assumed that the three active neutrino were massless, while only the sterile one was massive, while in the second case also the three active neutrinos have been considered massive, each one with the same mass $m_\nu = 0.02$ eV.

One light sterile neutrino and three massless active neutrinos

For this analysis, as done for the previously presented ones, the cosmological parameters reported in Tab. 4.1 have been used. In addition, the three active neutrinos have been considered massless, while it has been added a sterile neutrino with a mass of 1 eV. The parameters used in the MontePython code to represent these four neutrinos were

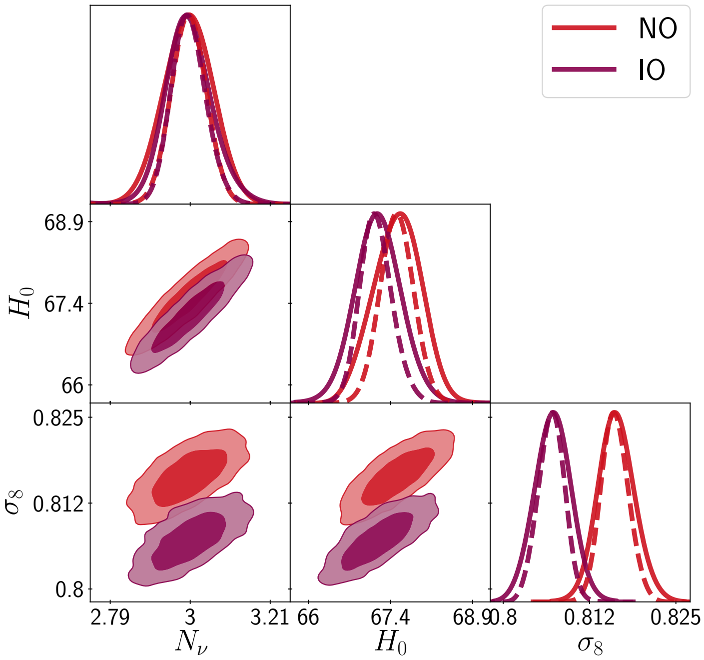

Figure 4.4: ΛCDM+N_ν model with three massive neutrinos posteriors for N_ν (number of effective neutrinos), H_0 and σ_8. The sensitivity for the number of neutrinos has been tested for a fixed value of $M_{tot} = 0.06\,\mathrm{eV}$ in case of Normal Ordering (red) and for a fixed value of $M_{tot} = 0.1\,\mathrm{eV}$ in case of Inverted Ordering (purple).

$$N_{\nu_0} = 3.046, \quad N_{ncdm} = 1 \text{ with } N_{\nu_s} = 1, \quad m_{\nu_s} = 1.0\,\mathrm{eV},$$

where the non-cold dark matter species $N_{ncdm} = 1$ refers to the extra sterile neutrino, with a multiplicity of 1 ($N_{\nu_s} = 1$) and a mass $m_{\nu_s} = 1.0\,\mathrm{eV}$. The three active neutrinos, being massless, are relativistic and are accounted for in the term $N_{\nu_0} = 3.046$.

The results are presented in Tab. 4.8 and the obtained sensitivities are similar to the ones for the ΛCDM+M_{tot} model with three massive neutrinos, considering the number of neutrinos fixed (see Tab. 4.4 and 4.5). The most relevant difference is the value of the sensitivity for ω_{cdm} that increases to 0.00098, at the order of 0.83% and similar to the sensitivity obtained from Planck measurements, at 1.0% (see Tab. 4.3). The expected Euclid sensitivity to the extra number of neutrinos N_{ν_s}, i.e. the number of sterile neutrinos, is found to be 0.066, while the sensitivity to the sterile neutrino mass is 0.035 eV.

In Figure 4.5 are shown the posterior functions (solid line) and the marginalised likelihoods (dashed lines) for the ΛCDM+ν_s model, considering three massless active neutrinos. The degeneracy observed between m_{ν_s} and H_0 and the one between N_{ν_s} and H_0 are of the same type of the ones seen for the active neutrino parameters M_{tot} and N_ν with the Hubble constant H_0 (see Figures 4.2, 4.3 and 4.4): when the mass becomes

Param	best-fit	sigma	mean$\pm\sigma$	95% lower	95% upper
$100~\omega_b$	2.232	0.013	$2.227^{+0.013}_{-0.013}$	2.201	2.253
ω_{cdm}	0.1185	0.00098	$0.1187^{+0.00094}_{-0.001}$	0.1169	0.1207
$ln10^{10}A_s$	3.062	0.0088	$3.064^{+0.0073}_{-0.01}$	3.048	3.082
n_s	0.967	0.0028	$0.9684^{+0.0027}_{-0.0028}$	0.9628	0.9741
τ_{reio}	0.06581	0.0039	$0.06694^{+0.0031}_{-0.0048}$	0.06	0.0741
m_{ν_s} [eV]	0.9989	0.035	$0.9955^{+0.033}_{-0.038}$	0.9282	1.066
N_{ν_s}	0.9925	0.066	$1.013^{+0.062}_{-0.07}$	0.8845	1.141
H_0 [$\mathrm{km\,s^{-1}Mpc^{-1}}$]	72.23	0.24	$72.25^{+0.23}_{-0.25}$	71.78	72.74
σ_8	0.634	0.0024	$0.6334^{+0.0023}_{-0.0025}$	0.6287	0.6383

Table 4.8: Sensitivities for ΛCDM+ν_s with one light sterile neutrino ($N_{\nu_s} = 1$ with mass $m_{\nu_s} = 1.0\,\mathrm{eV}$) and three massless active neutrinos.

bigger the value of H_0 lowers, while if the number of neutrino becomes higher also the value of H_0 increases. The mass of the sterile neutrino m_{ν_s} and the number of sterile neutrinos N_ν are tightly correlated one with the other: if the first becomes higher the second becomes lower.

One light sterile neutrino and three massive active neutrinos

In this second case the MontePython code has been modified to allow for two types of non-cold dark matter and, in this way, it has been possible to give mass to the three active neutrinos. It has been assumed that the sterile neutrinos would have the same temperature as the active neutrinos, so that the conversion from their effective mass to their physical mass is given for a Dodelson-Widrow sterile neutrino by $m_{\nu_s} = m^{eff}_{\nu_s}/N_{\nu_s}$ [58]. The fiducial parameters for this model have thus been setted as

$$N_{ncdm} = 2 \text{ with } N_\nu = 3 \text{ and } N_{\nu_s} = 1, \quad m_\nu = 0.02\,\mathrm{eV}, \quad m^{eff}_{\nu_s} = 1.0\,\mathrm{eV}.$$

They represent two species of non-cold dark matter $N_{ncdm} = 2$, where the first species has a multiplicity of three $N_\nu = 3$ and accounts for the active neutrinos with mass $m_\nu = 0.02\,\mathrm{eV}$, while the second species has a multiplicity of one $N_{\nu_s} = 1$ and accounts for a sterile neutrino with an effective mass $m^{eff}_{\nu_s} = 1.0\,\mathrm{eV}$. With the only exception of the mass of the sterile neutrino, all the described parameters have been considered fixed. The other parameters taken from Tab. 4.1 have been treated in the same way as in the other runs and left free to vary.

The results of the analysis are shown in Tab. 4.9 and the observed sensitivities are almost the same as the ones observed for the standard ΛCDM model (see Tab. 4.2). The sensitivity on the effective neutrino mass, in this case, is of $0.016\,\mathrm{eV}$, that is nearly the half

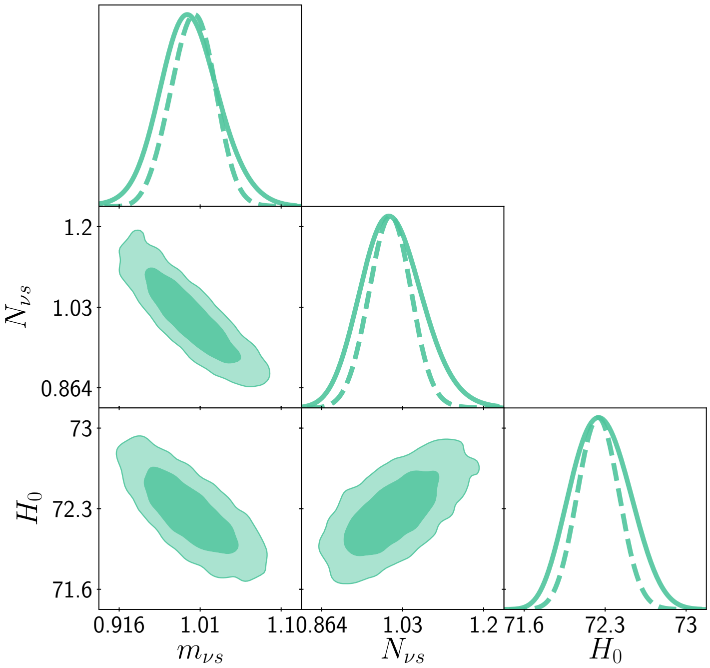

Figure 4.5: ΛCDM+ν_s model with three active massless neutrinos and one light sterile neutrino. Posterior distributions for m_{ν_s} (sterile neutrino mass), H_0 and σ_8, without fixing the number of extra sterile neutrinos.

with respect to the results obtained from a ΛCDM+ν_s model with three active massless neutrinos (see Tab. 4.8) without the constraint on the number of sterile neutrinos N_{ν_s}.

In Figure 4.6 are shown the degeneracies between the values of $m_{\nu_s}^{eff}$, H_0 and σ_8. Observing this plot and comparing it with the ones in Figures 4.2 and 4.3, the degeneracies results of the same type, confirming the result from the previous analysis.

Comparing both the models including light sterile neutrinos, the most evident effects are the ones on the H_0 and σ_8 values, that are respectively higher and lower with respect to the models without sterile neutrinos because of the effect of this additional mass on the Universe expansion. The sensitivity for the sterile neutrino mass is in the last, more parameter fixed case, of the order of 0.016 eV (four massive neutrinos, with active masses and neutrino numbers fixed), and in the first case is of 0.035 eV, where the neutrino number is not fixed. The degeneracies shown in Fig. 4.5 and 4.6 with the parameters H_0 and σ_8 are similar to the ones for active neutrinos. This is caused by the fact that, for cosmology, the value of the Hubble constant and the scale of clustering mostly depend on the particles densities and active and sterile neutrinos have the same effect on observables.

Current limits on the mass of a light sterile neutrino comes from Planck [11], adopting

Param	best-fit	sigma	mean$\pm\sigma$	95% lower	95% upper
$100~\omega_b$	2.218	0.012	$2.227^{+0.011}_{-0.013}$	2.202	2.25
ω_{cdm}	0.1184	0.00029	$0.1186^{+0.00031}_{-0.00027}$	0.118	0.1191
$ln10^{10}A_s$	3.062	0.0060	$3.063^{+0.0054}_{-0.0065}$	3.052	3.075
n_s	0.9693	0.0025	$0.9681^{+0.0024}_{-0.0026}$	0.9632	0.9731
τ_{reio}	0.06658	0.0033	$0.0664^{+0.003}_{-0.0035}$	0.06016	0.07249
$m_{\nu s}^{eff}$ [eV]	1.003	0.016	$1^{+0.016}_{-0.016}$	0.9693	1.032
H_0 [km s^{-1}Mpc^{-1}]	71.64	0.18	$71.7^{+0.17}_{-0.18}$	71.36	72.06
σ_8	0.6254	0.0019	$0.6259^{+0.0018}_{-0.002}$	0.6223	0.6294

Table 4.9: Sensitivities for ΛCDM+ν_s with one light sterile neutrino ($N_{\nu_s} = 1$ with mass $m_{\nu_s}^{eff} = 1.0\,$eV) and three massive active neutrinos ($N_\nu = 3$ with mass $m_\nu = 0.02\,$eV).

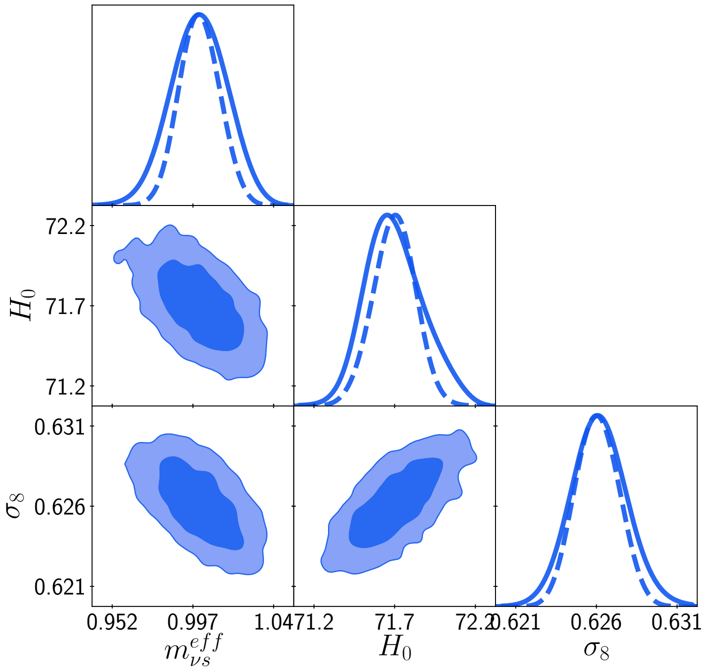

Figure 4.6: ΛCDM+ν_s model with three active massive neutrinos and one light sterile neutrino. Posterior distributions for $m_{\nu_s}^{eff}$ (sterile neutrino mass), H_0 and σ_8, having fixed the number of extra sterile neutrinos to 1.

a prior that $m_{\nu_s}^{thermal} < 10\,$eV, with $m_{\nu_s}^{thermal} = N_{\nu_s}^{-3/4} m_{\nu_s}^{eff}$, and defining $N_{eff} = N_\nu + N_{\nu_s}$. The upper limits become

$$N_{eff} < 3.29, \qquad m_{\nu_s}^{eff} < 0.65\,\text{eV} \qquad (95\%\,\text{CMB}) \tag{4.16}$$

for a model with minimal-mass active neutrinos and one additional sterile neutrino with mass $m_{\nu_s}^{eff}$. Adopting a stronger prior of $m_{\nu_s}^{thermal} < 2\,\mathrm{eV}$ it is obtained instead

$$N_{eff} < 3.34, \qquad m_{\nu_s}^{eff} < 0.23\,\mathrm{eV} \qquad (95\%\,\mathrm{CMB})\,. \tag{4.17}$$

Therefore, the expected Euclid sensitivities for sterile neutrinos represent again a significant improvement with respect to the current cosmological bounds.

Conclusions

The determination of neutrino properties is one of the most challenging problems of physics in the present day. Alongside ground-based experiments on neutrino oscillations and β-decays that aim to determine the neutrinos mass ordering and their absolute mass scale, also cosmology can provide robust constraints on the sum of neutrino masses. This is possible because of the strong impact that primordial neutrinos have during the evolution of the Universe, as during their free-streaming they smooth the density contrasts and slow down the galaxy clustering.

The ESA Euclid mission has been designed to observe a large fraction of the extragalactic sky in order to shed light on the "dark" Universe, allowing for stronger constraints on the dark energy equation of state, on dark matter properties and General Relativity on large scales. Euclid relays on two probes, the weak gravitational lensing and the galaxy clustering, that, together with the CMB surveys from Planck and other future CMB experiments, will allow to measure the total neutrino mass and the neutrino effective number with high sensitivity.

In this thesis, the future sensitivity of the Euclid mission on neutrino properties together with ΛCDM cosmological parameters is evaluated, using Bayesian inference. The results are obtained using the MontePython and CLASS codes, standard tools for cosmological statistical analysis. A fiducial cosmological parameter set, typical for a model, is given to MontePython which, using the implemented likelihoods, computes the posterior functions for all the initial parameters and for the derived ones. The sensitivity of the experiment for a parameter is then obtained from the marginalised posterior function.

The first analysis has evaluated the sensitivity for a standard ΛCDM cosmological model, then the results are compared with the ones from the Planck experiment. The obtained values show a noticeable improvement on the sensitivity with respect to Planck measurements.

The analysis has then considered the ΛCDM model plus active neutrinos, obtaining the constraints on the total neutrino mass M_{tot} and on the number of neutrinos N_ν in four cases:

- for a ΛCDM+M_{tot} model in case of a Normal Ordering of the neutrino masses, with a fiducial value $M_{tot} = 0.06\,\mathrm{eV}$ and a fixed number of effective neutrinos $N_\nu = 3$;

- for a ΛCDM+M_{tot} model in case of a Inverted Ordering of the neutrino masses, with a fiducial value $M_{tot} = 0.1\,\mathrm{eV}$ and a fixed number of effective neutrinos $N_\nu = 3$;
- for a ΛCDM+N_ν model in case of a Normal Ordering of the neutrino masses, with a fixed total neutrino mass $M_{tot} = 0.06\,\mathrm{eV}$ and a fiducial value for the number of effective neutrinos $N_\nu = 3$;
- for a ΛCDM+N_ν model in case of a Inverted Ordering of the neutrino masses, with a fixed total neutrino mass $M_{tot} = 0.1\,\mathrm{eV}$ and a fiducial value for the number of effective neutrinos $N_\nu = 3$.

The obtained sensitivities do not depend on the chosen value for the total mass M_{tot}, i.e. they do not depend directly on the neutrino mass ordering. In the first type of analyses, fixing N_ν, the obtained sensitivity for Euclid on the total neutrino mass is of the order of $0.02\,\mathrm{eV}$ and, not depending on the neutrino mass ordering, it will allow to distinguish between them once the experimental data will be obtained. In the second type of analyses, fixing the total neutrino mass M_{tot}, the sensitivity on the number of neutrinos N_ν is of the order of 0.066, a value precise enough to determine the exact number of neutrino species independently on the neutrino mass ordering.

The ΛCDM model has then been extended adding a light sterile neutrino, with an effective mass $m_{\nu_s}^{eff} = 1\,\mathrm{eV}$. The model has been tested for the sensitivity on the effective mass $m_{\nu_s}^{eff}$ in two cases:

- considering a ΛCDM+ν_s model with three active massless neutrinos and computing also the sensitivity on the number of sterile neutrinos N_{ν_s};
- considering a ΛCDM+ν_s model with three active massive neutrinos of fixed total mass $M_{tot} = 0.06\,\mathrm{eV}$.

The sensitivity on N_{ν_s} in the first case is of 0.066, the same value obtained for the ΛCDM+N_ν model. The best value obtained for the sensitivity on the effective mass $m_{\nu_s}^{eff}$ is of $0.016\,\mathrm{eV}$ for the second and more parameter fixed case.

The cosmological constraints from the Euclid experiment using BAO and weak lensing will be able to considerably improve the knowledge on neutrino properties. In particular, Euclid will have a high sensitivity on the neutrino mass, eventually allowing to determine the mass ordering, and will be able to determine the number of effective neutrinos with a sensitivity of 2.2% in the context of an extended ΛCDM model with three massive neutrinos.

The bounds obtained for an eventual extra neutrino of mass $1\,\mathrm{eV}$ do not instead set independent constraints on its mass. Sterile neutrinos are in fact seen from cosmology in the same way as active neutrinos, with the same dependencies on cosmological parameters and the same degeneracies, as seen in the plots with H_0 and σ_8. Strong bounds can be obtained through the effective neutrino number N_ν, but ground-based experiments, like the Short Baseline Neutrino program at Fermilab, will be essential to definitely confirm or rule out the light sterile neutrino hypothesis.

Bibliography

[1] L. D. Landau, *On the conservation laws for weak interactions*, *Nucl. Phys.* **3** (1957) 127.

[2] T. D. Lee and C.-N. Yang, *Parity Nonconservation and a Two Component Theory of the Neutrino*, *Phys. Rev.* **105** (1957) 1671.

[3] A. Salam, *On parity conservation and neutrino mass*, *Il Nuovo Cimento (1955-1965)* **5** (1957) 299.

[4] Particle Data Group collaboration, *Review of particle physics. Particle Data Group*, *Eur. Phys. J.* **C15** (2000) 1.

[5] B. Pontecorvo, *Mesonium and anti-mesonium*, *Sov. Phys. JETP* **6** (1957) 429.

[6] Z. Maki, M. Nakagawa and S. Sakata, *Remarks on the unified model of elementary particles*, *Prog. Theor. Phys.* **28** (1962) 870.

[7] I. Esteban, M. C. Gonzalez-Garcia, A. Hernandez-Cabezudo, M. Maltoni and T. Schwetz, *Global analysis of three-flavour neutrino oscillations: synergies and tensions in the determination of θ_{23}, δ_{CP}, and the mass ordering*, *JHEP* **01** (2019) 106 [`1811.05487`].

[8] C. Giganti, S. Lavignac and M. Zito, *Neutrino oscillations: the rise of the PMNS paradigm*, *Prog. Part. Nucl. Phys.* **98** (2018) 1 [`1710.00715`].

[9] Particle Data Group collaboration, *Review of Particle Physics*, *Phys. Rev.* **D98** (2018) 030001.

[10] KATRIN collaboration, *Improved upper limit on the neutrino mass from a direct kinematic method by katrin*, *Phys.Rev.Lett.* **123** (2019) 221802 [`1909.06048`].

[11] Planck collaboration, *Planck 2018 results. VI. Cosmological parameters*, `1807.06209`.

[12] LSND collaboration, *Evidence for neutrino oscillations from the observation of $\bar{\nu}_e$ appearance in a $\bar{\nu}_\mu$ beam*, *Phys. Rev.* **D64** (2001) 112007 [`hep-ex/0104049`].

[13] MiniBooNE collaboration, *A Search for Electron Neutrino Appearance at the $\Delta m^2 \sim 1eV^2$ Scale*, *Phys. Rev. Lett.* **98** (2007) 231801 [`0704.1500`].

[14] MiniBooNE collaboration, *Unexplained Excess of Electron-Like Events From a 1-GeV Neutrino Beam*, *Phys. Rev. Lett.* **102** (2009) 101802 [`0812.2243`].

[15] MiniBooNE collaboration, *Event Excess in the MiniBooNE Search for $\bar{\nu}_\mu \to \bar{\nu}_e$ Oscillations*, *Phys. Rev. Lett.* **105** (2010) 181801 [`1007.1150`].

[16] E. Akhmedov and T. Schwetz, *MiniBooNE and LSND data: Non-standard neutrino interactions in a (3+1) scheme versus (3+2) oscillations*, *JHEP* **10** (2010) 115 [`1007.4171`].

[17] J. Kopp, M. Maltoni and T. Schwetz, *Are There Sterile Neutrinos at the eV Scale?*, *Phys. Rev. Lett.* **107** (2011) 091801 [`1103.4570`].

[18] T. A. Mueller et al., *Improved Predictions of Reactor Antineutrino Spectra*, *Phys. Rev.* **C83** (2011) 054615 [`1101.2663`].

[19] K. Abazajian et al., *Light sterile neutrinos: A white paper*, `1204.5379`.

[20] SAGE collaboration, *Measurement of the solar neutrino capture rate with gallium metal. III: Results for the 2002–2007 data-taking period*, *Phys. Rev.* **C80** (2009) 015807 [`0901.2200`].

[21] SAGE collaboration, *Measurement of the response of the Russian-American gallium experiment to neutrinos from a Cr-51 source*, *Phys. Rev.* **C59** (1999) 2246 [`hep-ph/9803418`].

[22] D. V. Naumov, *The Sterile Neutrino: A short introduction*, *EPJ Web Conf.* **207** (2019) 04004 [`1901.00151`].

[23] Planck collaboration, *Planck 2018 results. I. Overview and the cosmological legacy of Planck*, `1807.06205`.

[24] A. Einstein, *On the General Theory of Relativity*, *Sitzungsber. Preuss. Akad. Wiss. Berlin (Math. Phys.)* **1915** (1915) 778.

[25] W. Hu and M. J. White, *A CMB polarization primer*, *New Astron.* **2** (1997) 323 [`astro-ph/9706147`].

[26] S. Galli, K. Benabed, F. Bouchet, J.-F. Cardoso, F. Elsner, E. Hivon et al., *CMB Polarization can constrain cosmology better than CMB temperature*, *Phys. Rev.* **D90** (2014) 063504 [`1403.5271`].

[27] R. Durrer, *The Cosmic Microwave Background*. Cambridge University Press, Cambridge, 2008, 10.1017/CBO9780511817205.

[28] ESA and the Planck Collaboration, "Planck's new cosmic recipe." `https://sci.esa.int/s/8o9qJ0w`.

[29] J. Lesgourgues and S. Pastor, *Massive neutrinos and cosmology*, *Phys. Rept.* **429** (2006) 307 [`astro-ph/0603494`].

[30] L. Verde, T. Treu and A. G. Riess, *Tensions between the Early and the Late Universe*, in *Nature Astronomy 2019*, 2019, `1907.10625`, DOI.

[31] A. G. Riess, *The Expansion of the Universe is Faster than Expected*, *Nature Rev. Phys.* **2** (2019) 10 [`2001.03624`].

[32] P. Coles and F. Lucchin, *Cosmology: The Origin and evolution of cosmic structure*. 1995.

[33] D. Rapetti, S. W. Allen, A. Mantz and H. Ebeling, *Constraints on modified gravity from the observed X-ray luminosity function of galaxy clusters*, *Mon. Not. Roy. Astron. Soc.* **400** (2009) 699 [`0812.2259`].

[34] EUCLID collaboration, *Euclid Definition Study Report*, `1110.3193`.

[35] E. Komatsu and D. N. Spergel, *Acoustic signatures in the primary microwave background bispectrum*, *Phys. Rev.* **D63** (2001) 063002 [`astro-ph/0005036`].

[36] L. Fu et al., *Very weak lensing in the CFHTLS Wide: Cosmology from cosmic shear in the linear regime*, *Astron. Astrophys.* **479** (2008) 9 [`0712.0884`].

[37] EUCLID collaboration, *Euclid: Reconstruction of Weak Lensing mass maps for non-Gaussianity studies*, `1910.03106`.

[38] P. Lemos, A. Challinor and G. Efstathiou, *The effect of Limber and flat-sky approximations on galaxy weak lensing*, *JCAP* **1705** (2017) 014 [`1704.01054`].

[39] SDSS collaboration, *Detection of the Baryon Acoustic Peak in the Large-Scale Correlation Function of SDSS Luminous Red Galaxies*, *Astrophys. J.* **633** (2005) 560 [`astro-ph/0501171`].

[40] W. J. Percival, S. Cole, D. J. Eisenstein, R. C. Nichol, J. A. Peacock, A. C. Pope et al., *Measuring the Baryon Acoustic Oscillation scale using the SDSS and 2dFGRS*, *Mon. Not. Roy. Astron. Soc.* **381** (2007) 1053 [`0705.3323`].

[41] H. Lin, R. P. Kirshner, S. A. Shectman, S. D. Landy, A. Oemler, D. L. Tucker et al., *The power spectrum of galaxy clustering in the las campanas redshift survey*, *Astrophys. J.* **471** (1996) 617 [`astro-ph/9606055`].

[42] L. M. Voigt, S. L. Bridle, A. Amara, M. Cropper, T. D. Kitching, R. Massey et al., *The impact of galaxy colour gradients on cosmic shear measurement*, *Mon. Not. Roy. Astron. Soc.* **421** (2012) 1385 [`1105.5595`].

[43] E. Semboloni et al., *On the shear estimation bias induced by the spatial variation of colour across galaxy profiles*, *Mon. Not. Roy. Astron. Soc.* **432** (2013) 2385 [`1211.5025`].

[44] EUCLID collaboration, *VIS: the visible imager for Euclid*, *Proc. SPIE Int. Soc. Opt. Eng.* **8442** (2012) 84420V [`1208.3369`].

[45] A. Secroun, B. Serra, J. Clemens, P. Lagier, M. Niclas, A. Ealet et al., *Characterization of infrared detectors for the euclid nisp instrument: Facilities design and validation introduction*, 06, 2014, DOI.

[46] R. Trotta, *Bayes in the sky: Bayesian inference and model selection in cosmology*, *Contemp. Phys.* **49** (2008) 71 [`0803.4089`].

[47] J. Lesgourgues, *The Cosmic Linear Anisotropy Solving System (CLASS) I: Overview*, `1104.2932`.

[48] J. Lesgourgues and T. Tram, *The Cosmic Linear Anisotropy Solving System (CLASS) IV: efficient implementation of non-cold relics*, *JCAP* **1109** (2011) 032 [`1104.2935`].

[49] C.-P. Ma and E. Bertschinger, *Cosmological perturbation theory in the synchronous and conformal Newtonian gauges*, *Astrophys. J.* **455** (1995) 7 [`astro-ph/9506072`].

[50] T. Tram and J. Lesgourgues, *Optimal polarisation equations in FLRW universes*, *JCAP* **1310** (2013) 002 [`1305.3261`].

[51] B. Audren, J. Lesgourgues, K. Benabed and S. Prunet, *Conservative Constraints on Early Cosmology: an illustration of the Monte Python cosmological parameter inference code*, *JCAP* **1302** (2013) 001 [`1210.7183`].

[52] T. Brinckmann and J. Lesgourgues, *MontePython 3: boosted MCMC sampler and other features*, `1804.07261`.

[53] A. Gelman and D. B. Rubin, *Inference from Iterative Simulation Using Multiple Sequences*, *Statist. Sci.* **7** (1992) 457.

[54] B. Audren, J. Lesgourgues, S. Bird, M. G. Haehnelt and M. Viel, *Neutrino masses and cosmological parameters from a Euclid-like survey: Markov Chain Monte Carlo forecasts including theoretical errors*, *JCAP* **1301** (2013) 026 [`1210.2194`].

[55] P. Bull, P. G. Ferreira, P. Patel and M. G. Santos, *Late-time cosmology with 21cm intensity mapping experiments*, *Astrophys. J.* **803** (2015) 21 [`1405.1452`].

[56] T. Sprenger, M. Archidiacono, T. Brinckmann, S. Clesse and J. Lesgourgues, *Cosmology in the era of Euclid and the Square Kilometre Array*, *JCAP* **1902** (2019) 047 [`1801.08331`].

[57] W. Hu and B. Jain, *Joint galaxy - lensing observables and the dark energy*, *Phys. Rev.* **D70** (2004) 043009 [`astro-ph/0312395`].

[58] S. Gariazzo, C. Giunti and M. Laveder, *Light Sterile Neutrinos in Cosmology and Short-Baseline Oscillation Experiments*, *JHEP* **11** (2013) 211 [`1309.3192`].

[59] B. Ryden, *Introduction to Cosmology.* Addison-Wesley, 2003.

[60] H. Hoekstra and B. Jain, *Weak Gravitational Lensing and its Cosmological Applications*, *Ann. Rev. Nucl. Part. Sci.* **58** (2008) 99 [`0805.0139`].

[61] W. Hu, *Power spectrum tomography with weak lensing*, *Astrophys. J.* **522** (1999) L21 [`astro-ph/9904153`].

[62] B. A. Bassett and R. Hlozek, *Baryon Acoustic Oscillations*, `0910.5224`.

[63] S. T. Petcov, *The Nature of Massive Neutrinos*, *Adv. High Energy Phys.* **2013** (2013) 852987 [`1303.5819`].

[64] L. Verde, *A practical guide to Basic Statistical Techniques for Data Analysis in Cosmology*, `0712.3028`.